Die Masernvirusinfektion verstärkt die Migration dendritischer Zellen in einer 3D-Umgebung

Measles virus infection enhances dendritic cell migration in a 3D environment

Doctoral thesis for a doctoral degree

at the Graduate School of Life Sciences

Julius-Maximilians-Universität Würzburg

Section: Infection and Immunity

submitted by

Shaghayegh Derakhshani

from Tehran, Iran

Würzburg 2019

Submitted on:

……..……..

Office stamp

Members of the *Promotionskomitee*:

Chairperson: Prof. Dr. Christian Janzen

Primary Supervisor: Prof. Dr. Sibylle Schneider-Schaulies

Supervisor (Second): Dr. Maria Steinke

Supervisor (Third): Prof. Dr. Manfred Lutz

Date of Public Defence: ……..……

Date of Receipt of Certificates: ……

Affidavit

I hereby declare that my thesis entitled "**Measles virus infection enhances dendritic cell migration in a 3D environment**" is the result of my own work. I did not receive any help or support from commercial consultants. All sources and/or materials applied are listed and specified in the thesis.

Furthermore, I verify that this thesis has not yet been submitted as part of another examination process neither in identical or similar form.

Würzburg, 2019

Shaghayegh Derakhshani

Eidesstattliche Erklärung

Hiermit erkläre ich an Eides statt, die Dissertation „ Die Masernvirusinfektion verstärkt die Migration dendritischer Zellen in einer 3D-Umgebung" eigenständig, d.h. insbesondere selbständig und ohne Hilfe eines kommerziellen Promotionsberaters, angefertigt und keine anderen als die von mir angegebenen Quellen und Hilfsmittel verwendet zu haben.

Ich erkläre außerdem, dass die Dissertation weder in gleicher noch in ähnlicher Form bereits in einem anderen Prüfungsverfahren vorgelegen hat.

Würzburg, 2019

Shaghayegh Derakhshani

Acknowledgments

First and foremost, I would like to express my sincere gratitude to my advisor, Prof. Dr. Sibylle Schneider-Schaulies, who has always been supportive in this challenging way and helped me in all ways she could. Her immense knowledge and guidance have always helped me in research and also to write this thesis. I deeply thank you for everything that I achieved in these years.

I would like to thank my other thesis committee members Dr. Maria Steinke for her continuous support, encouragement, and motivation, and Prof. Dr. Manfred Lutz for his insightful comments, constructive suggestions, and positive attitude.

My sincere thank goes to Prof. Dr. Jürgen Schneider-Schaulies for his positive energy and heartwarming smiles, fruitful discussions, and for kindly dedicating the cells that I needed in this work.

I would like to thank all my labmates, especially Dr. Elita Avota, for helping me to solve my problems and encouraging me. Charlene, Lena, Phillip, Anna, and Claudia for helping me with the Lab work and more importantly for making a friendly and fun atmosphere in the lab. Maria who I had such a memorable time with and experienced all moments full of joy, laughter, sadness, and a lot more during this PhD life. I thank you for being such a supportive friend for me. I would like to thank Lisa Pilgram for preparing the samples for lipidomics and analyzing the data.

I would like to thank all members of our 3D infect GRK2157 group especially Prof. Dr. Thomas Rudel and Prof. Dr. Heike Walles for their constant and great support and Dr. Matthias Schweinlin for his kind help and patience in teaching me to work with the 3D models.

I would like to appreciate the help and contributions in the published paper from this work.

My deepest thank goes to Andreas, who has always been there for me to help me with the scientific work in every part he could and on the top emotionally support me to be able to complete this journey. This time would be definitely not easy without you and your backup. Your trust, support, and love have always given me energy and enthusiasm to live happier and to see the world with a different look. Thank you so much for always being there for me.

Finally, I would like to thank my parents and my brother, who mean the whole world to me. It is because of their sacrifices, support, patience, and endless love that I am here right now, not just with a degree but with an enormous pack of experience from this new life in Germany. I am so blessed for having such a caring and loving family.

Table of contents

Abbreviations

Abbreviation	Long term/definition
%	percent
×g	gravitational constant
®	registered
°C	centigrade
2D	Two-dimensional
3D	Three-dimensional
APC	antigen-presenting cells
APS	ammonium persulfate
ARP2/3	actin-related proteins 2 and 3
ASM	acid sphingomyelinase
ATP	adenosine triphosphate
ATV	antibiotic-Trypsin-Versene
BSA	bovine serum albumin
$CaCl_2$	calcium chloride
Cas-9	CRISPR associated protein 9
CD	cluster of differentiation
Cdc42	cell division control protein 42 homolog
cDNA	complementary DNA
CERT	ceramide transfer protein
cm	centimeter
CNS	central nervous system
CO2	carbon dioxide

CRISPR	clustered regularly interspaced short palindromic repeats
crRNA	CRISPR RNA
CuSO4	Copper Sulphate
DAPI	4',6-Diamidin-2-phenylindol
DC	Dendritic cell
dH2O	Distilled water
DMEM	Dulbecco's modified Eagle's medium
DMSO	Dimethyl sulfoxide
DNA	Deoxyribonucleic acid
dNTP	2'-Deoxyribonucleoside-5'-triphosphate
Dr.	doctor
ECM	extracellular matrix
EDTA	ethylenediaminetetraacetic acid
ER	endoplasmatic reticulum
ERM	ezrin/radixin/moesin
F	measles virus fusion protein
FA	Formaldehyde
FACS	fluorescence-activated cell sorting
F-actin	filamentous actin
FCS	fetal calf serum
FIP	fusion inhibitory peptide
FITC	fluorescein isothiocyanate
FN	fibronectin
FSC	forward scatter
g	gram

GM-CSF	granulocyte-macrophage colony stimulating factor
GPCR	granulocyte-macrophage colony stimulating factor
GTP	guanosine triphosphate
h	hour/hours
H	measles virus hemagglutinin protein
HEK	human embryonic kidney cell
HEPES	4-(2-hydroxyethyl)-1-piperazineethanesulfonic acid
HIV	human immunodeficiency virus
HUVEC	human umbilical vein endothelial cell
IF	immunofluorescence
IFN I	interferon type I
Ig	immunoglobulin
IL	interlukin
kb	kilobase pair
KCl	potassium chloride
KD	knock down
kDa	kilo Dalton
L	measles virus large protein
LB	Luria-Bertani
LN	Lymph node
LPS	lipopolysaccharide
M	molar
mA	milliampere
MEM	minimal essential media

MFI	mean fluorescence intensity
MHC	major histocompatibility complex
MIBE	measles inclusion body encephalitis
min	minute
MLC	myosin light chain
MMP	metalloproteinase
MOI	multiplicity of infection
mRNA	Messenger ribonucleic acid
MV	measles virus
MxB	myxovirus resistance gene B
N	nucleoprotein
NaCl	sodium chloride
NaOH	sodium hydroxide
ng	nanogram
NSM	neutral sphingomyelinase
OD	optical density
P	measles virus phosphoprotein
PAGE	polyacrylamide gel electrophoresis
PBMC	peripheral blood mononuclear cell
PBS	phosphate-buffered saline
PCR	polymerase chain reaction
PEG	polyethylene glycol
PEI	polyethyleneimine
PFA	paraformaldehyde
pfu	plaque-forming unit
PH	pleckstrin homology domain
PI	propidium iodide
PI3	phosphoinositide-3

PLL	poly-L-lysin
pmol	picomole
Prof.	professor
PVRL-4	polio virus receptor-like protein-4
Rac	ras-related C3 botulinum toxin substrate
rMV	recombinant measles virus
RNA	ribonucleic acid
RNP	ribonucleoprotein
ROCK	Rho-associated protein kinase
rpm	revolutions per minute
RPMI	Roswell Park Memorial Institute
RT	room temperature
RT-PCR	reverse transcriptase polymerase chain reaction
S1P	sphingosine-1-phosphate
SDS	sodium-dodecylsulfat
sec	second/seconds
sgRNA	single guide RNA
siRNA	small interfering RNA
SIS^-	intestine submucosa without mucosa
SL	sphingolipid
SLAM	signaling lymphocytic activation molecule
SM	sphingomyelin
SMase	sphingomyelinase
SphK	sphingosine kinase
SSC	side scatter

SSPE	Subacute Sclerosing Pan Encephalitis
TAE	Tris-Acetate-EDTA
TE	Tris-EDTA
TEER	transepithelial electrical resistance
TEM	transendothelial migration
TEMED	tetramethylethylenediamine
Th	T-helper
TLR	toll-like receptor
TNFα	tumor necrosis factor α
tracrRNA	trans-activating CRISPR RNA
U	unit
UV	ultraviolet
VSV	Vesicular Stomatitis Virus
WASP	Wiskott-Aldrich-Syndrom-Protein
WT	wild type
µg	microgram
µL	microliter
µm	micrometer

Summary

The respiratory system is amongst the most important compartments in the human body. Due to its connection to the external environment, it is one of the most common portals of pathogen entry. Airborne pathogens like measles virus (MV) carried in liquid droplets exhaled from the infected individuals via a cough or sneeze enter the body from the upper respiratory tract and travel down to the lower respiratory tract and reach the alveoli. There, pathogens are captured by the resident dendritic cells (DCs) or macrophages and brought to the lymph node where immune responses or, as in case of MV, dissemination via the hematopoietic cell compartment are initiated. Basic mechanisms governing MV exit from the respiratory tract, especially virus transmission from infected immune cells to the epithelial cells have not been fully addressed before. Considering the importance of these factors in the viral spread, a complex close-to-*in-vivo* 3D human respiratory tract model was generated. This model was established using de-cellularized porcine intestine tissue as a biological scaffold and H358 cells as targets for infection. The scaffold was embedded with fibroblast cells, and later on, an endothelial cell layer seeded at the basolateral side. This provided an environment resembling the respiratory tract where MV infected DCs had to transmigrate through the collagen scaffold and transmit the virus to epithelial cells in a Nectin-4 dependent manner. For viral transmission, the access of infected DCs to the recipient epithelial cells is an essential prerequisite and therefore, this important factor which is reflected by cell migration was analyzed in this 3D system.

The enhanced motility of specifically MV-infected DCs in the 3D models was observed, which occurred independently of factors released from the other cell types in the models. Enhanced motility of infected DCs in 3D collagen matrices suggested infection-induced cytoskeletal remodeling, as also verified by detection of cytoskeletal polarization, uropod formation. This enforced migration was sensitive to ROCK inhibition revealing that MV infection induces an amoeboid migration mode in DCs. In support of this, the formation of podosome structures and filopodia, as well as their activity, were reduced in infected DCs and retained in their uninfected siblings. Differential migration modes of uninfected and infected DCs did not cause differential maturation, which was found to be identical for both populations. As an underlying mechanism driving this enforced migration, the role of sphingosine kinase (SphK) and sphingosine-1-phosphate (S1P) was studied in MV-exposed cultures. It was shown in this thesis that MV-infection increased S1P production, and this was identified as a contributing factor as inhibition sphingosine kinase activity abolished enforced migration of MV-infected DCs. These findings revealed that MV infection induces a fast push-and-squeeze amoeboid mode of migration, which is supported by SphK/S1P axis. However, this push-and-squeeze amoeboid migration mode did not prevent the transendothelial migration of MV-infected DCs.

Altogether, this 3D system has been proven to be a suitable model to study specific parameters of mechanisms involved in infections in an *in vivo*-like conditions.

Zusammenfassung

Die respiratorische System ist ein wesentlicher physiologischer Bestandteil. Durch die direkte und konstante Verbindung der Atemwege mit der äußeren Umgebung sind sie einer der häufigsten Pfade für den Eintritt von Krankheitserregern in den Körper. Luftübertragene Krankheitserreger wie das Masern-Virus (MV), das in Flüssigkeitströpfchen mitgeführt und von Patienten durch Husten oder Niesen ausgeatmet wird, können über die oberen Atemwege in den Körper gelangen und sich bis in die unteren Atemwege und bis zu den Alveolen ausbreiten. Dort werden diese Krankheitserreger von den dort residenten dendritischen Zellen (DC) oder Makrophagen erworben und zu sekundären lymphatischen Organen transportiert, in denen sowohl virus-spezifische Immunantworten, aber auch – wie im Falle von MV – die hämatogene Dissemination initiiert wird. Der Austrittsmechanismus des MV aus den Atemwegen, insbesondere dessen Übertragung von infizierten Immunzellen auf die Epithelzellen und die Faktoren, die diesen Ablauf bestimmen, wurden jedoch bisher unzureichend untersucht. In Anbetracht der Bedeutung dieser Faktoren für die Virusausbreitung wurde ein komplexes, realitätsnahes in-vivo 3D-Modell der menschlichen Atemwege erstellt. Dieses Modell wurde unter Verwendung von de-zellularisiertem Schweinedarmgewebe als biologischem Gerüst und H358 Epithelzellen als Empfänger etabliert. Dieses Grundgerüst wurde mit Fibroblastenzellen eingebettet. Später wurde auf der basolateralen Seite der Modelle eine Endothelzellschicht eingebracht, um eine Umgebung zu schaffen, die der der Atemwege ähnelt. Somit mussten die Virus-Donoren, MV-infizierte DC durch das

Kollagengerüst wandern und das Virus auf Epithelzellen in einer Nektin-4 abhängigen Weise übertragen. Für die Virusübertragung ist der Zugang infizierter DC zu den Empfänger-Epithelzellen eine wesentliche Voraussetzung, weshalb dieser wichtige Faktor, der sich in der Zellmigration widerspiegelt, in diesem 3D-System analysiert wurde.

Eine erhöhte Beweglichkeit spezifisch MV-infizierter DCs wurde in den 3D-Modellen beobachtet. Dies erwies sich als unabhängig von löslichen Faktoren der anderen Zelltypen in den Modellen. Erhöhte Beweglichkeit infizierten DCs wurde auch in 3D-Kollagenmatrizes gesehen, was auf einen infektionsvermittelten zytoskelettalen Umbau hindeutete, der auch anhand von Zytoskelettpolarisation und Uropodbildung bestätigt wurde. Die MV-Infektion induzierte einen schnellen amöboiden Migrationsmodus in den DCs, der sich als sensitiv gegenüber ROCK-Hemmung erwies. Im Gegensatz zu uninfizierten DCs gleichen Reifungsstadiums waren in infizierten DCs Podosomenstrukturen und Filopodien sowie deren Aktivität stark reduziert. Als potentiell zur verstärkten Motilität infizierter DCs beitragender Faktor wurde die Rolle der Sphingosinkinase (SphK) und des Sphingosin-1-phosphats (S1P) in MV-exponierten Kulturen untersucht. In dieser Arbeit wurde gezeigt, dass die S1P-Produktion durch eine MV-Infektion erhöht wurde, und in der Tat zur für infizierte DCs beobachteten erhöhten Geschwindigkeit beitrug, da diese sensitiv gegenüber Hemmung der Sphingosinkinase-Aktivität war. Diese Ergebnisse zeigen, dass die MV-Infektion einen schnellen amöboid-artigen Migrationsmodus induziert, der von der SphK/S1P-Achse unterstützt wird. Dieser Push-and-Squeeze-Amoeboid-

Migrationsmodus verhinderte jedoch nicht die transendotheliale Migration von MV-infizierten DCs.

Insgesamt hat sich dieses 3D-System als geeignetes Modell erwiesen, um die spezifische Parameter von Mechanismen von Infektionen in einem *in-vivo*-ähnlichen Zustand zu untersuchen.

1 Introduction

1.1 Respiratory tract

Lung functions as the respiratory center of the human body. It controls the air circulation through the complex network of the respiratory tract from trachea deep down to alveoli (1).

The respiratory tract is the most prevalent gate for virus entry. This complex system consists of many parts and tubes for exchanging the air between the body and environment. Every individual inhales a great volume of air every minute, possibly containing viral droplet and particles from sneeze or cough of an infected person (2).

The respiratory tract is divided into two main parts, the upper respiratory tract, and lower respiratory tract. The upper respiratory tract consists of the nose, nasal passages, sinuses, pharynx, and larynx. Larger droplets can get stuck in the upper respiratory tract, while smaller particles or liquids can get deeper into the lower respiratory tract which consists of the trachea, bronchi, and lungs. Bronchi divide into smaller bronchioles which have a pulmonary acinus, each containing 10,000 alveoli and in total around 300 million alveoli, responsible for the gas exchange (2, 3).

1.1.1 The airway epithelium

A pseudostratified epithelium lines the upper respiratory tract. It contains mucus-producing goblet cells and ciliated cells, which co-function to push the mucus with the trapped pathogens or external suspensions (like dust) to the digestive system. A minor

fraction of mucus-secreting goblet cells are present in the lower respiratory tract, and the ciliated cells mostly localize to the beginning of the lower respiratory tract. Immune cells like dendritic cells and macrophages distributed all over the respiratory mucosa and also in the alveoli capture the antigens there by extending their dendrites in between the tight junctions of airway lumen epithelial cells (4).

1.1.2 The extracellular matrix

The extracellular matrix (ECM) is a structural non-cellular part of a tissue. The most common component of the ECM is collagen, a structural protein. In addition to proteins, the ECM also contains carbohydrates, which both are produced by resident cells (5). The ECM serves as a scaffold for the cells and confers the shape and architecture of an organ. In addition to this physical function, it has a major role in mediating biochemical signaling, which controls a vast area of biological events such as morphogenesis and differentiation (6). The ECM in the lung is categorized into two compartments: the basement membrane and the interstitial spaces. The basement membrane is found underneath epithelial and endothelial layers, while interstitial spaces which contain resident fibroblast cells make the lung parenchyma. The major role of these resident fibroblast cells is the production of ECM components (7). The ECM is important for initializing molecular cues, but also for relaying environmental stress signals to cells via cell-matrix interactions as well as for inducing proliferation for tissue regeneration and repair (8).

1.2 Measles virus

1.2.1 Pathogenesis and immune response

Measles is a highly contagious airborne disease which caused more than 2 million worldwide deaths each year before the first vaccine introduction in 1963 (9). Despite effective vaccination and the massive reduction in children mortality, measles caused around 535,000 deaths globally in 2000, and according to the reports in 2017, this number was reduced to approximately 110,000 deaths cases (10). The large recent outbreaks are due to problems in achieving the high vaccination coverage needed to confine infections due to insufficient health control, or geographical, cultural, and economic issues (11). Measles is highly contagious with the basic reproduction rate (R0) reported being 12-18, meaning that among a susceptible population, one measles infected person can on average infect 12-18 other individuals (12). Pneumonia, diarrhea, and acute encephalitis are severe complications of acute measles; however, the majority of severe morbidity and mortality of measles is based on the immunosuppressive potential of measles virus (MV) which favors secondary infections or supports reactivation of persistent infection (9, 13). Virus-specific immune responses are, however, efficiently established which mediate viral clearance and confer lifelong protection against reinfection (14).

The infection starts in the respiratory tract, spreads to the lymphoid tissues followed by a prodromal phase with fever and cough. Thereafter, at the time that Koplik spots appear, the virus is disseminated to the peripheral tissues via infected lymphocytes

(15). The maculopapular skin rash which occurs 3-5 days post prodromal phase, reflects the onset of MV specific humoral and cellular responses as determined by the appearance of antiviral antibodies and virus-specific T cells involving $CD4^+$ and $CD8^+$ T cells which infiltrate sites of MV replication. This initial Th1 response later on shifts to a prolonged Th2 response marked by an increase in IL-4 and IL- 10 and IL-13 and reduced levels of IL-12, thereby suppressing cellular immunity (16–18).

As a late complication, subacute sclerosing panencephalitis (SSPE) develops in rare cases late after acute infection (approximately 1 in 100,000) (19). Viral genes expression in persistently infected brain cells is restricted: while proteins important in viral replication, the N and P proteins, were detected in most infected brain cells, expression of viral envelope proteins varied between patients and was generally low (20).

1.2.2 MV structure and main receptors

MV belongs to the Morbillivirus species of the Paramyxoviridae family. MV has a negative-sense single-stranded RNA genome of about 16,000 nucleotides. The viral RNA is encapsidated by nucleoproteins (N) forming a helical ribonucleoprotein (RNP) complex (Figure 1). The viral RNA-dependent Large polymerase protein (L protein) and phosphoprotein (P) are attached to the RNPs. The lipid envelope of the virus is acquired by budding from the host cell plasma membrane. While a matrix protein (M) layer lines the inner side of the envelope, the viral glycoproteins hemagglutinin (H) and fusion (F) proteins are transmembrane proteins projecting from the particle. The P gene

encodes for two additional non-structural proteins, which are V and C proteins (21, 22).

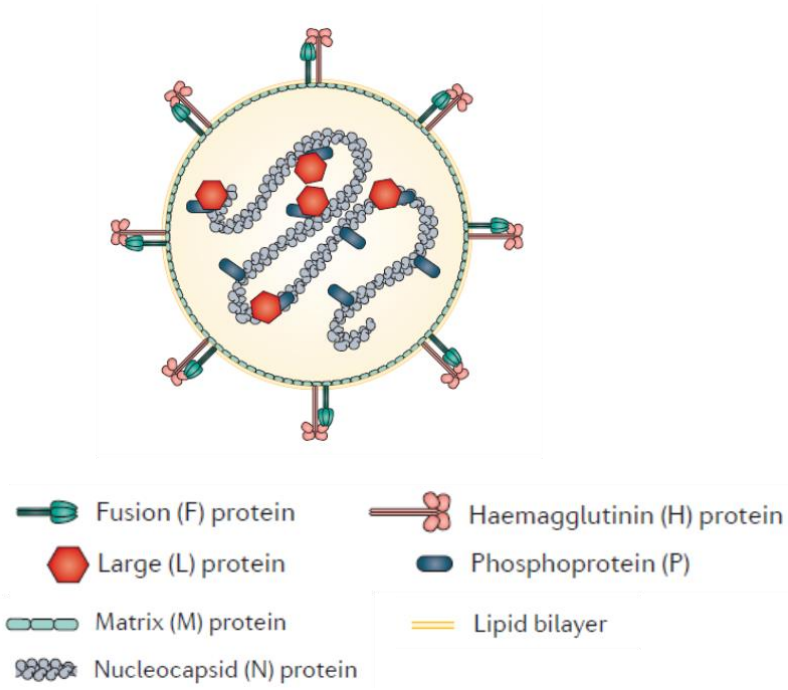

Figure 1 Schematic representation of MV structure.
Source: Rota PA et al., Nat Rev Dis Primers, 2016 (15).

To date, three different cellular receptors binding the MV H protein have been identified: 1) CD46 (membrane cofactor protein), used by attenuated/laboratory MV strain, is a complement regulatory glycoprotein expressed on all human nucleated cells (23). 2) Signalling lymphocyte activation molecule (SLAMF1) or CD150 used by both wild type and attenuated MV strains is expressed on human activated B cells, T cells, monocytes and mature dendritic cells (DCs) and is, therefore, the major receptor mediating immune cell infection as important in MV acquisition, amplification and spread through the hematopoietic compartment (24, 25). 3) PVRL4 (Nectin-4), an

adherence junction protein of the immunoglobulin superfamily expressed on epithelial cells. Nectin-4 is required for MV host exit. It is expressed to low or moderate levels in normal tissues, and highly abundant on transformed cells (26, 27).

1.3 DCs in MV infection and viral transmission

Monocyte-derived DCs have a major role in the initiation and modulation of immune responses. They are also believed to be central to initiating and shaping MV-specific immunity, but also in MV-induced immunosuppression. In common with alveolar macrophages, they are early targets of MV, and most likely serve as Trojan horses mediating viral transport into secondary lymphatic tissues and thereby, initiating spread within the hematopoietic compartment (28, 29). MV infection of DCs is mediated by CD150, which is aided by trapping via DC-SIGN. The latter directly supports viral uptake by MV ligation-mediated activation of the acid sphingomyelinase as important for translocation of CD150 from its intercellular storage compartments to the cell surface (30). Functional consequences of CD150 ligation in DCs are not known. MV-induces phenotypic maturation of DCs as shown by the upregulation of MHC class II and co-stimulatory markers such as CD80, CD83, and CD86 (31, 32). The MV-induced production of IFN type I production by MV was revealed by MxA protein expression in DCs which did not prevent viral spread in DCs while it interfered with viral replication in monocytes and neural cells (20).

It is highly unlikely that $CD150^-$ epithelial cells are initial targets for infection. The nectin-4 expression is confined to the basolateral compartment, and in line with this, infection

of primary epithelial cells *in vivo* and *ex vivo* at the basolateral surface has been documented (31). After first viral replication in local lymph nodes and the subsequent viremia via MV-infected circulating lymphocytes and DCs, these can migrate to the subepithelial layers of the respiratory tract from the blood vessels. There, they might mediate degradation of the basement membrane and travel towards and between epithelial cells and transmit MV to epithelial cells using nectin-4 (15, 32, 33). Efficient MV transmission within the epithelial cell via intercellular membrane pores in primary airway epithelial cells has been reported (34, 35). *In vitro*, basolateral entry of MV into human airway epithelial cells was followed by replication and apical viral release (36). Suggesting that the virus is shed apically from the infected cells into the airway lumen and released into the environment by coughing (32). The schematic representation of MV infection and transmission is illustrated in Figure 2.

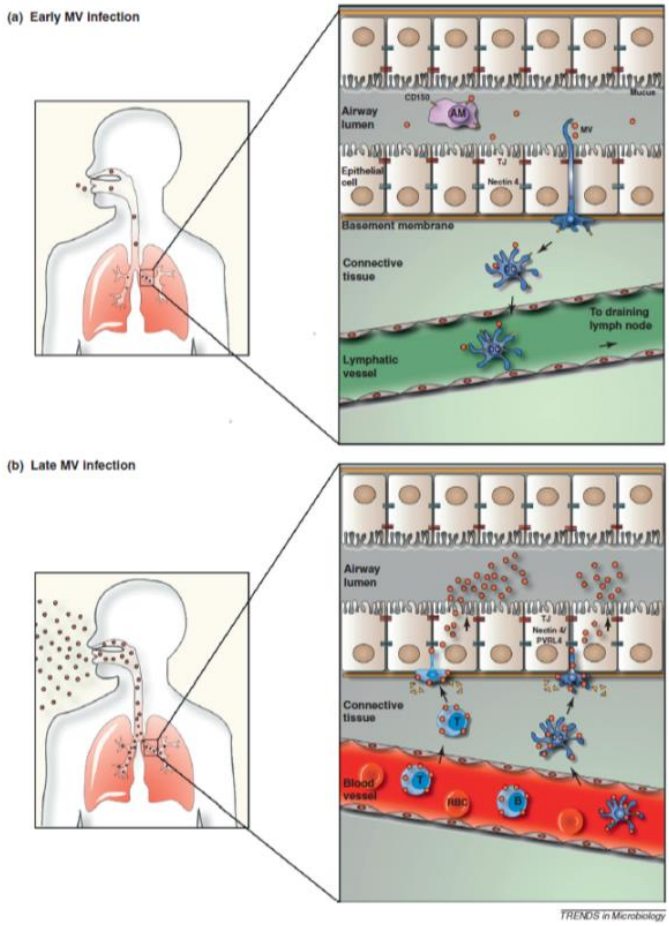

Figure 2 MV infection and transmission mechanism in the host body.
A) The entry of the virus to the airway lumen where they encounter the CD150⁺ DCs or macrophages (AM). DCs may also get infected by capturing the MV via the dendrites which move through the epithelial tight junctions. B) Late in MV infection, the epithelial cells get infected basolaterally via nectin-4, presumably via MV transmission from infected DCs. The virus replicates in and is shed from the apical side of epithelial cells to the lumen and eventually to the environment. Source: Noyce RS et al., Trends Microbiol, 2012 (32).

1.4 DC activation and migration

The ability to migrate is a major prerequisite in DC interactions with both immune and non-immune cells. At both homeostatic conditions and pathogen challenge, DCs need to reach target destinations (37). They locate to most compartments such as skin,

intestine, and lungs. They patrol the environment in search of antigens which they capture, process and transport to the local draining lymph nodes via lymphatic vessels, where they present antigenic peptides on major histocompatibility complex (MHC) molecules to trigger T cell activation and thereby, the adaptive immune response (37). However, considering the importance in DCs functionality, details, and mechanisms of DC migration in complex environments are not fully understood.

Toll-like receptors (TLRs) are important sensors of viruses, bacteria, and parasites, and thereby induce DC activation and maturation. Phenotypically, this can be characterized by upregulation of MHC class II and co-stimulatory molecules such as CD80 and CD86, as well as the changes in surface expression of chemokine receptors. The CCR5 is abundantly expressed on immature (iDCs) and is important in DC recruitment to peripheral sites of inflammation. Upon maturation signals, CCR5 is downregulated while CCR7 expression is induced as essential for recruitment of maturing DCs towards chemokines produced in secondary lymphatic tissues (CCL19 and CCL21) (37–39). MV does not efficiently induce this chemokine receptor switch and impairment of chemotactic responses to CCR7 chemokines is suggested to contribute to MV immunosuppression (40).

1.5 The cell migration modes

Migrating cells, also including DCs, encounter a variety of environmental changes, like those defined by the ECM structure, or by surface structures of interacting cells. These

factors as well as cell type, or protein expression and signaling patterns (cell behavior), can define the individual migration mode (41).

The migration mode defines efficiency and the velocity of this process. Velocity substantially varies from a few microns per hour for some fibroblasts to approximately 10 microns per minute for DC and T cells. The general classification of migration modes originally based on the morphology of the migration patterns distinguished three main categories: proteolytic migration (slow), non-proteolytic integrin-dependent migration (intermediate speed) and non-proteolytic integrin-independent migration (fast) (42). As major categories, cells move either individually (using either an amoeboid and mesenchymal migration mode), or collectively as multicellular units in clusters, sheets, or strands (43).

Amoeboid and mesenchymal modes are at the opposing poles of individual cell migration. The main characteristics of these two phenotypes are summarized in Figure 3.

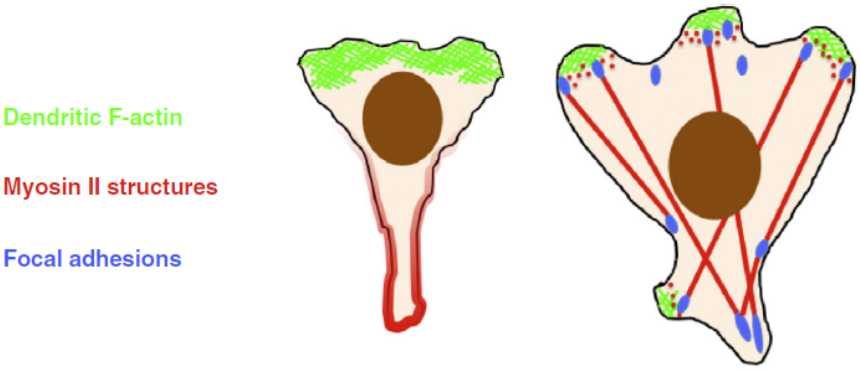

	Amoeboid	Mesenchymal
Migration speed	Fast, ~ 10 µm/min	Slow, < 1 µm/min
Polarity	Well-defined front and rear	Multiple, competing lamellipodia
Adhesion	Relatively weak, mostly intercellular	Strong, mostly ECM with well-defined adhesion complexes
Migration mechanics *in vivo*	Sqeezing through pores in matrix/stroma	Traction via adhesion to ECM, matrix degradation as necessary
Organization of action cytoskeleton	Thick dendritic actin network at the cell front; elsewhere, cortical actomyosin mediates contractility beneath the plasma membrane	Dendritic F-actin in lamellipodia; acto-myosin minifilaments mediate contractility behind the leading edge(s) and form thick stress fibers attached to focal adhesions
Chemoattractant receptors	GPCRs	RTKs

Figure 3 Amoeboid and mesenchymal migration modes.
Source: Bear JE et al., Curr Opin Cell Biol, 2014 (44).

The amoeboid migration phenotype is characterized by fast speed (around 10 microns per minute or more) and is mainly driven by a strong polarization of the actomyosin cytoskeleton (44, 45) with the other cytoskeletal components having a marginal regulatory or supportive role (45). This strong polarization allows movement through the narrow gaps through the ECM by squeezing the cell body and extending pseudopods and blebs. Fast migrating leukocytes, also including DCs mainly use the amoeboid migration type as they should rapidly cover far distances to reach their target tissues (46).

Actin cytoskeletal force is generated by two main elements: network expansion mediated by actin polymerization and network shrinkage mediated by actin contraction, which is the only force which plays the main role in retraction of the cell body. The actual movement requires pulling forces against the direction of movement (45, 47). Both expansion and retraction can contribute to the formation of plasma membrane protrusion. Firstly, actin filament polymerization can promote intracellular trafficking. When happening underneath the plasma membrane, actin polymerization and expansion provided the force required for lamellipodia (sheet-like) and filopodia (finger-like) formation by pushing out the plasma membrane (49, 50). Nucleation of the actin expansion network in lamellipodia formation depends on the Arp2/3 complex (48).

Secondly, actin network contraction also supports the leading edge activity by hydrostatic pressure gradients. Contraction is mainly dependent on myosin II activity, which locally increases the hydrostatic pressure (45).

The mesenchymal mode is mainly driven by actin polymerization through activation of the small GTPase Rac, while the amoeboid mode is promoted by enhanced cell contractility as a result of activation of the small GTPase RhoA followed by ROCK-dependent myosin light chain phosphorylation and myosin II activation (45, 49).

DCs activation has been shown to induce a fast and persistent mode of migration driven by actomyosin cytoskeleton concentration at the cell rear (50). The driving force of mDCs migration in a 3D microenvironment with high confinement is generated myosin II activation (51).

Mesenchymal cell motion is slowed down by integrin-mediated adhesion to the ECM. Formation of adhesive structures and ECM attachment is regulated by the ability of cells to express matrix metalloproteinases for matrix degradation (52). This focalized proteolysis is well established for cells preferentially using the mesenchymal migration mode, such as in stromal cells, has, however been shown for leukocytes (usually using the amoeboid mode) migrating through 3D fibrillar collagen matrices which can be reverted to a nonproteolytic migration mode on inhibition of metalloproteinases (53). If mechanical forces or signaling pathways stabilizing the adhesive structures and the attachments to ECM are weakened, mesenchymal movement can switch towards amoeboid migration, although with differential efficiencies (43).

Podosomes, as formed by motile cells such as DCs, macrophages, and osteoclasts, are dynamic F-actin-based adhesive structures (54). Podosome structures contain an actin core with a ring which is rich in vinculin and paxillin. Podosoms in DCs can be protrusive and remodel and degrade the ECM via membrane-localized metalloproteinases MMP14 at the tip of these structures, which favors the pathfinding in DCs to reach the target destinations (55). Podosoms mediate cell adhesion, mechanosensing, and matrix digestion (54, 56, 57). Podosom dissolution has been reported to be associated with an enhanced amoeboid 3D migration in fibrillar collagen I matrices (58). These structures (also known as invadopodia in cancer cells) are involved in the mesenchymal migration mode, which is protease-dependent and takes place in 3D environments. This behavior has also been seen in DCs by means of myosin II activity and MMP14 dependent matrix degradation (55, 59). TLRs activation

can differentially regulate podosome formation and dissolution and thereby modulate the migration mode. The adopted migration mode does, however, not only depend on maturation because iDCs and mDCs can adopt differential migration modes according to the matrix stiffness, maturation status and respective activated intracellular signaling pathways, and absence/presence of podosomes (60).

1.6 Sphingolipids and Ceramides

Sphingolipids contain a sphingoid backbone. They can be metabolized and generate a wide range of lipid molecules. These molecules include ceramide, sphingosine, and sphingosine-1-phosphate which have a wide variety of biological properties and functions (61, 62).

Sphingolipids are mainly found as structural molecules within membrane bilayers of eukaryotic cells where they designate their physical cellular function. They can be produced in many different pathways via catalyzing an amino acid (predominantly serine) and fatty acid (predominantly palmitate) as basic units for their biosynthesis in the *de novo* pathway (61).

The sphingolipid metabolism is highly complex generating a great number of metabolites with ceramide standing at the center of this biosynthetic and catabolic network (Figure 4). Ceramide consists of sphingosine and a fatty acid chain and can be generated via three main pathways: *de novo*, sphingomyelin breakdown by sphingomyelinases, and the sphingolipid recycling or the salvage pathway (63). Ceramide can be further converted to ceramide-1-phosphate or sphingosine-1-

phosphate via phosphorylation of the 1-hydroxy group of sphingosine produced from ceramide by ceramidase activity. Addition of phosphorylcholine head group or a sugar moiety to ceramides generates sphingomyelin or glycosphingolipids, respectively.

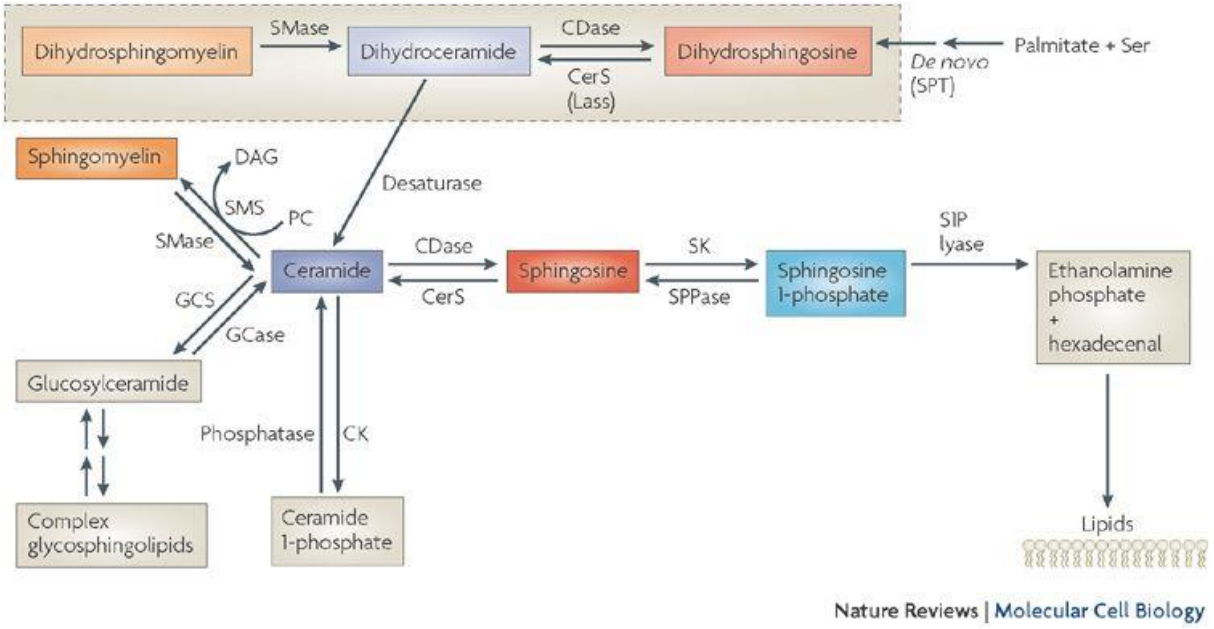

Figure 4 Sphingolipid metabolism.
Source: Hannun YA, Obeid LM., Nature Reviews Molecular Cell Biology, 2008.

Ceramide de novo synthesis is initiated in the ER and involves trafficking to the Golgi where further conversion occurs. Sphingomyelin breakdown into ceramide is catalyzed by the activity of sphingomyelinases. The acid sphingomyelinase (ASM) is compartmentalized in late endolysosomal vesicles from where translocation to the outer plasma membrane leaflet is triggered by external stimuli. The neutral sphingomyelinase (NSM) localizes at the inner leaflet of the plasma membrane and intracellular compartments (62, 64).

1.6.1 Sphingosine-1-phosphate and cell migration

Sphingosine modulates signaling pathways and protein kinases mediating cell cycle arrest and apoptosis (65, 66). S1P is produced by many cell types and its concentration in serum can raise up to 1µM (67). It can be generated from ceramide through ceramide break down by ceramidases and be used as a substrate for sphingosine kinases (SphK) that generate S1P or be regenerated through dephosphorylation by intracellular S1P phosphatases (62).

S1P is a bioactive sphingolipid stimulating a variety of cellular signals mostly associated with cell activation. Following its production by sphingosine kinase 1 or 2 at the plasma membrane (or other membranes), regulation of signaling pathway by S1P may occur directly intracellularly or, best investigated, after S1P export via ABC transporters or spinster channels, after interaction with G-protein coupled S1P receptors (GPCRs) (S1PR1, S1PR2, S1PR3, S1PR4, and S1PR5) (62, 65, 68). The five S1P receptors can initiate different and opposing signaling pathways. S1PR1 and S1PR3 activate the Rac/Cdc42 pathway and thereby can promote cell migration, while ligation of S1PR2 inhibits migration, though in common to S1PR3, it couples to Gi, Gq, and G13. There is a counteraction between Gi and G12/13 regarding Rac activity in migration regulation in a way that Gi leads to Rac activation and migration, while G12/13 ligation gives rise to a Rho-dependent inhibition of Rac and migration. However, these effects mainly apply to chemotaxis and directional migration (69, 70).

The importance and functional role of myosin II at the cell rear of the migrating cells for generating the retrograde flow and cell contraction was described in 1.5. Small

GTPases take part in in the regulation of myosin II and modulation of cell migration as described in leukocytes like neutrophils (Figure 5) (71). RhoA plays a critical role in cell polarization and migration and it has been revealed that RhoA signaling at the rear of motile leucocytes inhibits the Rac signaling and pseudopodia formation there through myosin II regulation (71). RhoA–ROCK signaling axis promotes the phosphorylation of myosin light chain (MLC) which induces the assembly of actin-myosin filaments. However, ROCK function on actin-myosin assembly can be indirect and through the other substrates which are involved in cytoskeletal remodeling (71, 72).

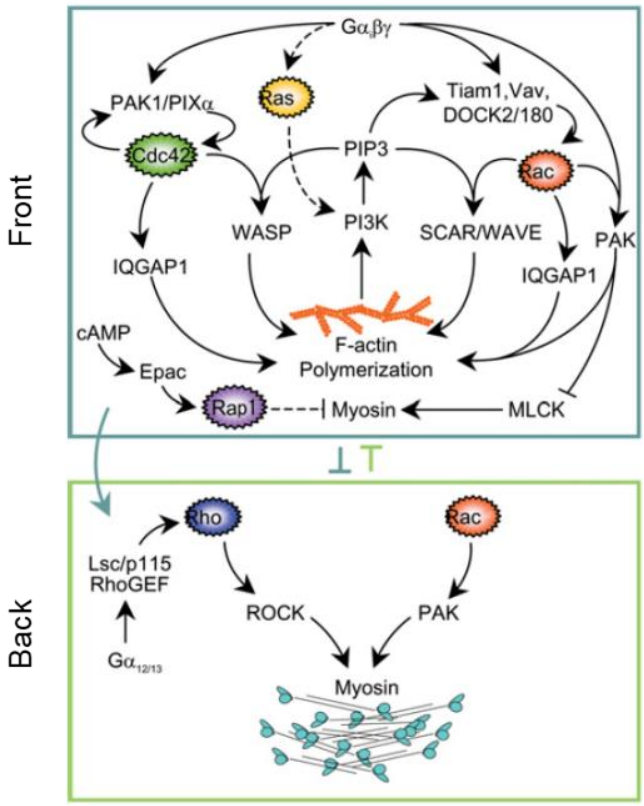

Figure 5 Actin and myosin dynamics regulation by small GTPases in leukocytes.
Source: Charest PG et al., Firtel RA et al., Biochem J, 2007.

1.7 Tissue engineering

The general concept in tissue engineering is to combine biology, biomaterial science, and engineering and thereby, cells and biodegradable scaffolds for tissue repair or regeneration. The most popular used strategy in tissue engineering is to isolate, expand and seed specific cell types of interest in a 3D environment that can mimic the natural physiological cell niche. These 3D environments can be generated using biological scaffolds, resembling the natural ECM (73).

One approach in regenerative medicine is to use ECM obtained from animal tissues as a scaffold for the host cell growth. After isolation from the tissue source and de-cellularization, these ECMs can be used as graft prosthesis and are referred to as bioscaffolds and biomatrices (5). In addition to decellularized matrices (81) scaffold used include porous membrane coated with collagen (74) or 3D hydrogels (75).

An important goal in tissue engineering is the generation of human tissue models to study the human-specific diseases and thereby, to design new therapeutic strategies. This is particularly important in diseases where animal models reflecting essential parameters of the disease in humans are not available (76). There are different approaches for generating the 3D test models depending on the cell type, scaffold, and culture conditions. Taking advantage of a variety of human cell resources (primary, iPS, cell lines) together with the use of different types of scaffolds for better cell adherence and shaping, eventually substituted by the immune cell compartment, experimental models recapitulating specific features of a given human organ can be

established (77, 78). Physical and mechanical cell stimulation are further key issues in 3D test models. These can be provided by different means during cell culture, for instance, by dynamic shear stress, pressure, and tension generated by mechanobioreactors (79).

All in all, using this knowledge together with novel interdisciplinary expertise and complementary techniques, help to develop new strategies and/or advance the current methods for disease modeling, drug screening, tissue transplantation, and regenerative medicine. Developing new techniques using human material will also help the reduction or remove of animal testing and might give rise to broader usage and improvement of translational clinical application of human cells like stem cells in tissue engineering (80, 81).

1.8 Aim of the thesis

This work aimed to generate a complex 3D human respiratory tissue model for studying parameters important in MV exit from the host using tissue engineering techniques and co-culture of several human cell types.

Understanding the migration mediating factors during the MV infection in DCs as well as the MV cell to cell transmission at the late MV infection phase in the respiratory tract is of great importance in the initiation and development of viral egress and transmission. However, this cannot be studied in animal models like mice, because mice are not susceptible and permissive to peripheral MV infection. Therefore, a substitute test model like a complex human 3D model which allows the recapitulation of specific tissue characteristics, like the ECM structures with the respective human cell types is required. In order to study cell migration in this context, the test model should allow the 3D visualization of cells with solid quantitative analysis so that the spatiotemporal data of cellular interactions could be achievable.

In this thesis, a 3D test model with the characteristics described above, based on our previous established model using a biological scaffold embedded with fibroblast cells was generated. To study the impact of MV infection on dendritic cell migration and mimic the viral exit from the host respiratory system, the tissue model was advanced by using human primary dendritic cells and endothelial cells.

2 Materials

2.1 Biological material

Table 1 Biological material

Cells/tissue/viruses	Type	Source
H358 cell line	Human epithelial lung adenocarcinoma	Virology Würzburg
BCi-NS1.1 cell line	Airway epithelium-derived basal cells	Virology Würzburg
CRISPR/Cas9 Nectin-4 KD H358 cell line	Human epithelial lung adenocarcinoma	Self-edited/ Virology Würzburg
BJAB	Human B cell, lymphoblastoid	Virology Würzburg
B95a	EBV transformed marmoset B cell	Virology Würzburg
Vero-hSLAM	African green monkey kidney fibroblasts transfected to express human CD150	Virology Würzburg
HEK 293T	human embryonic kidney cells transformed by SV40 T-antigen	Virology Würzburg
Primary fibroblasts	Human skin dermis layer	Tissue engineering department, Würzburg
PBMCs	Human peripheral blood	Institute for Clinical Transfusion Medicine and Hemotherapy of the University Hospital Würzburg
HUVECs	Human umbilical vein	Virology, Würzburg
Porcine jejunum	Pig (6 weeks, female) (Niedermeyer, Dettelbach)	Tissue engineering department, Würzburg

Wild-type MV	Fleckenstein (WTF)	Virology, Würzburg
Recombinant wild-type MV encoding for eGFP	IC323-EGFP	Virology, Würzburg

2.2 General buffers, media and solutions

Table 2 Chemicals, media and solutions

Media/buffers/solutions	Manufacturer /composition
Acrylamide/bisacrylamaid	AppliChem
Agarose, ultrapure	BioFroxx
APS	Carl Roth
ASM Assay lysis buffer	20 mM HEPES pH 7,4 2 mM EDTA 5 mM EGTA 5 mM DTT 1 mM Na-orto-vanadate 10 mM β-glycerolphosphate protease inhibitor cocktail ad aqua dest.
ATP	Thermo Fischer
ATV	136,89 M NaCl 5,36 M KCl 3,22 M D(+)-glucose 6,90 M $NaHCO_3$ 0,05 % trypsine 0,54 M EDTA ad aqua dest., pH 7,4
BSA	Serva
Citrate buffer stock solution (10X)	42 g/L Citric acid

	17.6 g/L NaOH pellets in demineralized water pH 6.0
Collagen I High Concentration Rat Tail	Sigma-Aldrich
D-*erythro*-sphingosine 1-phosphate	Enzo
DMEM	Gibco
DMSO	AppliChem
dNTP Mix, 10 mM each	Thermo Scientific
EDTA	Sigma-Aldrich
Endothelial Cell Growth Medium Vasculife VEGF	Lifeline cell technology
Eosin	Sigma-Aldrich
Ethanol	AppliChem
FACS buffer	PBS (w/o Ca^{2+}/Mg^{2+}) 0,5 % (w/v) BSA 0,02 % (w/v) NaN_3
FCS	Biochrome AG
First Strand cDNA Synthesis Kit	Fermentas
FITC-Dextran	Sigma-Aldrich
Gel Red	Sigma-Aldrich
Haematoxylin	Carl Roth
HCL	VWR
HCL/EtOH (H&E staining)	6.85%(v/v) HCL, 1M in ethanol (50% v/v)
HEPES	Sigma-Aldrich
Histopaque-1077	Sigma-Aldrich
HMU-PC	Moscerdam Substrates
HMU-PC solution	1,35 mM HMU-PC 0,25 M Na-acetate 30 μM Na-taurochlorate ad aqua dest., pH 7,4 or 5,2
HPLC-grade water	AppliChem
Human Fibronectin	Prospec
Hygromycin	Sigma-Aldrich
Isopropanol	AppliChem

Lysis buffer	1% (w/w) Nonidet P-40 (NP-40) 120mM NaCl 10mM NaF, pH=7.2 50mM Hepes, pH=7.4, 40mM b-glycerophosphat 1mM EDTA 1 tablet protease inhibitors cocktail per 50ml lysis buffer
MEM	Gibco
Methanol	AppliChem
Mounting media	Southern Biotech
Mounting media (Mowiol)	Carl Roth
NaCl	AppliChem
NSM/ASM Assay stop buffer	0,2 M glycine 0,2 M NaOH 0,25 % Triton-X ad aqua dest., pH 11
Paraffin	Carl Roth
Paraformaldehyde (PFA)	AppliChem
PBS	137 mM NaCl 2,7 mM KCl 10 mM Na_2HPO_4 x H_2O 1,8 mM KH_2 PO_4 1 mM $CaCl_2$ x 2 H_2O 0,5 mM $MgCl_2$ x 6 H_2O ad aqua dest.
PBS (w/o Ca^{2+}, Mg^{2+})	137 mM NaCl 2,7 mM KCl 10 mM Na_2HPO_4 x H_2O 1,8 mM KH_2 PO_4 ad aqua dest.
Penicillin/Streptomycin (100 i.e./mL)	Sigma-Aldrich
Phusion® High-Fidelity DNA Polymerase	New England Biolabs
Poly-L-Lysine	Sigma-Aldrich

Propidium Iodide	Immunotools
Protein standard marker for WB	Fermentas
Puromycin	Sigma-Aldrich
Roticlear	Carl Roth
RPMI-1640	Gibco
SDS	AppliChem
TAE-buffer	25 mM Tris 0,57 % (v/v) acetic acid 0,6 M EDTA ad aqua dest., pH 8,0
TEMED	Carl Roth
Tris	Carl Roth
Triton-X	Sigma-Aldrich
TRIzol reagent	Invitrogen
Trypanblue	0,25 % (w/v) in PBS (w/o Ca^{2+} /Mg^{2+})
TWEEN-20	VWR
WB blocking buffer	5 % w/v skim-milk in PBS
WB loading buffer	200 mM Tris pH 6.8 4 % w/v SDS 20 % w/v glycerol 0.02 % w/v bromophenolblue 200 mM DTT
WB washing buffer	PBS/0.05 % Tween-20
Xylene	Carl Roth

2.3 Disposable material

Table 3 Disposable material

Disposable material	Manufacturer
125, 75 25 cm^2 cell culture flasks	Greiner Bio-One
6, 12, 24 well cell culture plates	Greiner Bio-One
96 well flat bottom plate	Falcon
Coverslips for IF slides	Marienfeld-Superior
Cryo-tubes	Greiner Bio-One
FACS-tubes	Falcon

µ-Dish 35 mm, high	ibidi
Leucocyte reduction chambers	University Hospital Würzburg
Petri dishes	Greiner Bio-One
Pipette tips	Brand
Plastic pipettes (5, 10, 25 mL)	Sarstedt
Plastic tubes (50, 10 mL)	Greiner Bio-One
Reaction tubes (0.5, 1.5, 2.0 mL)	Eppendorf
µ-Slide VI 0,4	ibidi
Sterile Filter (Attachement for Disposable Syringes): Diameter 50 mm, Pore Size 0.2 µm	Sartorius Stedium Biotech
Syringe (60 mL)	Infuject
Cell scrapers	Hartenstein
Grease pencil	Dako
Scalpel blades	Hartenstein
Whatmann filter paper	Hartenstein
Nitrocellulose membrane	Hartenstein
PCR tubes	Eppendorf
Pasteur pipettes	Hartenstein

2.4 Cytokines and inhibitors

Table 4 Cytokines and inhibitors

Cytokine/Inhibitor	Manufacturer
FIP	Bachem
GM-CSF	Berlex
IL-4	Miltenyl Biotec
Y27632	Cayman
Amitriptyline	Sigma-Aldrich
SKI-II	Sigma-Aldrich
VPC23019	Cayman
LPS	Sigma-Aldrich

2.5 Antibodies and dyes

Table 5 Antibodies and dyes

Antigen/Target	Catalog No.	Manufacturer	Dilution
Phalloidin ATTO643	AD 643-81	ATTO-TEC	1:200 (IF, FACS)
Cell proliferation dye eFluor 670	65-0840-90	Affymetrix	5 µM
IF secondary antibodies		Life Technologies	
Alexa 555 chicken-α-mouse			1:100
Alexa 647 goat-α-mouse			1:100
Alexa 647 goat-α-rabbit			1:100
Alexa 568 goat-α-mouse			1:100
Annexin V	4317907	Affymetrix	1:100 (FACS)
MV-N, F227		Institute	1:100 (FACS)
αCD14-PE	21620144S	immunotools	1:100 (FACS)
αCD11c-FITC	21487113	immunotools	1:100 (FACS)
αCD86-APC	555660	BD Pharmingen	1:100 (FACS)
αHLA-DR-FITC	1638	Immunotech	1:100 (IF, FACS)
αCD80-FITC	21270803	Immunotools	1:100 (FACS)
αpERM	3149	Cell Signalling	1:200 (IF)
αNectin-4	337516	R & D technology	1:50 (FACS) 1:200 (WB)
αvimentin	Ab8069	Abcam	1:100 (IF)
αE-cadherin	610181	Becton Dickinson	1:100 (IF)
αvinculin	V9131	Sigma-Aldrich	1:200 (IF)
αVE-cadherin	RB01	R&D systems	1:200 (IF)
αFilaminA	MA5-31975	Thermo Fisher	1:1000 (WB)

			1:50 (FACS)
αDC-SIGN-647	330111	Biolegend	1:100 (IF) 1:50 (FACS)
αCas9	14697	Cell signalling	1:500 (WB)
αβ-actin	MA5-15739	Thermo Fischer scientific	1:1000 (WB)
Sphingosine 1-phosphate	LT1002	Echelon Biosciences	1:50 (IF,FACS)
NucBlue live cell stain	1855818	Thermo Fischer scientific	

2.6 Equipment

Table 6 Equipments

Equipment	Manufacturer
Accu-jet pro	Brand
Agarose-Gel Chamber	Virology, University Würzburg
Cell crowns	Tissue engineering and regenerative medicine department
Centrifuge Mikro 200	Hettich
Centrifuge Rotanta 460 R	Hettich
Confocal microscope LSM 780	Zeiss
Embedding station	Thermo fisher scientific
FACS LSR II	Becton Dickinson
FACScan Calibur	Becton Dickinson
Fluorescent microscope Biorevo BZ9000	Keyence
Fluorescent microscope DMi8	Leica
Heating block	Liebisch
Incubator 37 °C, 5 % CO_2	Heraeus
Laminar workflow	Gelman
Microliter pipettes	Brand, Eppendorf
Neubar cell counting chamber	Hartenstein
Paraffinized tissue floating bath: type 1052	Medax
PCR cycler	ML Research

PH meter	Mettler Toledo
Safire2 – Fluorescence plate reader	Tecan
Shaker platform WS5	Edmund Bühler
Sliding microtome RM 2255	Leica
Steam cooker: MultiGourmet	Braun
Vortex Mixer	Neo Lab
Water bath	Kotterman

2.7 Software

Table 7 Softwares

Software	Company
CellQuest Pro	Becton Dickinson
FlowJo	FlowJo
GraphPad Prism 6	GraphPad Software Inc.
ImageJ	NIH
Imaris Bitplane 8.4	Oxford Instruments
Keyence BZ-II viewer and analyzer	KEYENCE Deutschland
Tecan-i-controlTM 1.7	Tecan
BD FACSdiva	Becton Dickinson
Citavi 6	Citavi
Chemotaxis tool	NIH
Office excel 2013 Office powerpoint 2013 Office word 2013	Microsoft Deutschland GmbH
OriginPro 2017	OriginLab
Affinity Designer	Affinity Serif

3 Methods

3.1 Cell culture

3.1.1 Adherent cell culture

Cells were cultured in cell culture plastic flasks in a humified incubator at a temperature of 37 °C and a 5 % CO_2 atmosphere. H358 cells, HEK 293T and VerohSLAM cells were cultured in RPMI 1640 Media, supplemented with Penicillin/Streptomycin (100 i.e./mL) and 10 % heat-inactivated fetal calf serum (FCS) and B95a cells were cultivated in 5% FCS containing antibiotics. Serum was heat-inactivated at 56 °C for 30 min. After reaching confluency, cells were detached by trypsinization using ATV and split at a ratio of 1:3 for H358, 1:3 for HEK 293T, 1:5 for VerohSLAM and 1:3 for B95a. For culturing CRISPR/Cas9 nectin-4 KD H358 cells the medium used for H358 wild type cells was supplemented by 1 µg/mL puromycin for selection of CRISPR/Cas9 expressing cells. Primary dermal fibroblast cells were cultured in DMEM containing 10% FCS and antibiotics. After reaching 90% confluency, these were split at a ratio of 1:3, seeded in fresh flasks and kept until passage 5. Human umbilical vein endothelial cell (HUVECs) were cultured in Endothelial cell growth medium (Vaculife) containing additives as listed in the table below.

Table 8 supplements and growth factors in endothelial cell growth medium

Product	Final concentration in the medium
rh FGF basic	5 ng/mL
Ascorbic Acid	50 µg/mL

Hydrocortisone Hemisuccinate	1 µg/mL
FBS	2%
L-Glutamine	10mM
rh-IGF-1	15 ng/mL
Rh EGF	5 ng/mL
Rh VEGF	5 ng/mL
Heparin Sulfate	0.75 U/mL
Gentamicin	30 mg/mL
Amphotericin B	15 µg/mL

Cells were cultured until 80% confluency, detached by trypsinization using ATV for about 5 min in 37°C, resuspended and split at a ratio of 1:3 in fresh flasks and kept until 3-4 passages.

3.1.2 Suspension cell culture

BJAB cells were cultured in RPMI1640 with 10% FCS and antibiotics. For splitting, cells were pelleted by centrifugation at 1600 rpm for 5 min at 20°C, resuspended in an appropriate volume of culture media according to the used flask size. Cells were passaged every three days.

3.1.3 Thawing and cryopreservation of cells

Frozen samples were quickly thawed in a water bath, rapidly diluted by the addition of 9 mL of pre-warmed complete culture medium and centrifuged at 1600 RPM for 5 min. The supernatant was removed, cells were resuspended in fresh warm culture media and transferred to appropriate culture flasks.

For cryopreservation, cells were harvested at the optimal rate of growth with more than 75% viability by trypsinization, pelleted by centrifugation, resuspended in 1 mL freezing medium containing FCS + 10% DMSO and transferred to -20 for 2h and subsequently to -80 for overnight. Finally, cells were transferred to -140°C.

3.1.4 Isolation of PBMCs and DC generation

Peripheral blood mononuclear cells (PBMCs) were from blood samples obtained with permission of the ethics committee of the medical faculty from the department of transfusion medicine of the Universitätsklinikum Würzburg as leucocyte reduction chambers. First, samples (~8 mL) were diluted with PBS 1:5 (final volume around 50 mL) and layered onto Histopaque in a 50 mL centrifuge tube (25 mL diluted blood to 9 mL Histopaque). Density gradient centrifugation was performed at 160g for 30 min at RT to separate the PBMC layer, which can be isolated from the gradient. The schematic representation of blood cell layers before and after the gradient centrifuge is illustrated in Figure 6.

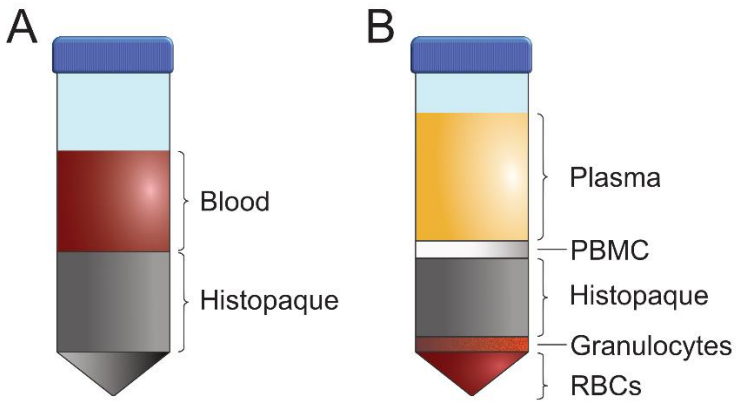

Figure 6 Schematic representation of Histopaque density gradient centrifugation.
A) Layers of blood and Histopaque before centrifugation. B) Blood cell layers after centrifugation.

After removal of the upper plasma containing layer, PBMCs were recovered, washed three times with 50 mL PBS, centrifuged each at 1600 RPM for 5 min and resuspended in RPMI with 5% FCS to a density of 5×10^6 cells/mL.

From these, monocytic cells were isolated either by plastic adherence or via the positive selection using CD14+ cells microbeads. For plastic adherence, the cell suspension was transferred into 75 cm^2 cell culture flasks and incubated for 2h at 37 °C in the incubator to allow adherence of monocytic cells. After 2h incubation time, the culture medium containing the non-adherent B and T cells was removed, and fresh cell culture medium (RPMI + 10% FCS) was added to the adherent monocytes.

For monocyte selection via CD14, the cell suspension was exposed to magnetic microbeads coated with anti-CD14-antibodies and subsequently loaded onto a MACS column placed in the magnetic field of a MACS separator. Thereby, cells labeled by the beads are retained in the column, and the unlabeled cells (depleted from CD14+

cells) flow through. After removing the column from the magnetic field, the CD14+ cells are recovered from the column.

For both methods, the purity of monocytes was determined by CD14 staining for 30 min at 4°C and washing twice with PBS by flow cytometry.

Monocytes obtained by either method were differentiated into immature dendritic cells (DCs) by culture in RPMI supplemented with 10 % FCS and human GM-CSF (500 U/mL) and IL-4 (250 U/mL) for 5-6 days, with fresh cytokines added every two days. When indicated, these immature DCs were matured by addition of 100 nM LPS to the cell culture medium overnight. After six days of DCs differentiation, these were phenotypically characterized using dendritic cell markers.

3.1.5 Generation of the human 3D respiratory tract model using small intestine submucosa without mucosa (SIS$^-$)

In order to culture cells in a 3D system, the biological collagen scaffold SIS was fixed between two metal rings which are called cell crown. To this end, the SIS was cut, opened, and divided into smaller pieces using sterile surgical scalpel and forceps under the laminar flow hood. The small pieces were moved onto the inner ring of sterile cell crowns in a way that the luminal side of SIS faced inward. The SIS was subsequently fixed into the cell crown by placing the bigger outer ring onto the inner ring. Next, the cell crown was turned upside down and placed into a 6-well-plate (Figure 7) (82).

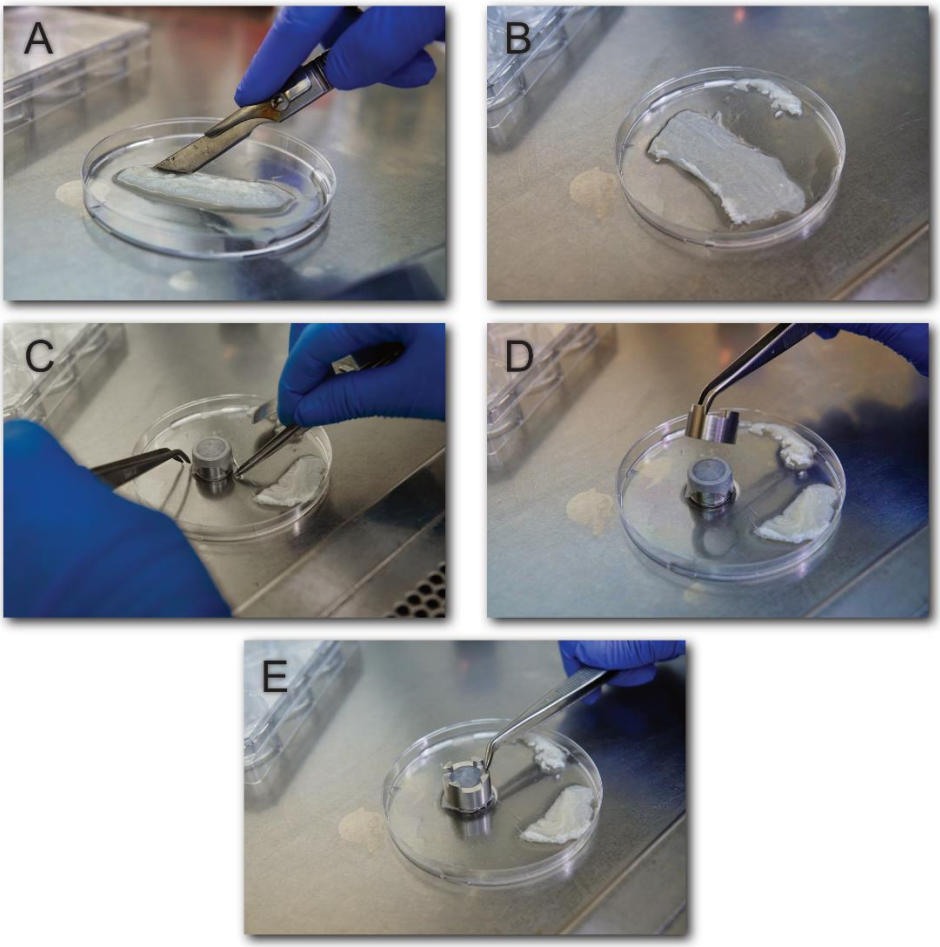

Figure 7 Generation of the human 3D respiratory tract model.
A)The SIS scaffold was cut along one edge, B) it was opened and cut in smaller pieces, C) the small pieces were moved onto the smaller inner ring with the lumen side facing inward, D) the bigger outer ring was placed onto the inner ring, and E) the scaffold was tightly fixed between the two rings.

Cell crowns containing the scaffold were kept in a cell culture medium for at least 2h before seeding of cells. Primary human fibroblast cells (50,000 cells/cm2) were suspended in 500 µL DMEM medium added to the apical side of the cell crown and incubated for at least 1h at 37°C in the incubator. The outer compartment (inside well)

was then filled with 2 mL and inner compartment (inside the cell crown) with 1 mL of the respective culture medium. The whole construct was incubated further for 48 h.

Next, epithelial cells (H358 or BCi-NS1.1) (200,000 cells/cm^2) suspended in 500 µL culture medium were added to the apical side of the cell crown. The cell culture medium used for the culturing the 3D models from this step on was a 1:1 mixture of fibroblast cells medium with the respective epithelial cells medium.

In case endothelial cells were added to the system, the cell crown was turned upside down after the fibroblast addition step, the HUVECs suspended in 25 µL culture medium were added onto the basolateral side of the cell crown (500,000 cells/cm^2) and incubated for 3h. Every 20-30 min 15 µL culture medium was added to the scaffold to avoid the drying of the collagen (question see above for the origin of the collagen). The whole construct was further incubated for 48h followed by seeding of epithelial cells onto the apical surface. The culture media was mixed in the following ratio: 50% endothelial cell medium, 40% RPMI with 10% FCS, and 10% DMEM with 10% FCS.

In order to introduce the fully differentiated DCs as described earlier (3.1.4) to the construct, the cell crown was turned upside down, DCs suspended in 25 µL of culture medium were applied onto the basolateral compartment of the cell crown. After 1h, the construct was turned back to the initial orientation. Every 20 min 15 µL culture medium was added to the scaffold to avoid the drying of the collagen.

3.2 Histology

3.2.1 Tissue fixation and paraffin embedding

In order to characterize the general morphology of the 3D models as well as the cellular compartments, the whole models were fixed. For this, they were washed once with PBS and then fixed by 4 % paraformaldehyde (PFA) for 30 min RT or 1 h 4°C. Following a further washing step in PBS fixed samples were wrapped in a Whatman paper and placed in labeled paraffin embedding cassettes which were floated in tap water to remove remaining PFA and then loaded into the embedding station. After paraffin embedding, samples were floated in liquid paraffin at 60°C, removed from the embedding cassettes and cut into approximately equal pieces. These were transferred into the molten paraffin inside the mold followed by cooling down the mold and creating the paraffin block. Paraffin sectioning was performed using a sliding microtome (Leica) with 5 µm thickness and dried at 37°C overnight.

3.2.2 Deparaffinization and rehydration of tissue sections

Prior to staining, the paraffinized tissue sections had to be deparaffinized and rehydrated. The deparaffinization and rehydration procedure of the samples (Table 9) was preceded by incubation at 60°C for 30 min.

Table 9 Deparaffinization and rehydration protocol

Process	Reagent	Duration (min)
Deparaffinization	Xylene I	10 min
	Xylene II	10 min

Rehydration	Ethanol 96% I	3 times dipping
	Ethanol 96% II	3 times dipping
	Ethanol 70%	3 times dipping
	Ethanol 50%	3 times dipping
	Deionized water	Immersed shortly

3.2.3 Hematoxylin & Eosin (H&E) staining

In order to check the general morphology and the barrier integrity, H&E staining was performed according to a standard protocol below (Table 10).

Table 10 H&E staining protocol

Procedure	Reagent	Duration (min)
Staining basophilic structures	Hematoxylin	6
Rinsing	Deionized water	3 (Until the solution is clear)
Differentiating Hematoxylin	HCL/Ethanol	2 times dipping
Rinsing	Deionized water	Dipping once
Bluing	Tap water	5
Staining acidophilic structures	Eosin	6
Rinsing	Deionized water	3 (Until the solution is clear)

Dehydration	Ethanol 70%	3 times dipping
	Ethanol 96%	2
	Isopropyl I	5
	Isopropyl II	5
Cleaning	Xylene I	5
	Xylene II	5

3.2.4 Immunofluorescence staining of sectioned tissues

Cellular compartments of the tissue samples were characterized by immunofluorescence staining using specific cell markers. Prior to staining, tissues were deparaffinized (Table 9) and the epitopes were unmasked from fixation slides were treated with heat in a steamer containing citrate buffer pH 6 for 30 min at 95-100°C. Sections were then kept at RT for 20 min, washed in PBS for 15 min and permeabilized with 0.1% Triton X 100 for a maximum of 5 min at RT. After a blocking step for at least 30 min using 5% BSA/PBS (albumin fraction V), primary antibodies were applied at the appropriate dilution (1:100 if not mentioned otherwise) overnight at 4°C. In the case of double staining, primary antibodies from different species were combined in one solution. Next, sections were washed with PBS/Tween20 three times for 3 min. Secondary antibodies were applied at the appropriate dilutions and incubated for 1h at RT. After three final washing step with PBS/Tween20 (each 3 min), slides were mounted with ready to use Mowiol mounting medium containing DAPI.

3.2.5 Immunofluorescence staining of tissues

Cellular compartments of the 3D tissue models without paraffin embedding and sectioning were characterized by immunofluorescence staining of the complete fixed tissue. Models were washed once with PBS and then incubated with PFA 4% for 30 RT or 1h 4°C followed by washing twice 5 min with PBS on a shaker. Then, the samples inside the cell crown were permeabilized with 0.1% Triton X 100 for 5 min at RT, and tissues were blocked for at least 1h using 5% BSA/PBS at RT. Primary antibodies used at appropriate dilution (1:100 if not mentioned otherwise) were added to the inner side and outer side (in the well) of the cell crown and incubated overnight at 4°C. Samples were washed with PBS/Tween20 three times for 3 min. Secondary antibodies were applied at the appropriate dilutions and incubated for 1h at RT. After three final washing step with PBS/Tween20 (each 3 min), the cell crown was removed from the well plate, flipped upside down, and the outer bigger ring was cautiously removed. The inner ring with the tissue on the top was placed on a microscopic slide using a forceps, the tissue was then spread on the slide, and the ring was removed. After 2 min RT incubation in a horizontal position, the tissue was mounted with a ready to use Mowiol mounting medium containing DAPI.

3.3 FITC-dextran assay

FITC-dextran was used for measuring the permeability of the 3D tissue models and the epithelial cell barrier function. FITC-dextran (4 kDa) was dissolved in the cell culture medium a final concentration of 0.25 mg/mL and filtered using a 0.2 µm pore size. For

the assay, the medium of the models was replaced by fresh medium and incubated at 37°C for 30 min. Before apical addition of the FITC-dextran solution. After a 30 min incubation time at 37°C in the incubator, 100 µL from the basolateral compartment or the apically added solution were transferred into a black 96-well-plate and absorption was measured at an excitation of 490 nm and emission of 525 nm with an ELISA-reader (Tecan infinite 200, Switzerland). Values obtained for the apically added medium were defined as 100 percent (the FITC-dextran solution). Permeability for FITC-dextran was calculated in percentage according to the dilution of the FITC-dextran solution by basolateral medium volume. A model containing only the collagen scaffold served as control.

3.4 TEER measurement

The barrier integrity of the 3D models was measured by the transepithelial electrical resistance (TEER). The Millicell-ERS device was used for measuring TEER values. A culture medium similar to that used in 3D models was used for testing the electrodes and calibration. Prior to TEER measurement, the model cultures medium incubated for 30 min at 37°C with fresh medium. The electrodes of the device were sterilized by soaking in 70 % ethanol for 10 min followed by drying under the laminar hood. The longer electrode was then placed in the outer compartment (basolateral, in well), the shorter in the inner compartment of the cell crown (apical). The measurement was continued until the TEER value displayed was stable. Finally, values from the models containing only the collagen matrix were subtracted from those containing cells.

3.5 Bacterial transformation and plasmid isolation methods

3.5.1 Transformation of bacteria

Ecoli XL10-Gold ultracompetent cells were used to amplify for plasmid amplification. 50 ng of plasmid DNA were added to 50 µL of bacteria, mixed, vortexed gently, incubated 30 min on ice and then for 1min at 42°C in a water bath followed by cooling on ice for 5 min. 1 mL of antibiotic-free Lennox L Broth (LB) medium was added to the bacteria which were incubated for 1h on a shaker at 220 rpm at 37°C. 50 µl of this bacterial culture was then spread on an LB agar plate surface, containing 100 µg/ml of Ampicillin or 100 µg/ml of carbenicillin which were incubated at 37°C for 24h. Colonies formed were selected and further inoculated in LB medium for Miniprep and Maxiprep plasmid isolation.

3.5.2 Glycerol stock preparation

Briefly, a single bacterial colony from the plate was added to 5 mL of LB medium containing antibiotics, gently vortexed and incubated at 37°C on a shaker at 220 rpm overnight. 850 µL of this culture were gently mixed with 150 µL of sterile glycerol, transferred to screw-capped tubes and stored at -80°C.

3.5.3 Miniprep and Maxiprep plasmid isolation

A single bacterial colony from the LB agar plate or 10 µL of colony suspension was inoculated in 5 mL of LB medium containing antibiotics and incubated in a bacterial shaker at 220 rpm overnight at 37°C. The plasmid Miniprep isolation was performed using the QIAGEN Plasmid Mini Kit according to the manufactures instruction. The

isolated plasmids were then diluted in 50 µL of TE buffer, and the O.D. was measured using the photometer device and used for restriction enzyme digestion to verify their identity. For maxipreparation, 2 mL of the amplified bacterial colony was added to 200 mL of LB medium containing antibiotics and incubated in a bacterial shaker at 220 rpm overnight at 37°C. Bacteria were then recovered by centrifugation at 6000×g for 15 min at 4°C, and plasmid DNA was isolated using “QIAGEN Plasmid Maxi Kit” according to manufactures instruction. The plasmid DNA was resuspended in TE buffer at the final concentration of 1 µg/µl and stored at -20°C.

3.6 Generation of CRISPR-Cas9 edited cells using a lentiviral system

3.6.1 Transient transfection of cells

PEI was used for expression of plasmid-encoded genes in HEK 293T. These were seeded in a 6-well-plate at the density of 1 x 10^6 cells per well and incubated at 37°C for 24 h and were up to 80% confluency. The medium was replaced by MEM 10% FCS without antibiotics 5h prior to transfection. Two mixtures were prepared in separate tubes. Mix 1: PEI + 150 mM NaCl (vortex for 1 min) and Mix2: Plasmid DNA + 150 mM NaCl (for 1 µg of total DNA add 4µl of PEI). Mix 1 and Mix 2 were combined, mixed by gentle pipetting and incubated at room temperature for 20-30 mins to enable the formation of DNA-PEI complexes which were then applied as droplets onto the cells kept at 37°C. The medium was replaced the next day of transfection with an antibiotic-free medium and cells were incubated further for 24-48h.

3.6.2 Generation of lentiviral particles

For lentiviral delivery of the Cas9 gene into H358 cells, a packaging system using psPAX2 and pVSV-G packaging plasmids together with cas9 lentiviral construct was used. Transfection of HEK 293T cells for this purpose was carried out as described above with mixture 1 (PEI mix) containing 50 µl PEI + 600 µl 150 mM NaCl (vortexed for 1 min) and mixture 2 containing 3µg Cas9 lentiviral construct (pRSGCCH-U6-sg-HTS6C-CMV-Cas9-2A-Hygro, Cellecta, California, USA) + 4µg psPAX2 + 4µg pVSV-G + 600 µL sterile 150 mM NaCl (mixed and vortexed). The supernatant containing viral particles was harvested after 2 to 3 days post-transfection. Cell debris was removed by centrifugation at 2000-3000 RPM at 4°C in 50 mL centrifuge tubes and subsequent sterile filtration (0.2 µm filter pore size) followed by either freezing aliquots at -80°C or concentration. For this, the supernatant was transferred in 15 ml centrifuge tubes and centrifuged at 160×g for 5 minutes at 4°C. The viral supernatant was transferred to a tube containing cold PEG-it (PEG it ratio 1:4) and mixed by gentle inversion. The tubes were incubated overnight at 4°C and then centrifuged at 1500×g for at least 1h at 4°C. The supernatant was immediately removed and the pellet was re-suspended in 1/100 ratio of the original volume of sterile cold PBS/1% BSA (100 fold concentration). Aliquots were transferred to cryovials and stored at -80°C.

3.6.3 Lentiviral transduction

H358 cells which were seeded in a 6 well plate at the density of 1 x 10^5 cells per well and incubated at 37°C for 24 h. Cell monolayers were washed once with serum-free MEM before supernatants containing or concentrated lentiviral particles were added.

To increase the efficiency of transduction and obtain maximum expression of target genes, plates were centrifuged at 400×g for 30 min at 37°C and then incubated at 37°C for 48h. Transduced cells were cultured for three days to achieve sufficient confluency, followed by the selection of hygromycin-resistant cells (resistance provided through the integrated Cas9 construct). Subsequently, the cas9 gene expression was estimated by semi-quantitative PCR and western blot.

The Nectin-4 sgRNA used in this study is a lentiviral sgRNA vector in which the gene-specific CRISPR RNA (crRNA) and the trans-activating CRISPR RNA (tracrRNA) are expressed as a chimeric single guide RNA (sgRNA) under the control of a human U6 promoter. Puromycin resistance gene expression allows the rapid selection of cells with the integrated sgRNA. Plasmid preparation and isolation, transfection, and the packaging system used for generating nectin-4 sgRNA lentiviral particles was performed as described above (3.5, 3.6.1, and 3.6.2). The lentiviral Nectin-4 sgRNA construct (GSGH11838-246559205, Dharmacon, Cambridge, UK) was used with the described packaging plasmids for production of lentiviral particles. Lentiviral transduction was performed as described above, followed by the selection of puromycin cells with the integrated sgRNA construct after three days. The transduction procedure was repeated twice to increase the efficiency of nectin-4 knockdown via the CRISPR-Cas9 system. Subsequently, Nectin-4 gene expression was measured by flow cytometry.

3.7 RNA isolation, cDNA synthesis, and PCR

3.7.1 RNA isolation and cDNA synthesis

For RNA isolation by TRIzol, 1×10^6 H358 cells (transduced or not) were pelleted and resuspended in 1 mL TRIzol. Samples were then incubated at RT for 5 min and subsequently, 200 µL chloroform was added, gently mixed in by inversion for 15 s followed by incubation for 3 min at RT. Samples were centrifuged at 15000×g for 15 min at 4 °C for separation of phases containing RNA (upper aqueous phase), proteins (lower organic (chloroform) phase) and DNA (interphase). The RNA containing phase was transferred to a fresh tube, mixed with 500 µL isopropanol and 10 µg RNase-free glycogen and centrifuged for 10 min at 15000×g at 4 °C. After removal of the supernatant, the RNA was washed with 1 mL of 75 % ethanol followed by centrifugation at 8500×g for 5 min at 4 °C. The RNA pellet was resuspended in 30 µL HPLC water and incubated on a heating block at 55 °C for 10 min. An aliquot of the solution was used for measuring the RNA content, the remainder was aliquoted and stored at -80 or used for cDNA synthesis by reverse transcription using the First Strand cDNA Synthesis Kit. RNA amounts ranged from 1 to 5 µg and oligo $(dT)_{18}$ primers were used in a final volume of 20 µL according to the manufacturer's instructions. The cDNA was aliquoted and stored at -20°C for further use.

3.7.2 PCR reaction

For the PCR reaction was carried out using the Phusion high-fidelity kit. The following mix in Table 11 was prepared in a 0.5 µL PCR tube to start the PCR reaction.

Table 11 PCR reaction mix

Component	Final concentration/volume
5X Phusion HF buffer	4 µL (1X)
dNTPs	10 mM (0,4 µL)
Forward primer	10 µM (1 µL)
Reverse primer	10 µM (1 µL)
DMSO	0,6 µL (3%)
Phusion DNA polymerase	0,2 µL (0.02 U/ µL)
cDNA	2 µL
Nuclease-free water	Add to 20 µL

Cas9-specific primers used in this PCR reaction:

Forward primer: CCCCGGTGAGAAGAAAAATGG

Reverse primer: CGTTGTCAAAGGTCCGTTGCT

The used PCR conditions are listed in Table 12.

Table 12 PCR program

Step	Temperature	Time	Cycle
Initial denaturation	95°C	5 min	
denaturation	95°C	1 min	35
Primer annealing	63°C	30 sec	
Elongation	72°C	30 sec	

Final elongation	72°C	10 min
Store	4°C	∞

After the PCR was finished, 2 µL of the PCR product were mixed with 2 µL Gel Red, loaded onto a 2 % agarose/TAE gel and bands were detected under UV light.

3.8 Flow cytometry

Flow cytometry relies on the ordering of the sample into a stream of single cells achieved by a fluidic system. Cells individually pass a laser beam which enables detection of cell size shown by forward scatter (FSC), granularity and internal structure calculated by side scatter (SSC) and fluorescently labeled cell markers Measurement of these optical and fluorescent characteristics provides quantitative information on individual cell populations within one sample. In this study, flow cytometry was performed using the BD LSR II or BD FACSCalibur, data analysis was performed by CellQuestPro or FlowJo 10.4.2 software. Adherent cells were detached by ATV, in case of cell recovery from the 3D models, ATV treatment was repeated three times each 5 min at 37°C with prior EDTA (0.5M) treatment. For surface protein detection, 20,000 – 200,000 cells were transferred into FACS tubes, washed once with FACS buffer and resuspended in 50-100 µL of appropriate dilution of primary antibody and incubated at 4°C for 1h. After a FACS buffer washing step, the fluorescent secondary antibodies were diluted and added in 50-100 µL of FACS buffer and incubated at 4°C for at least 30 min. Cells were then washed and measured by flow cytometry. Detection of total

protein followed the same procedure except for prior fixation in 100 µL 4% PFA for 20 min at 4°C followed by a washing step and dilution of primary and secondary antibodies in saponin buffer.

3.8.1 Cell viability analysis

Cell viability was analyzed using Annexin V or/and propidium iodide (PI) staining. Annexin V binding marks both early apoptotic and necrotic cells, while PI penetrates cells and marks late-stage apoptotic cells and necrotic cells. Living cells will be unstained. For positive control, cells were killed by incubation at 60°C for 15 min.

3.9 Cell lysate preparation and protein quantification

Cells (minimum of 1×10^6) were transferred to centrifuge tubes and washed with cold PBS followed by the addition of 100 µL lysis buffer, vortexed, and incubated for 30 min incubation. Lysates were centrifuged at 10000 rpm for 5 min at 4°C, and the supernatant was cautiously moved to 1.5 mL tubes. The protein concentration in lysates was measured using BCA, and the rest of the samples were stored at -20°C. For protein quantification, 5 µL of samples or protein standard were applied to 995 µL of a solution of CuSO4 diluted 1:50 with BCA solution (1 mL BCA with 20 µL of CuSO4) in 1.5 mL tubes, vortexed, and incubated at 60°C for 15 min. Samples were transferred into cuvettes for the protein absorbance measurements using the photometer.

3.10 Western blot

3.10.1 SDS-PAGE and protein transfer

The western blot method allows the detection of proteins of interest by separating them according to their electrophoretic mobility via Sodium dodecyl sulfate-polyacrylamide gel electrophoresis (SDS-PAGE) in the electrical field. Two gels were used to separate the proteins; the first gel is known as stacking gel with a neutral pH in which loaded proteins are concentrated and a separating gel with pH 8.7. Gels used in this study were 8 or 10 % polyacrylamide, and 30-50 µg of protein from the cell lysates were used. The lysates were mixed were 3X Laemmeli buffer, incubated at 95°C in a heating block for 5 min and loaded onto the gel. The electrophoresis was performed at a constant current of 120 mA (for a 12cm gel) for 3-4 hours or at 8 mA for overnight.

Following electrophoresis, proteins were transferred to a nitrocellulose membrane. Whatman papers, membrane, and gel were soaked in anode and/or cathode buffers and placed onto the transfer apparatus in the following order: Two Whatman papers soaked in cathode buffer, the SDS gel soaked in cathode buffer, the nitrocellulose membrane soaked in 30 mM anode buffer, two Whatman papers soaked in 30 mM anode buffer, and two Whatman papers soaked in 300 mM.

After the transfer at 125 mA for 1-2 h, the nitrocellulose membrane was washed 1 x with PBS/0.1% Tween, blocked 30 min at RT in 5% non-fat dry milk or BSA in PBS/0.1% Tween (depending on the primary antibody) and washed once with PBS/0.1%Tween. The membrane was incubated overnight on a shaker at 4°C with the

primary antibody diluted in 5% non-fat dry milk or BSA in PBS/0,1 % Tween and washed three times 5 min at RT. The secondary antibody diluted in 5% milk/PBS/0.1%Tween was added, incubated for 1h at RT and washed three times with PBS/0.1%Tween followed by the acquisition of the membrane image in a Li-cor OdysseyÒ Fc Imaging system.

3.11 Confocal Microscopy

Imaging was performed by the confocal laser scanning microscope LSM 780, Zeiss, which is equipped with an incubation system and objectives with the following specifications; oil 63x/1.4, oil 40x/1.4, air 40x/0.95, 20x/0.8, 10x/0.45 plan apochromat. Fluorescence dyes were excited by laser lines 488 nm, 555nm, 568nm, and 633 nm. For live-cell imaging experiments, samples were transferred to ibidi microscopy slides and dishes containing normal cell culture medium supplemented with HEPES buffer or other pH controlling buffers. The incubation system was used in all live-cell imaging experiments if not otherwise stated. The acquired images were pre-processed using DAQ software ZEN2012 black or directly used for image analysis by ImageJ or Imaris software.

3.11.1 Live imaging in 3D tissue models

For live-cell imaging, the bigger outer ring was cautiously removed and samples were transferred into a 35 mm ibidi µ-Dish containing normal cell culture medium supplemented with 10mM HEPES buffer.

For imaging DC transmigration, MV-DCs were labeled with live NucBlue stain for 15 min at 37°C prior to addition to the models. 1h after addition of MV-DCs to the basolateral side of the tissue models (3.1.5), samples were transferred to microscopy dishes and static imaging by acquiring Z-stacks from the complete tissue was performed, or time-lapse z-stack using 20x apochromat for 2h was recorded. Image analysis for 3D cell tracking and quantifications was carried out using Imaris software (Bitplane).

3.11.2 Morphological analyses of MV-DCs

2 x 10^5 cells from MV-DC cultures were applied to each channel of fibronectin-precoated ibidi channel slides (µ-Slide VI0.4) (20 µg/mL of fibronectin in PBS for 2 h at 37°C followed by 3 times washing with PBS and air-dry for 10 min under the laminar hood) for 2 h at 37°C and allowed to migrate on the support. After a washing step using pre-warmed PBS, cells were fixed with pre-warmed 4% PFA for 15 min at 37°C, permeabilized with 0.1% Triton X-100 for 5 min at RT and washed 3 times with PBS. The blocking step was performed by 5% BSA/PBS for at least 30 min at RT. Samples were washed once by PBS and incubated with primary and secondary antibodies as described.

For determining cell polarity, circularity analysis was performed using ImageJ based on phalloidin actin detection by manual segmentation. This was required because the phalloidin signal was not always complete along the cell borders, which could result in errors by an automated method. Additionally, cells displaying more than one nucleus, lacking defined cell borders or cells close to the image edges in at least one

fluorescence channel were discarded. The cell borders of chosen cells for the analysis were measured and the circularity parameter was automatically calculated according to the following equation:

$$\text{Circularity} = 4 \cdot \pi \cdot \left(\frac{\text{area}}{\text{perimeter}^2} \right)$$

Obtained values from circularity measurement are between 0 and 1, with 1 representing circular and values towards 0 showing a deformed elliptical shape.

3.12 3D migration analysis in collagen matrix

For MV-DCs random migration analysis in collagen matrices, 1×10^6 cells from MV-DC cultures were resuspended in 10% RPMI and embedded in un-polymerized collagen gels. Cells were imaged under the confocal microscope using laser line 488 and transmission light (DIC) for 90 min. For collagen polymerization, rat-tail type I collagen gel was adjusted to neutral pH with 7% bicarbonate, mixed with 10X minimal essential medium (MEM) and the cell suspension in a standard culture medium. The mixture was prepared in 1.5 mL tubes and on ice to avoid fiber polymerization, then incubated for 2 min at 37°C, loaded into the channel slides and incubated for further 40 min at 37°C for polymerization. The table below shows the used amounts for 2 mg/mL collagen gel preparation.

Table 13 Collagen matrix mix

Component	Volume
Bicarbonate (7%)	4.25 µL

MEM	3.75 µL
Collagen	30 µL
1×10^6 DCs in medium	37.5 µL

After polymerization, live-cell imaging to record cell tracks was performed. In case of using inhibitors, DCs were pretreated with Y27632 (30 µM), SKI-II (10 µM), or VPC23019 (10 µM) 2h prior to life imaging.

In case of using the D-erythro-sphingosine 1-phosphate which is a photolyzable derivative of Sphingosine-1-phosphate (S1P) and is termed as caged S1P, DCs were pre-loaded with the caged S1P molecule (1-2 µM) for 2h prior to life imaging. Due to its caging chemical groups, which makes the S1P inactive, this molecule allows the study of S1P-mediated intracellular events (83). Prior to life cell imaging, the caged-S1P loaded DCs were exposed to UV light (254nm wavelength) irradiation for 30 sec.

Cell tracking analysis was carried out using the Fiji plugin “Manual Tracking” and the quantification of velocity and migration distances was performed using the “Chemotaxis Tool” software.

3.13 3D image analysis

3D images obtained from live imaging of the 3D models described in 3.11.1 were analyzed using the Imaris software. To define the migration efficiency of GFP+ and GFP- DCs in MV-infected DC cultures and to distinguish the fast migratory cells in this

population, the Z positioning of the cells in the collagen scaffold 2 h after DC reconstitution was compared by quantification of the number of DAPI+ cells (GFP+ or GFP-) in this cell population using the Imaris spot detection tool. The signal intensity segmentation was performed using the diameter filter between 10-15 µm for the spot detection algorithm, and the values were chosen to reach the best overlap of detected spots with the actual fluorescence signal. After transforming the intensity point clouds into countable objects, a filter with a quality parameter was also applied to improve the detection. For preprocessing of the raw data, a median filter (3x3x1 px kernel) was used to improve the performance of the spot detection algorithm.

To estimate migration efficiencies, a ratio of counted cell in a top DC layer to the total DC count in the model was calculated. In order to keep the consistency of the analysis for different models, first, the distance between the z position of the lowest and the highest GFP+ DC in the 3D model was defined. Then the respective intermediated z position was calculated, and the top layer was defined above the intermediate point.

Random 3D migration was automatically analyzed by application of an autoregressive motion algorithm. In order to sort and edit the tracks, a filter for track length above 10µm and track duration longer than 2.4 s was set to avoid the nonrecurring events. For the maximum distance between detected spot and predicted position in subsequent time points, we set 13.9 µm and 26.5 µm for GFP+ or GFP-/DAPI+ cells. Dimensions of the representative model are 425, 425, 45 µm (X, Y, Z) with 3.5 min time intervals.

3.14 Virological methods

3.14.1 MV culture and stock preparation

Wild type MV (strain WTF) was cultured on BJAB cells. 5 x 10^7 BJAB cells were resuspended in 5 mL of serum-free RPMI medium in a 15 mL centrifuge tube, WTF (MOI 0.01) was added and incubated at 37°C for 3h with intermittent inversion (4-5 times). Cells were then pelleted (1600 rpm for 5 min), resuspended in 100 mL RPMI supplemented with 10% FCS and were cultured for 2-3 days at 37°C. When syncytia formation was observed, the infected culture was inoculated on BJAB cells in 550 mL culture flask and further cultured for 24h. When syncytia became visible, cells were harvested by centrifugation, resuspended in 1 mL PBS per flask and stored at -80°C. Analogous to virus cultivation, uninfected BJAB cells were grown and harvested which served as a MOCK control.

The recombinant wild type virus IC323eGFP was grown in Vero-hSLAM cells. These were cultured in 175 cm^2 flask until 60-70% confluency before the medium was removed and the virus (MOI 0.01) was added in 5 mL of serum-free RPMI medium. After a 3h incubation at 37°C the virus inoculum was replaced with 20 mL of RPMI supplemented with 10% of FCS, cultures were incubated for 2-3 days at 33°C and cells were harvested by using a cell scraper. The cell suspension was collected in a precooled homogenizer, homogenized 10 -15 times to enable the release of the cell-associated virus and centrifuged at 280×g for 15 minutes at 4°C. The centrifugation

step was repeated three times in order to remove the cell debris. The viral supernatants were aliquoted in cryo-tubes and stored at -80°C.

3.14.2 Virus titration

MV titration was performed on B95a cells in 96-well plates. One day prior to the assay, 5 $\times 10^4$ B95a cells were suspended in 100 µL culture medium and seeded per well. For titration, virus stocks were serially diluted in serum-free RPMI culture medium with a dilution factor of 100 (starting with 1:10) (8 values per dilution), in a way that for the first column of the plate, 100 µL of the virus was mixed with 900 µL serum-free culture medium and the mixture was distributed to the wells of the first column (100 µL per well) followed by the other columns in the serial dilution. After incubation for 3h at 37°C, the viral inocula were replaced with fresh RPMI medium supplemented with 5% FCS and incubated for 3-4 days in 37°C incubator. MV infection-induced syncytia (plaques) were counted microscopically. The titer is indicated as PFU/ml, which is calculated by the following formula: $\frac{Mean\ number\ of\ plaques \times dilution\ factor}{volume\ of\ inoculum\ (mL)}$

3.14.3 MV infection of monocyte-derived DCs

Immature DCs were transferred into 1.5 mL tubes, centrifuged for 2 min at 8000 rpm, and resuspended in serum-free RPMI medium containing MV (MOI 3)(volume ratio of the virus to the medium 1:2). The equivalent amount of culture medium containing MOCK suspension was added to control DCs. Cells exposed to virus or MOCK were incubated for 3 h at 37°C incubator with intermittent vortexing (every 20 min), washed and resuspended in 1 mL (per 1×10^6 cells) of fresh RPMI medium supplemented with

10% FCS, IL –4, GM-CSF and 200 µM of fusion inhibitory peptide (FIP). The efficiency of infection was determined by flow cytometric detection of MV N-protein staining or eGFP expression (for rIC323) after 24 h. For DC maturation, these immature DCs were treated with LPS (100 ng/mL) overnight at 37°C

3.15 Lipid analysis

In order to perform the lipid analysis, 1 x 10^6 DCs per sample in two groups of MV exposed immature DCs (MOI 2) or MOCK exposed (at the equivalent amounts for MV exposure) for 24 h were prepared and thereafter dissolved in 1 mL of ice-cold methanol. For S1P extraction, C17-S1P (Avanti Polar Lipids, Alabaster, USA) was used as an internal standard and quantified as described (84). Samples were analyzed using liquid chromatography tandem-mass spectrometry (LC-MS/MS) using a 6490 triple quadrupole mass spectrometer (Agilent Technologies, Waldbronn, Germany) operating in the positive electrospray ionization mode (ESI+) (77).

3.16 ASM assay

To measure ASM enzyme activity, the fluorescence-labeled sphingomyelin fanalogue HMU was used as a substrate.

5-10×10^5 DCs were pelleted at 8000 rpm for 5 min at RT, resuspended in 40 µL lysis buffer and mixed by vortexing. The suspension was frozen at -80 °C for 5 min and then thawed in 37 °C water bath for 5 min. The freeze/thaw procedure was repeated for 4

times. Lysates were centrifuged at 8000 rpm for 2 min to remove the cell debris, mixed with the substrate, and EDTA (Table 14) and were incubated at 37°C overnight.

Table 14 ASM assay mix

Component	Volume
Cell lysis	10 µL
HMU-PC (pH 5.2)	10 µL
EDTA (30 mM)	1.3 µL

The assay was performed in triplicates. One sample only contained the lysis buffer was used for background measurement. The reaction was stopped by addition of 100 µL stop buffer which contains 0.2M glycine, 0.2M NaOH, and 0.25% TritonX. Samples were transferred to a black flat bottom 96-well-plate, and fluorescence was measured at the excitation of 404nm and emission of 460nm by the Tecan fluorescence reader. For data analysis, the background value was subtracted from sample values.

3.17 Statistical analysis

The statistical evaluation and graph preparation was performed using GraphPad Prism 6. For comparing two groups, a two-tailed student's t-test was performed when having a normal distribution or the Mann-Whitney test when there was no normal distribution. For the statistical analysis the P-values are shown as *P <0.05, **P <0.01, ***P < 0.001, ****P <0.0001 on graphs. Data shown was acquired in at least three independent experiments, each consisting of at least one donor.

4 Results

4.1 MV-DCs migration in the 3D human respiratory tract model and virus transmission to recipient H358 epithelial cells

The developments in infection models using tissue engineering technology to mimic an *in vivo*-like situation have gained great importance in recent years (85). To study and understand fundamental parameters in MV transmission in the upper respiratory tract, the previously published 3D respiratory tract model (86) needed to be advanced by addition of dendritic cells supposed as donors for viral delivery to epithelial cells and subsequent exit of the virus via the respiratory tract. This 3D in vitro human respiratory test model mimics the late phase of infection as closely as possible to the *in vivo* situation.

4.1.1 Generation of 3D respiratory tract model

The 3D model was generated as detailed in methods. The schematic representation in Figure 8 shows the procedure of MV-DCs addition to the model.

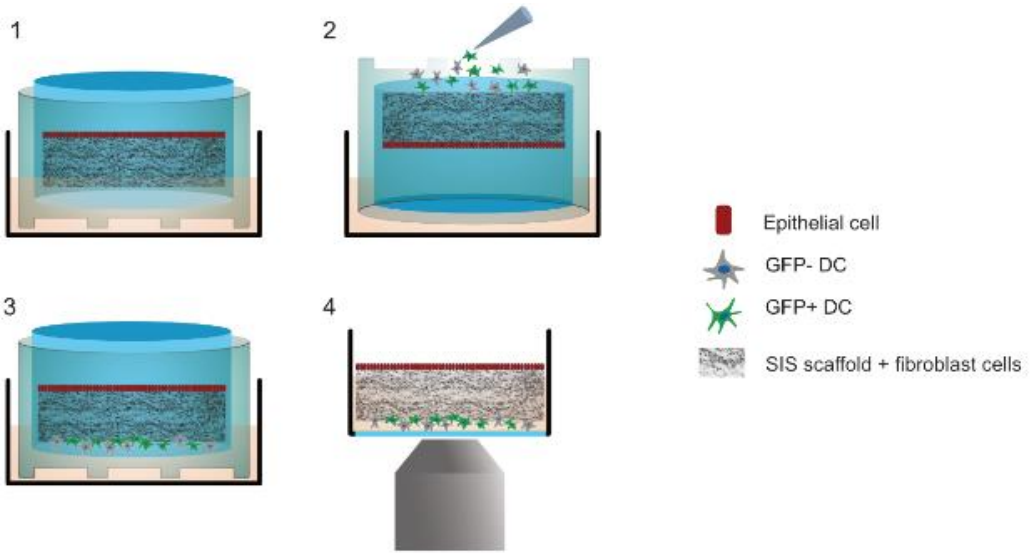

Figure 8 Schematic representation of the 3D model set up
1) 3D model general structure, 2) flipping the model up-side-down to add MV-DCs to the basolateral side, 3) reverting the model back to the original orientation after 1h. Subsequently, the model was incubated at 37°C and used for fixation or for life imaging experiments, 4. (77).

4.1.2 Evaluating the suitable culture time of 3D models

In order to evaluate the most suitable time frame for 3D model culture and monitor the impact of culture time on epithelial cell barrier integrity, FITC-dextran assays were performed. The FITC-dextran permeability of the models containing human airway basal (BCi-NC1) cells and human lung epithelial adenocarcinoma (H358) cells was measured at days 7 and 10 of culture and compared to that of a control model containing only SIS scaffold (negative control) (Figure 9).

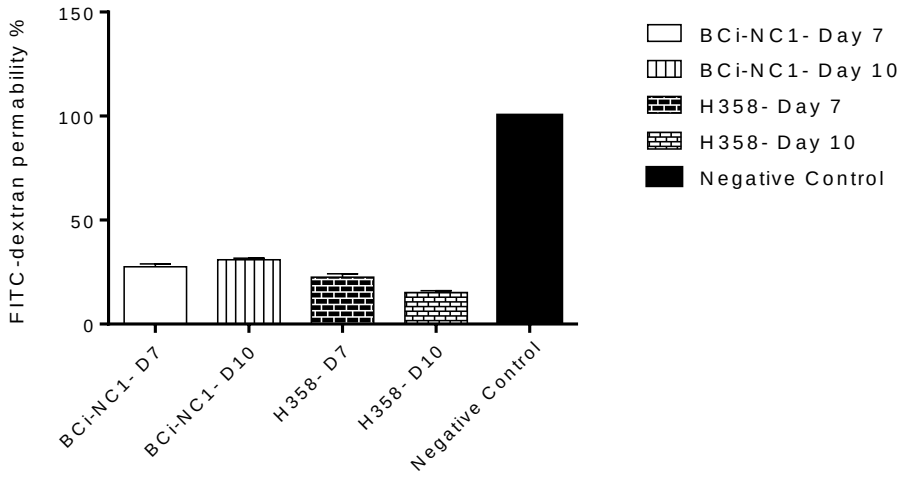

Figure 9 FITC- dextran assay in different culture durations.
The FITC-dextran permeability of the 3D models containing BCi-NC1 or H358 cells on SIS at different time points was compared with a negative ctrl model containing only SIS. Values are normalized to the negative ctrl set to 100% (n=3).

The permeability of BCi-NC1 models increased (~ 3%) between day 7 and 10 while that of the H358 models was reduced (~ 5%) within this time frame. Therefore, a 10 days culture with H358 cells (which are more suitable for MV infection studies) was used in further experiments.

The barrier integrity was one of the important factors to validate the 3D models stability and to ensure the reliability of further experiments. Therefore, measurement of TEER-value with the chopstick electrodes as an easy additional and non-invasive way to determine the barrier function of the H358 models was employed and compared to that seen in FITC- dextran assays (Figure 10).

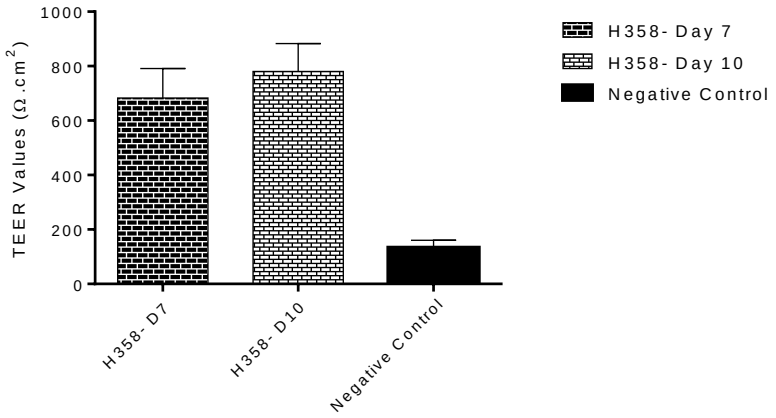

Figure 10 Transepithelial electrical resistance (TEER) measurement.
Barrier integrity of models containing H358 cells was analyzed using TEER measurements after 7 and 10 days of culture. The values are compared to a negative ctrl model containing only SIS (n=3).

4.1.3 Cellular characterization of the 3D model

Based on the optimization experiments described above, H358 human lung adenocarcinoma epithelial cells were seeded onto the decellularized SIS scaffold containing primary fibroblast cells for 10 days under static culture conditions (details described in 3.1.5).

To illustrate the morphology of the whole model structure, hematoxylin and eosin (H&E) staining was performed. The H&E staining showed a confluent cell layer on the apical surface of the tissue model and some cells having migrated into the SIS scaffold (Figure 11A). To identify the cellular compartments, immunofluorescent staining was performed. This verified earlier data (86) revealing E-cadherin-positive H358 within the apical epithelial layer and vimentin-positive fibroblasts migrated in the connective tissue (Figure 11B).

A

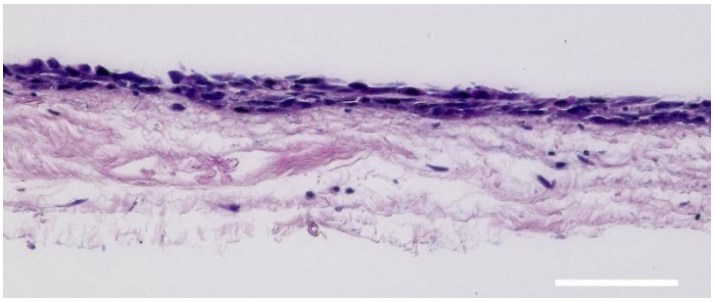

B

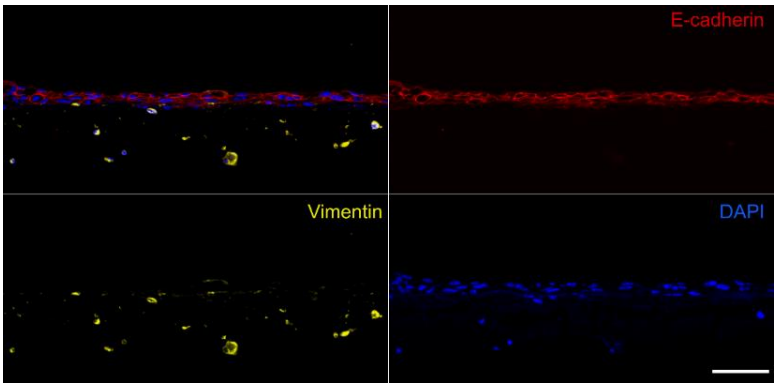

Figure 11 Cellular compartments within the 3D respiratory model.
Hematoxylin/eosin (A) and immunofluorescent (IF) staining (B) for E-cadherin (apical epithelial cell layer, red), vimentin (collagen-embedded primary fibroblasts, yellow) and nuclei (DAPI, blue) of the 3D model tissue. Scale bars, 100 µm. (77).

4.1.4 MV infection of immature dendritic cells

Immature monocyte-derived DCs were infected with MV-IC323-GFP for 24h. As described earlier (40, 87, 88), MV-infection caused phenotypic maturation of DCs as determined by detection of surface markers prior to and after infection by flow cytometry (Figure 12).

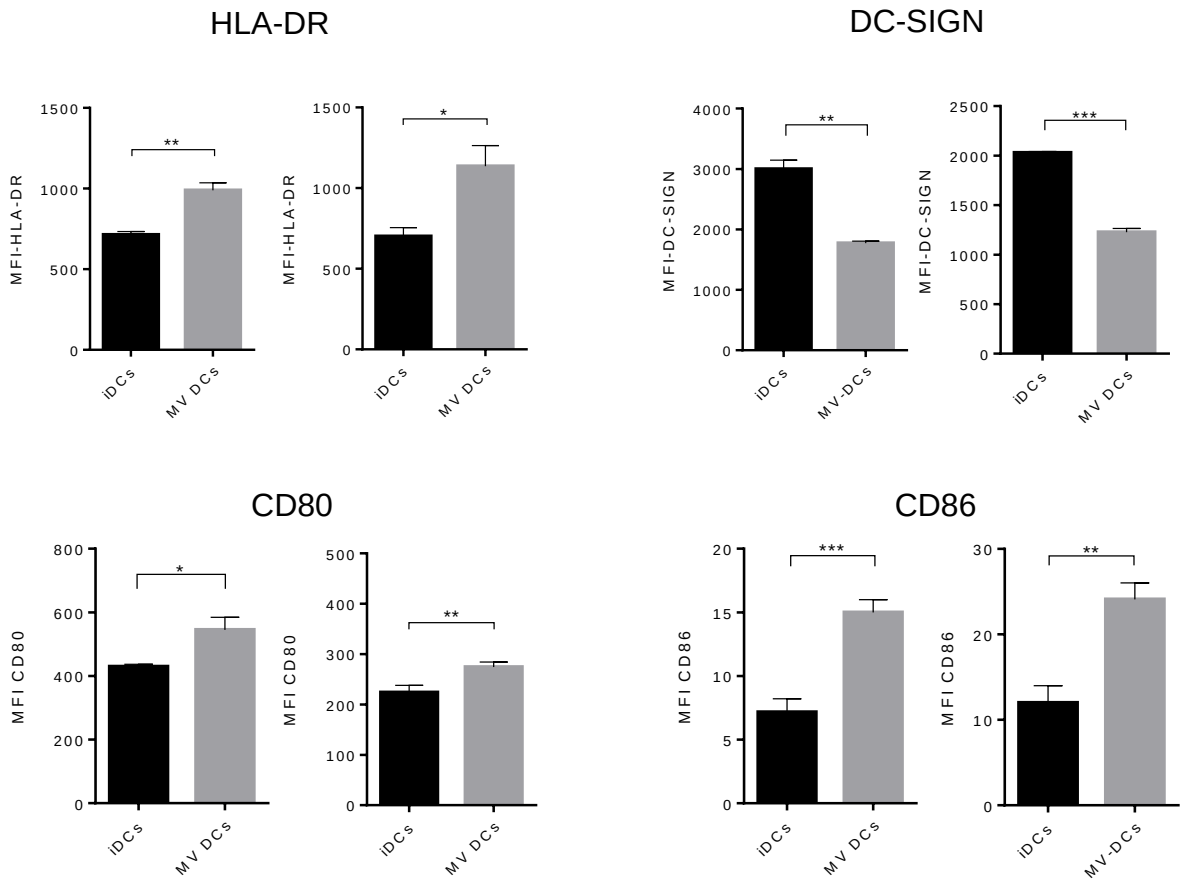

Figure 12 Phenotypic characterization of DCs before and after MV infection.
FACS staining for HLA-DR (upper left graphs), DC-SIGN (upper right graphs), CD80 (lower left graphs) and CD86 (lower right graphs) in MFI values. Each graph shows one independent donor in three replicates.

As typically seen in matured DCs, MV caused upregulation of MHC class II, CD80 and CD86 while DC-SIGN was downregulated. To reveal whether phenotypic maturation was confined to infected cells, DC maturation status of the entire culture exposed to MV as well as double detection of MV (assessed by GFP detection) and representative maturation markers (CD86 and HLA-DR) was performed by flow cytometry (Figure 13 A and B). In agreement with earlier findings, MV exposure caused phenotypic maturation of the entire culture (14, 89, 90) independently of actual infection levels

which substantially varied donor-dependently (ranging from 10-60% as identified by GFP expression) (Figure 13B).

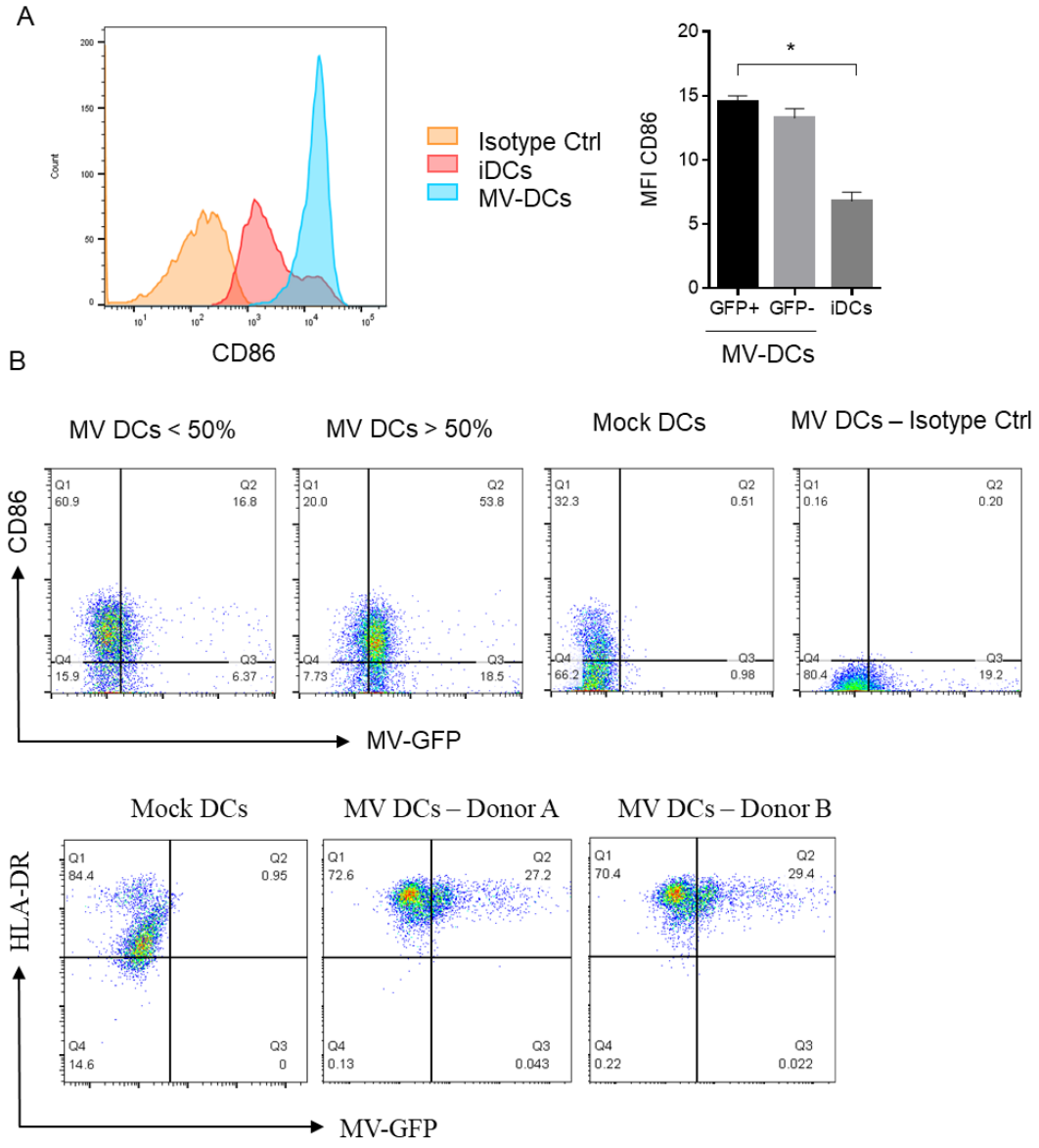

Figure 13 Maturation status of DCs after MV infection.

A) Histogram representation of CD86 (left panel) with the corresponding CD86+/MV-GFP MFI in DC populations compared to the isotype control. Results are expressed as mean ± SEM of 3

independent experiments. B) Double detection of MV and maturation markers, CD86 (top panel) and HLA-DR (bottom panel).

4.1.5 Addition of DCs to the 3D respiratory tract model

For the addition of DC, the tissue models were horizontally flipped and DCs (when infected cultures were used these contained a mixture of infected (GFP+) and uninfected (GFP-) cells) were added to the basolateral side of the model as shown in (Figure 8). The models were incubated for 60 min in this position and then re-flipped to the original orientation. According to the IF staining images taken 24h after addition of DCs, these had migrated through the tissue model (from the basolateral side to the top where the epithelial cells layer is located) as detected by the presence of DC-SIGN+ cells in close proximity to and within the E-cadherin-positive epithelial layer (Figure 14).

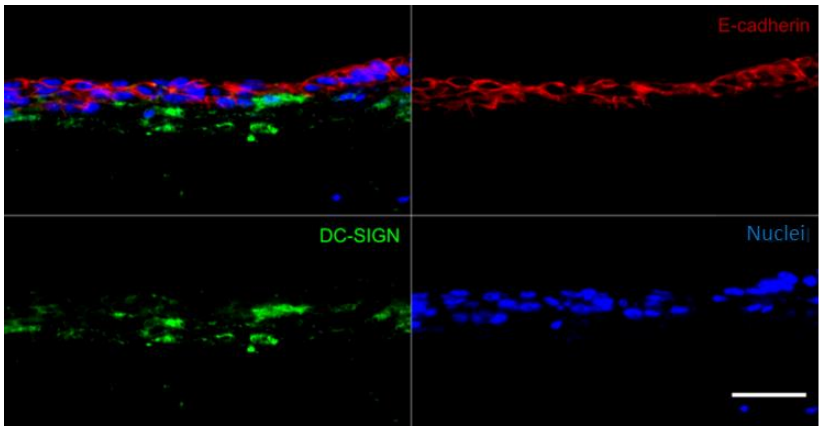

Figure 14 Dendritic cells localization inside the 3D model.
DC-SIGN+ cells (green) in close proximity to and within the epithelial layer (E-cadherin, red) 24 h after basolateral addition of DCs. Scale bar, 100 µm. Overlay in the upper left panel. (77).

4.1.6 Addition of MV-DCs to the model and MV transmission to the recipient H358 epithelial cells

To monitor if MV-infected DCs would be able to traverse the collagen scaffold and to transmit the infection to epithelial cells, MV-DCs (containing both GFP+ and GFP- DCs) were reconstituted into the model in which epithelial cells were labeled with a cell proliferation dye eFluor670 prior to addition to the 3D model. As seen 72h following DC-transfer by direct life fluorescent imaging EGFP signals were detected within the epithelial cell layer indicating that DCs had reached this compartment and delivered virus there to H358 cells (Figure 15).

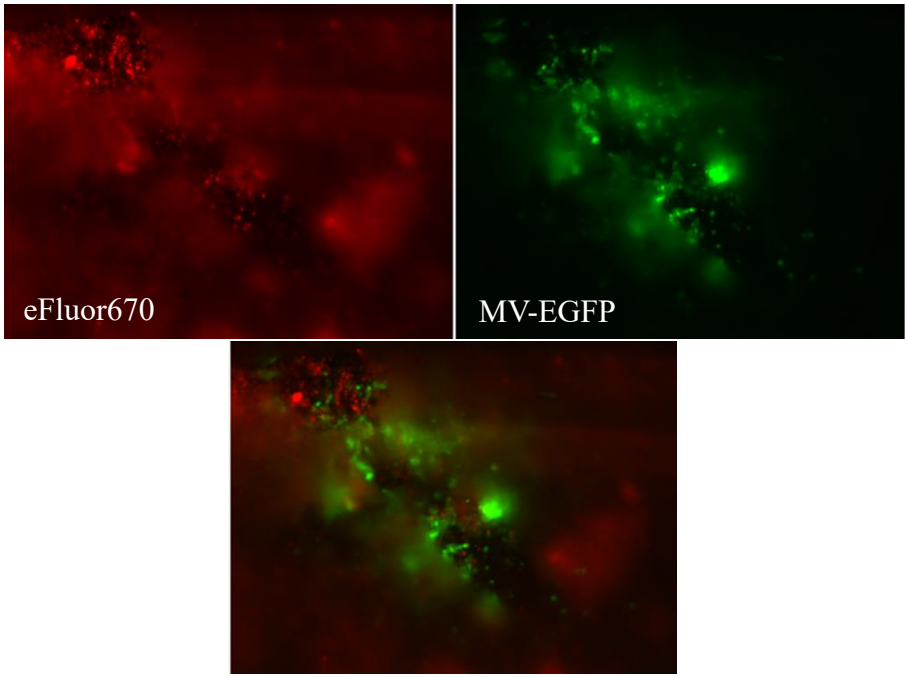

Figure 15 Fluorescent images of MV-infected H358 epithelial cells in 3D models.
Fluorescent images of pre-labeled H358 cells with eFluor670 dye in red (top left) and MV-EGFP in green (top right) and the overlay (bottom row). Images were taken 72 hours after MV-DC addition to the models.

This MV transmission from MV-DCs to epithelial cells was also confirmed by flow cytometry. Four days after addition of MV-DCs, epithelial cells were recovered from the 3D models and the infection rate in H358 epithelial cells was measured by double detection of GFP and the eFluor670 in pre-labeled epithelial cells which was not seen when, for control, uninfected DCs (though immature) had been added instead of MV-DCs (Figure 16).

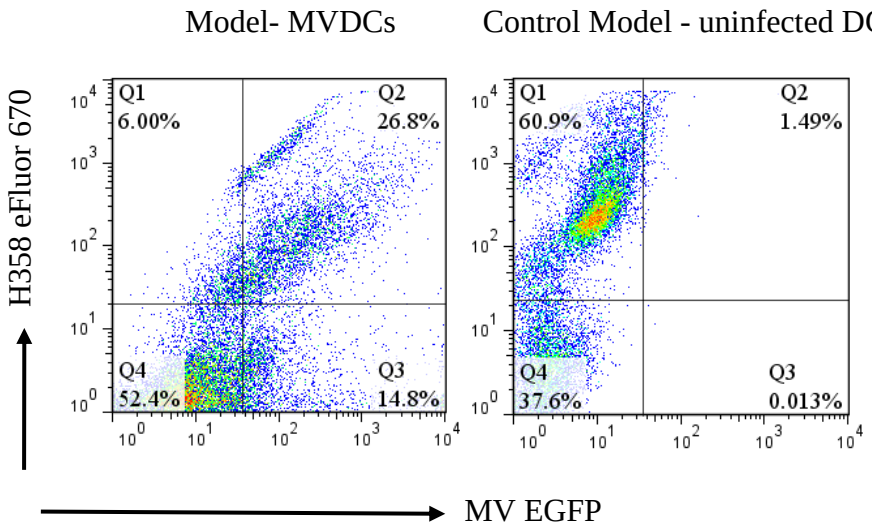

Figure 16 Detection of MV-infected H358 epithelial cells in 3D models after trypsin-EDTA recovery.

Double detection of GFP and H358 eFluor670 labeled cells in a model consisting of MV-DCs (left) and a control model negative for GFP signal consisting of uninfected immature DCs (right).

4.2 Generation of a CRISPR-Cas9 edited H358 cell line

MV entry into epithelial cells relies on Nectin-4 expressed on the basolateral side of their membranes which is oriented towards the collagen scaffold in 3D models. If transmission by donor cells to H358 recipients is specific, ablation of Nectin-4 should ablate this process. Therefore, a CRISPR-Cas9 edited H358 cell line was generated and chosen as a suitable control of MV transmission in the 3D system.

H358 cell lines stably expressing cas9 were generated as described in 3.6. Subsequently, expression of the cas9 mRNA was estimated by semi-quantitative PCR (not shown), and the protein expression was confirmed by western blot (Figure 17).

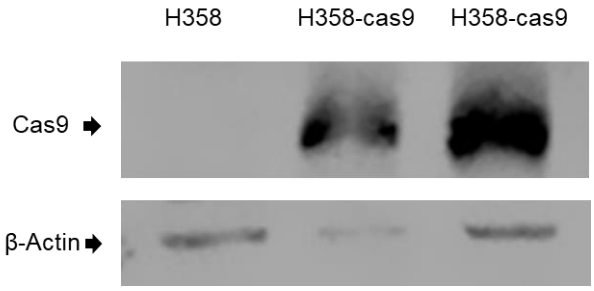

Figure 17 Western blot showing the cas9 protein expression in CRISPR-Cas9 edited cells.
H358 cells were retrovirally transduced with cas9 as described (methods), and Cas9 was detected in wild type H358 (left column) and H358 cas9 transduced cells (middle and right columns with different protein concentrations). Detection of actin as a loading control.

Thereafter, retroviral particles transferring Nectin-4 sgRNA (lentiviral sgRNA, GSGH11838-246559205, Dharmacon, Cambridge, UK) which were produced in HEK293 cells were introduced into stably Cas9 expressing H358 cell line as described earlier. Nectin-4 expression was measured after selection of puromycin-resistant cells containing integrated sgRNA by flow cytometry (Figure 18).

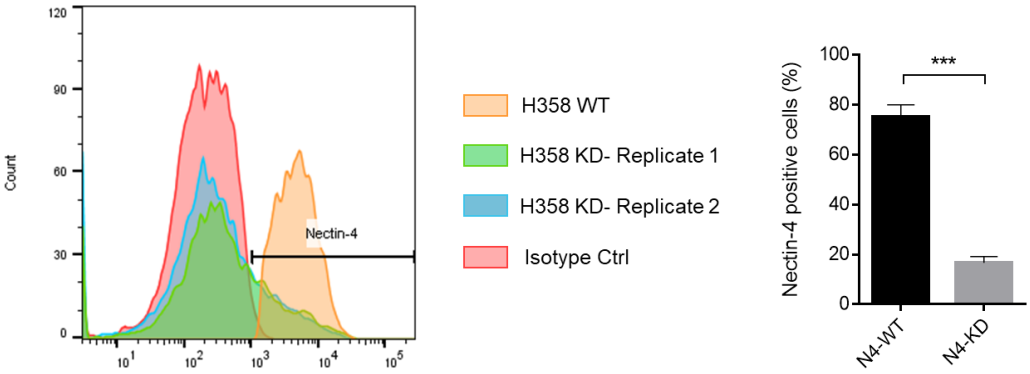

Figure 18 Detection of Nectin-4 in H358 cell line by flow cytometry.
Nectin-4 expression was measured in H358 wild type (WT) and CRISPR-Cas9 edited (KD) cell lines. The histogram shows a representative Nectin-4 expression in two replicates of CRISPR-Cas9 edited cells compared to the wild type. The bar graph shows the mean ± SD of the percentage of Nectin-4 expressing cells in both groups in three independent experiments.

Nectin-4 expression proved to be highly reduced in the edited cell line, which was thereafter used for MV infection in 3D models (Figure 19). Corroborating its role of entry receptor for MV in epithelial cells, ablation of Nectin-4 significantly reduced the amount of GFP+ H358 cells as compared to non-edited controls.

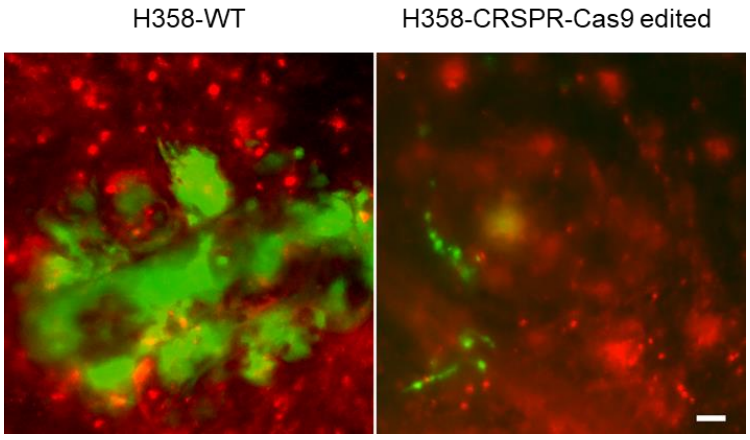

Figure 19 Nectin-4 edited cell line is significantly less permissive to MV infection in 3D models.
Fluorescent images of pre-labeled H358 cells with eFluor670 dye in red and MV-EGFP in green. Images were taken 72h post MV-DC addition to the 3D models. Syncytia formation and higher

amount of MV-GFP signal in H358 wild type cells (left) comparing to the Nectin-4 edited H358 cell line (right). Scale bar: 50 µm.

When used as recipients in the 3D model for quantitative analysis, Nectin-4 edited H358 cells failed to acquire GFP fluorescence from reconstituted MV-DCs in contrast to unmodified H358 cells (Figure 20). Altogether, these findings reveal that our DC reconstituted model system recapitulates MV transmission to airway epithelial cells in a Nectin-4-dependent manner and therefore, is excellently suited to dissect important parameters in this process such as dynamic recruitment of donor DCs.

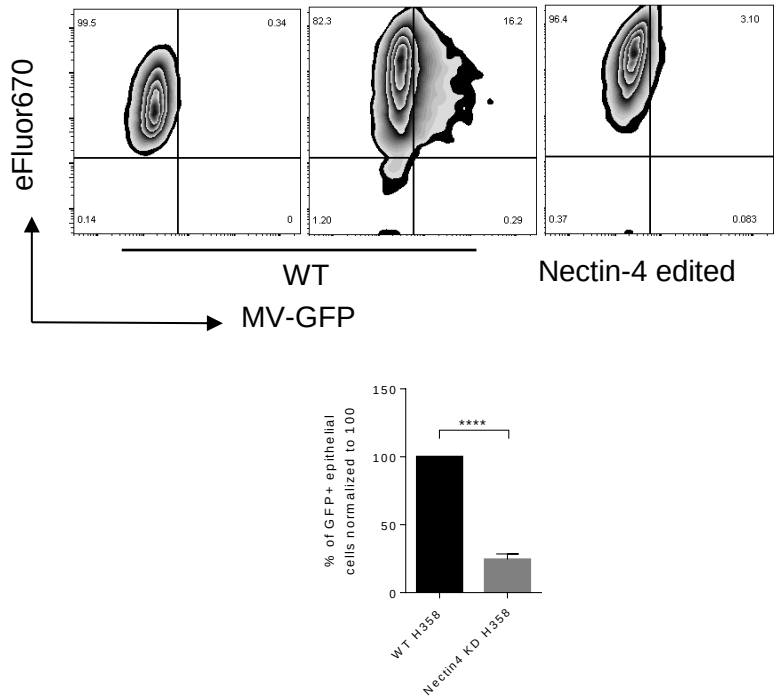

Figure 20 MV transmission from MV-infected DCs to Nectin-4 knockout H358 cells is diminished in 3D models.

MV transmission from MV-infected DCs to wild-type (middle graph) and nectin-4 knockout H358 cells (right graph) was determined 4 days post addition of MV-DCs by flow cytometry. Uninfected wild type H358 cells were used as a negative control (left graph). H358 cells were labeled with eFluor 670 dye prior to addition to the model. The bar graph shows the mean ± SEM of MV

infected epithelial cells (GFP+) percentage in three independent experiments, each consisting of three replicates. (77).

4.3 MV-DC migration in 3D respiratory tract model

The encounter between donor and recipient cell is most important in cell-associated viral transmission. In case this encounter involves motile cells such as immune cells, these should retain the ability to migrate towards the target cells in a 3D environment as an indispensable prerequisite for successful transmission. So far, the lack of suitable 3D systems to study this key aspect has precluded studies on the efficiency of MV transmission during viral exit in the respiratory tract.

4.3.1 MV-infection promotes DC migration in a 3D environment

Considering the importance of migration in transmission, experiments addressing the migration of MV-DCs inside the SIS scaffold in 3D models were performed. In order to evaluate potential differences between added infected and uninfected DCs as both contained in the MV-DC population, migration of GFP+ and GFP- DCs was comparatively analyzed. For detection of MV-DCs (GFP+ and GFP-), these were labeled with DAPI life stain prior to addition to the models. Figure 21 exemplifies the localization of DAPI life stain labeled GFP+ and GFP- DCs in the 3D model containing eFluor 670 pre-labeled H358 cells within 2h after reconstitution.

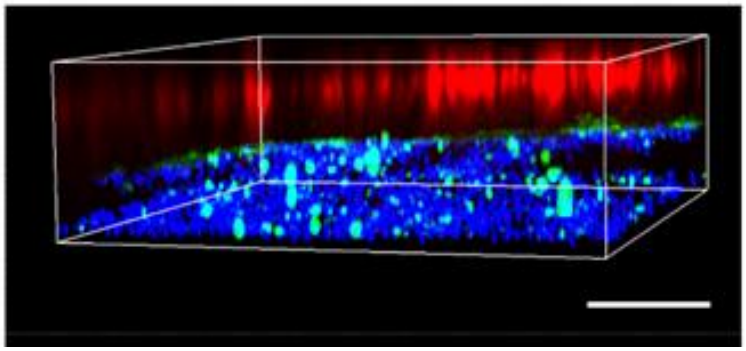

Figure 21 Localization of MV-DCs 2h after addition to the 3D model.
3D view of z-stack reconstruction (raw fluorescence data) of a representative tissue model consisting of eFluor 670 pre-labeled H358 cells (red), fibroblasts (not visible in this plane) and MV-infected DC cultures (pre-labeled with life-DAPI, infected DCs expressing GFP shown in green) 2 h following basolateral DC reconstitution. Scale bar: 200 µm. Data representative of 8 independent experiments. (77).

As visible in Figure 21, DAPI+ MV-DCs had entered the tissue where they were detected at different locations (X, Y, Z) with especially progression within the Z dimension showing the migration towards epithelial cells. The efficiency of this migration can be estimated by comparing the Z values from these z-stacks.

In order to compare the migratory behavior of GFP+ with GFP- DCs, Imaris-based analysis of object segmented 3D z-stacks was performed. This segmentation allowed the transformation of intensity point clouds into countable objects. As described in 3.13, DC migration efficiencies within this time frame could be evaluated by quantification of DAPI-labeled DCs having covered a distance of more than 92 µm toward the H358 layer (Figure 22).

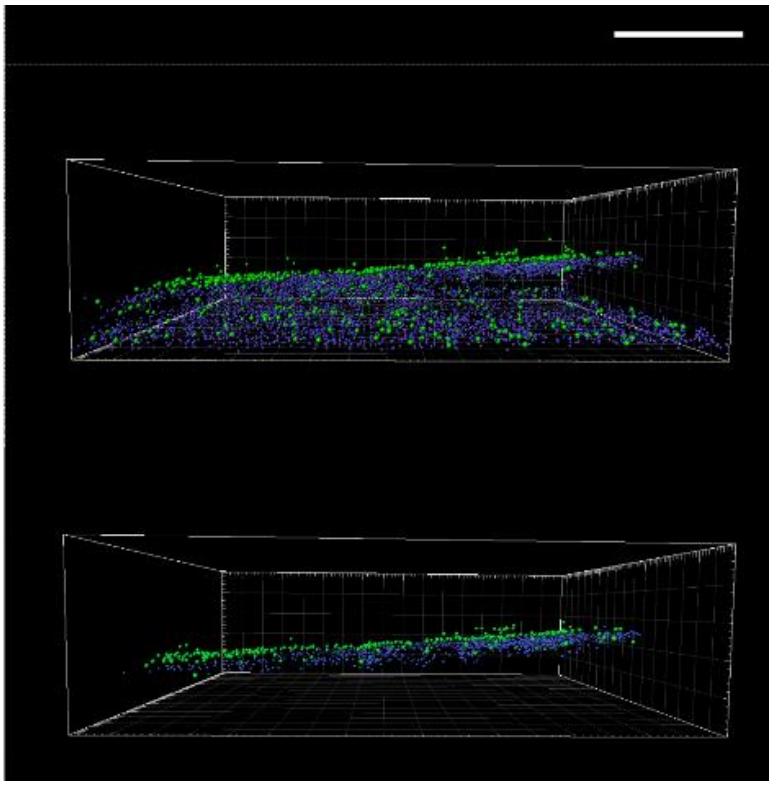

	Total cell count	Top layer cell count	Ratio top layer/total [%]
GFP+ DCs	814	350	43
GFP- DCs	5333	1169	22

Figure 22 Imaris based image analysis allowed cell quantification in z-dimension.
3D view of the model in Figure 21 after conversion into countable objects via spot finder tool in Imaris (top panel) and the estimated top layer (bottom panel) as described in methods. Double counting of cells was avoided by correcting the number of GFP+ cells for the corresponding nuclei count (GFP-). The ratios of the objects in the top layer to the total object count in each group (GFP+/-) was calculated accordingly (table). Scale bar: 200 µm. Data represent 1 out of 8 independent experiments. (77).

Quantifications (Figure 22, table) showed that migration of GFP+ DCs significantly exceeded that of GFP- DCs (43% versus 22% of total DCs detected within the top layer). Because infection rates in this experiment were low, the number of cell counts for the GFP- population by far exceeded that of GFP+ DCs (Figure 22, table). Though

donor-dependent variations in infection levels and overall migration efficiencies were obvious in the 8 independent experiments summarized in Figure 23, these confirmed the higher motility of infected versus uninfected MV-DCs in a 3D environment. (Figure 23 23).

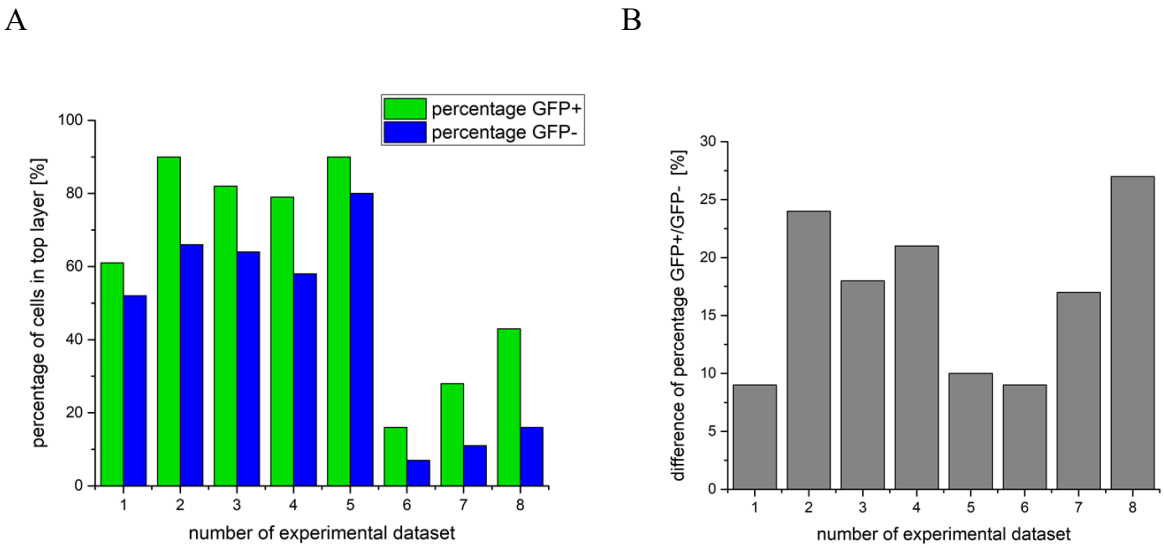

Figure 23 Quantification of cell ratios in the 3D model top layer to determine fast migrating cells.
A) The ratio of cell numbers in the top layer to total cell number for GFP+ and GFP- DCs in percentage. The top layer is set to z-values above half the distance of given highest and lowest detected GFP+ DC. B) The difference of ratios in GFP+ to GFP- DC from the analysis shown in (A) with a mean ± SD of (16.9 ± 7.0) %. Each bar represents one acquired dataset, in total 8 independent experiments.

In order to confirm and support these results, a 3D time-lapse recording of both cell populations in the respiratory model was performed (Figure 24).

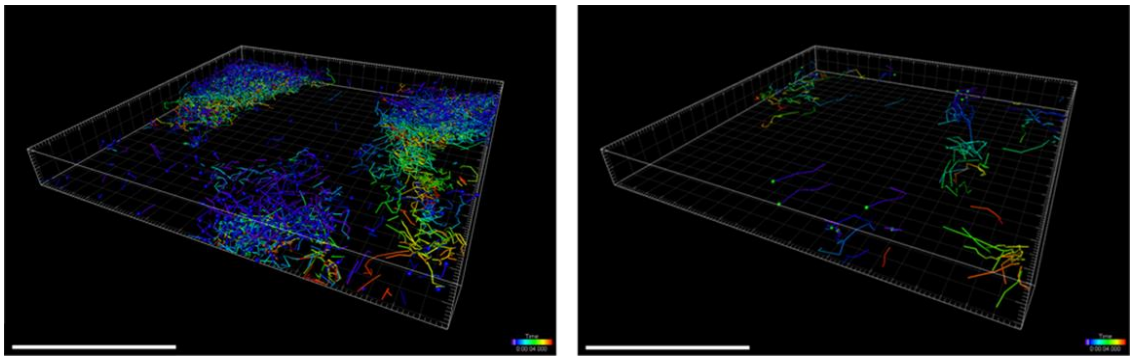

	mean [µm/min]	min [µm/min]	max [µm/min]
GFP- DCs	5.9 ± 2.4	1.0	14.6
GFP+ DCs	8.7 ± 4.6	7.6	21.8

	mean [µm]	min [µm]	max [µm]
GFP- DCs	51.4 ± 42.0	10.0	304.7
GFP+ DCs	86.5 ± 58.9	2.7	289.9

Figure 24 3D single-cell trajectories of MV-DCs migration in 3D models.
3D time-lapse tracks of GFP- (top left panel, n=1722) and GFP+ DCs (n=76) (top right panel) through the 3D model with track lengths being time color-coded. Scale bars: 200 µm. Velocity and track length were quantified (bottom left and right tables, respectively). The data shown is representative of at least three independent experiments.

Track lengths and speed values extracted from the 3D cell tracking data from time-lapse recording revealed around twofold higher values for GFP+ DCs than for their GFP- counterparts during 2 hrs. (Figure 24, table) thereby supporting the 3D z-stack imaging data (Figure 23).

Taken together, this strongly suggests that DC infection (rather than maturation which was common to both GFP+ and GFP- populations) enhanced DC motility in a 3D environment.

4.4 Cytoskeletal activation in DCs is induced by MV infection

According to the data from 3D models, GFP+ and GFP- DCs appeared to have different migrational capacities, and this might reflect differential migration modes. Cell migration is mostly driven by changes in cell morphology (morphodynamics) (91), which are mostly based on the actin cytoskeletal polarization. However, the extent of this polarization differs for different cell types and migration modes. For instance, the mesenchymal migration mode can occur independently of strong polarization (44).

4.4.1 Morphological analysis of MV-DCs on fibronectin-coated channel slides

In order to determine the migration modes for GFP+ and GFP- DCs, a set of morphological analysis was performed after seeding of MV-DCs on fibronectin-coated channel slides.

4.4.1.1 Cytoskeletal polarization in MV-DCs

Cytoskeletal remodeling is prerequisite to cell migration, which, when enhanced, is associated with actin front-rear polarization (44). Therefore a morphological analysis for defining the overall cell polarity in MV-DCs migrating in two different conditions (on fibronectin-coated channel slides or inside the collagen gel) was performed.

Cytoskeletal polarization was quantitatively analyzed by assessment of cell circularity for MV-DCs seeded onto fibronectin (FN) coated slides. The cell circularity index ranges between ‘0’ and ‘1’ with ‘1’ representing a circular and ‘0’ an elliptical shape. Values of <0.5 were, therefore defined polarized cells (Figure 25).

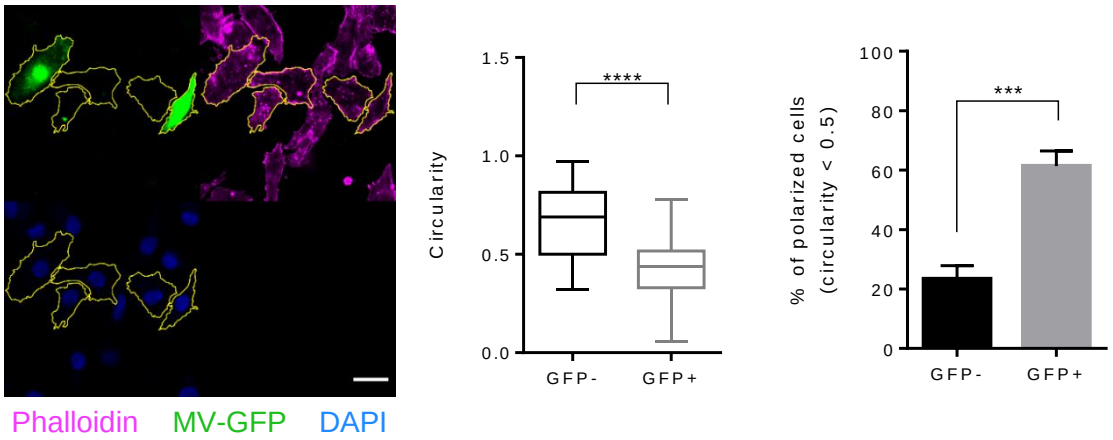

Figure 25 Morphological analysis of GFP+ and GFP- DCs seeded onto FN coated channel slides.

Cells were seeded on FN coated channel slides and incubated for 2 hrs. The manual segmentation strategy for polarity analysis is indicated in the left image (f-actin (phalloidin, magenta), MV-GFP (green), nucleus (blue), scale bar: 20µm). Circularity indices of at least 60 cells in each group (left graph) and percentage of polarized cells, showing a circularity index < 0.5 in each group (right graph) are shown. Circularity index analysis was carried out using ImageJ. Results are shown as mean values ± SEM of four independent experiments. (77).

GFP- DCs showed significantly higher circularity indices than GFP+ DCs (Figure 25) indicating the lower extent of polarization for GFP- DCs and a higher extent of polarization for GFP+ DCs. Moreover, more than 60% of GFP+ DCs revealed circularity indices below 0.5 (highly polarized) while this applied to only around 23% of GFP- cells (Figure 25, graphs). This suggests that MV infection indeed enforced cytoskeletal activation in DCs as required for fast migration.

4.4.1.2 Uropod detection in MV-DCs

Observing a clear difference in actin cytoskeleton polarization between GFP+ and GFP- suggested that the migration mode used by these cells could be different.

In order to support the previous results on differential cytoskeletal polarization, uropod detection based on morphology and presence of actin-enriched structures at the cell rear was performed (92). Thereby, clear segregation of actin-enriched uropods as detected by phalloidin staining was preferentially observed for FN-seeded GFP+ rather than GFP- cells (Figure 26). F-actin accumulation at the rear of GFP+ DCs was directly confirmed by intensity heat map analysis of the immunofluorescence images.

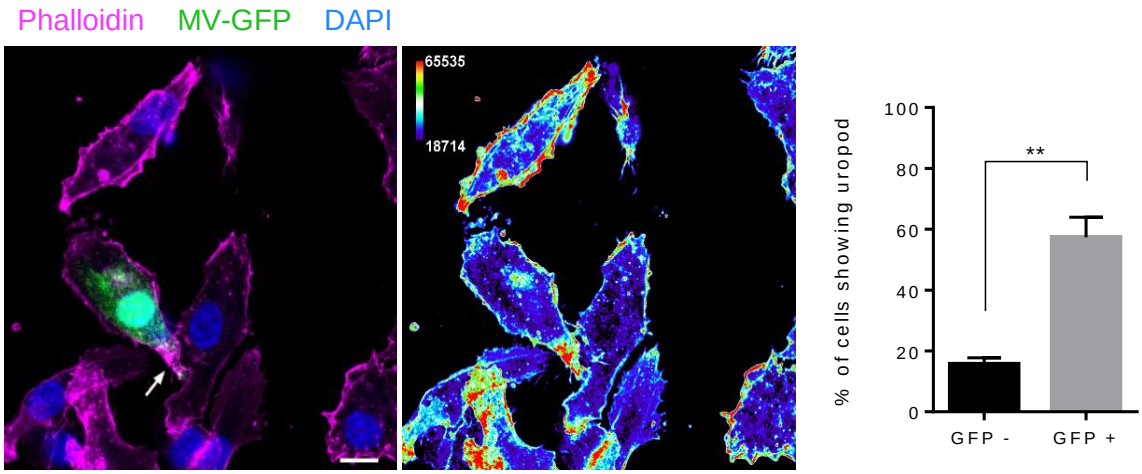

Figure 26 Uropod detection in MV-DCs.
Representative image (left) of uropod detection in DCs, f-actin (phalloidin, magenta), MV-GFP (green), and nuclei (blue). The arrow marks f-actin accumulation at the cell rear (uropod structure) (left). Heat map of f-actin intensity from the same image (right). The thermal LUT look-up-table (ImageJ) has been adapted using the Color/Edit LUT tool. Scale bar: 10µm. The graph shows the mean percentage ± SEM of DCs with a well-defined uropod in each group. Data were acquired in four independent experiments. (77).

4.4.2 Morphological characterization of collagen gel embedded MV-DCs

4.4.2.1 Influence of 3D environment on the migratory phenotype

To reveal whether differential morphodynamics, seen for GFP+ and GFP- MV-DCs on FN supports would also apply in a 3D environment, the phenotype of MV-DCs

embedded in collagen matrices was evaluated. There, GFP+ cells preferentially acquired an elongated shape marked by the strong actin polymerization. Though this morphed during movement through the collagen matrix, the migratory phenotype needed for fast migration was retained in confined environments (Figure 27).

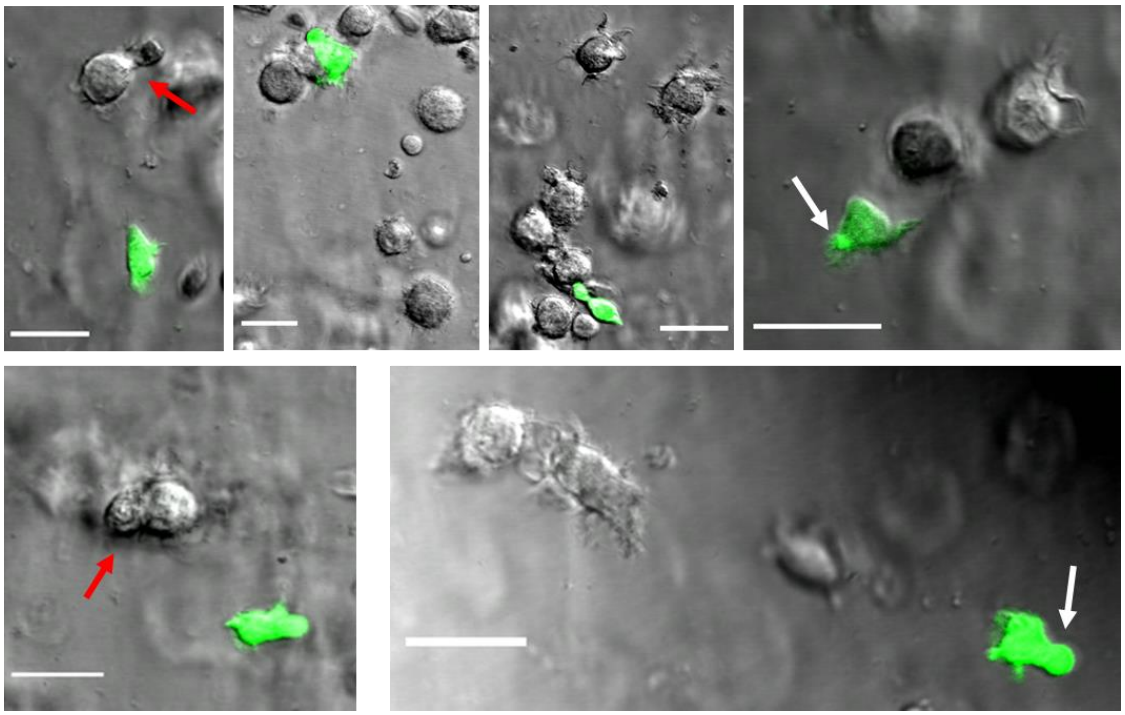

Figure 27 Different migratory phenotypes of GFP+ and GFP- MV-DCs in the 3D collagen matrix.
Overlay of fluorescence and DIC images of MV-DCs (GFP+ (green), GFP-) when migrating through the collagen matrix. GFP+ DCs had an elongated shape when moving through the collagen using the actomyosin contraction at the cell rear, shown by white arrows. GFP- cells retained their circular shape, red arrows point to the supporting contractile force at the cell rear of some GFP- DCs. Scale bars: 20µm.

In contrast, GFP- DCs kept their mainly circular morphology even when moving through the collagen matrix. In common to the majority of GFP+ DCs, a supporting contractile force at the cell rear (actomyosin contraction) was also discernable in a small fraction of GFP- DCs (Figure 27).

These observations suggest that GFP+ and GFP- MV-DCs differ in their migration modes as revealed by the different migration capacities (speed and distance) and differential cell morphology in different substrates. Amoeboid and mesenchymal migration modes are among the most studied migration modes. Suggesting that GFP- DCs preferentially use a mesenchymal-like migration mode, these were less polarized, yet revealed pronounced filopodial structures at the leading edge when migrating in collagen matrices as typical for this particular type of migration (Figure 28). These filopodial structures - not seen in GFP+ cells – additionally were highly active in GFP- DCs as recorded by time-lapse images of DCs migrating in collagen gel I (Figure 29).

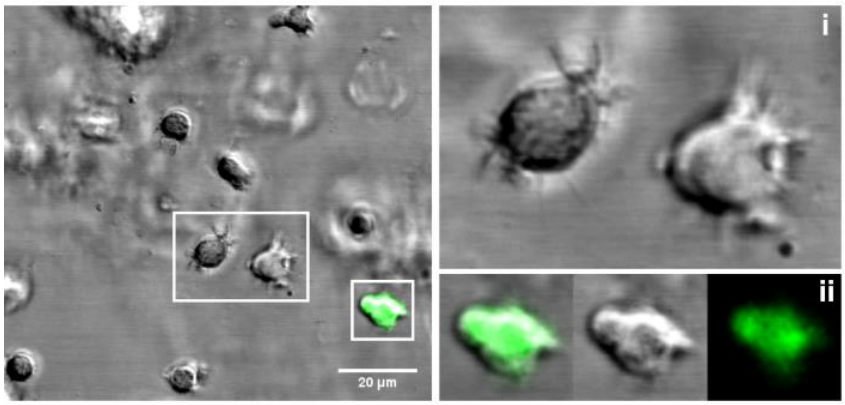

Figure 28 Filopodial structures are most visible in GFP- DCs.
Representative image of MV-DCs filopodial structures while migrating in 3D collagen (2 mg/ml) (left). Insets show magnification of GFP- DCs with several filopodia (i) and GFP+ DC with a well-defined leading edge fewer filopodia (ii), scale bar: 20µm. (77).

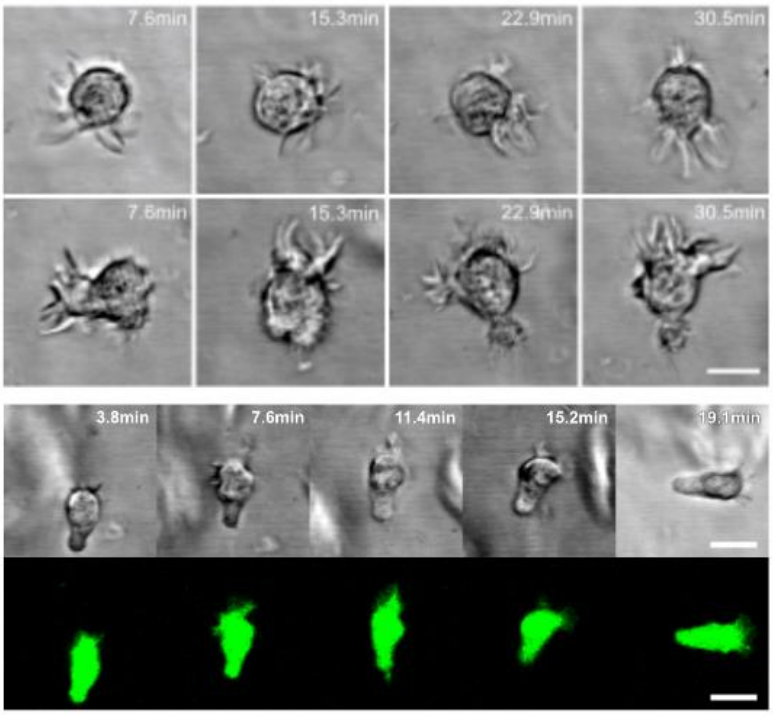

Figure 29 Higher filopodial activity in GFP- DCs.
Time-lapse sequence of two different GFP- (top) DCs and a GFP+ (bottom) DC random migration in 3D collagen (2 mg/mL). Time in minutes (white). Scale bars: 10µm. (77).

4.5 MV infection induces acquisition of differential migratory phenotype by DCs

As shown above, MV infection can modulate the DC migration mode. As evident from the data in 3D model tissue (Figures 22, 23 and 24) and differential morphology of GFP+ and GFP- MV-DCs, it appeared highly likely that GFP+ DCs gained an amoeboid fast migration mode while that of GFP- DCs resembled a mesenchymal-like migration mode.

4.5.1 Enhanced Migration in GFP+ MV-DCs is independent of paracrine signals produced by other cell types

Fast movement through the 3D environment was described earlier for fast leukocyte migration in complex environments (51, 93). However, it is unknown whether and to what extent viral infection can influence the migration of these cells. In order to study virus-induced enforced migration at a mechanistic level, we included collagen matrices for further experiments where the MV-DCs move randomly in the absence of any other cell type.

Using this experimental set-up, features of enhanced GFP+ DC migration seen previously in 3D model tissues were observed. In this random migration system, mean velocity and accumulated distance were enhanced for GFP+ DCs, while their directionality was inferior to that of GFP- DCs (measured and shown as Euclidean distance) (Figure 30). The latter was reflected by the seemingly longer trajectories measured for GFP- DCs documenting a higher degree of directional migration. In contrast, trajectories of GFP+ DCs were marked by a high frequency of turns in the presence of high velocity (Figure 30, right upper panel).

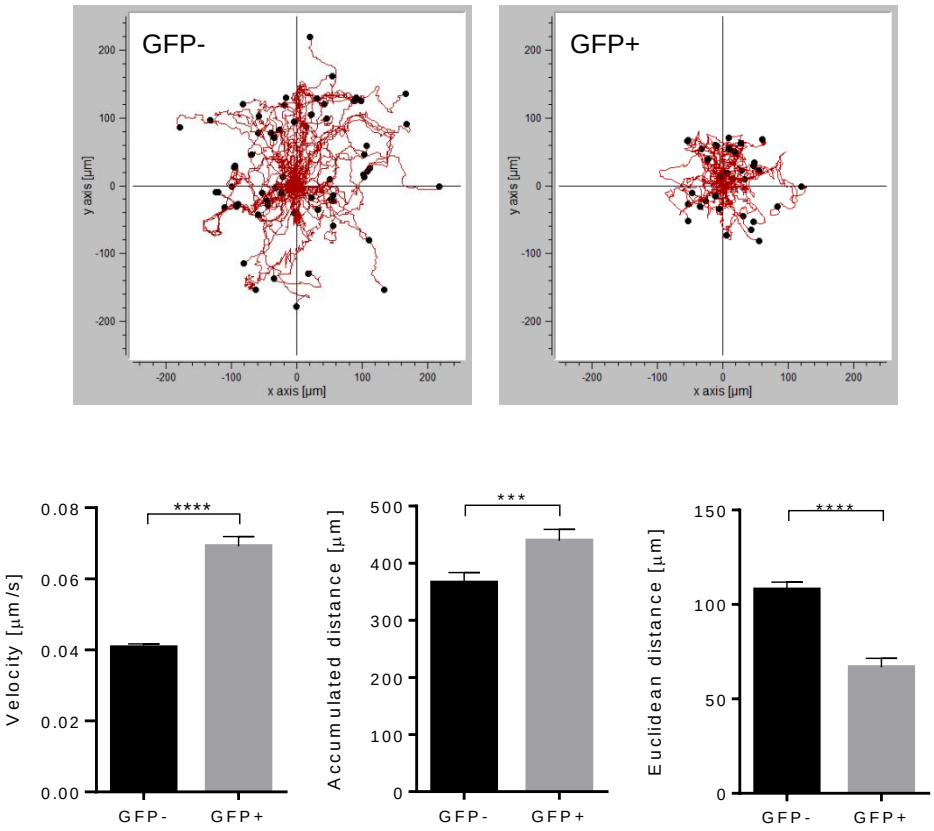

Figure 30 Enhanced random migration of GFP+ DCs in collagen matrices.
Representative single-cell trajectories graph recorded for 90 min of GFP- (top panel left) and GFP+ (top panel right) DCs embedded in 3D collagen (2 mg/mL) matrices of one data set. Quantification of single-cell tracks analysis for mean velocity (bottom panel left), mean accumulated distance (bottom panel middle) and mean Euclidean distance (bottom panel right) (n=7 donors in 6 independent experiments). (77).

As enhanced migration of GFP+ DCs is maintained also in collagen matrices where migration is random, paracrine signals potentially provided by H358 cells or fibroblasts in the 3D respiratory models are not likely to contribute (Figure 30).

4.6 GFP+ and GFP- MV-DCs preferentially use different migration modes

To define whether GFP+ MV-DCs indeed differ with regard to their migration mode from their GFP- counterparts, MV-DCs were exposed to the ROCK inhibitor Y27632, which is known to interfere with amoeboid migration (45) prior to the random migration assay. This inhibitor specifically reduced the mean velocity of GFP+ DCs, which was also slightly affected for GFP- DCs. The same applied to this is while the differences seen for accumulated distances covered by both populations, which also proved to be sensitive to ROCK inhibition (Figure 31). Their higher sensitivity of both migration parameters to ROCK inhibition suggests that GFP+ DCs predominantly use the amoeboid migration mode.

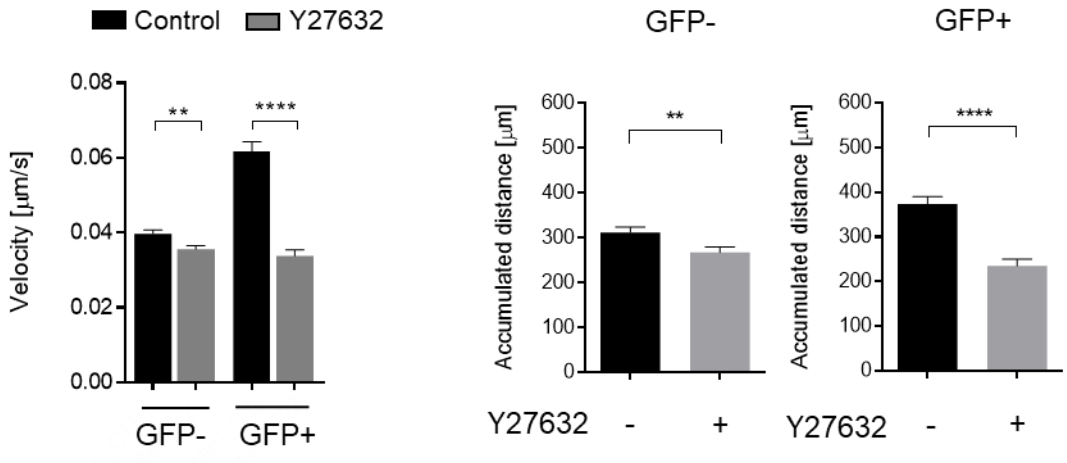

Figure 31 An amoeboid mode of migration is preferentially used by GFP+ DCs.
Velocity (left graph) and accumulated distance (middle and right graphs) of single-cell trajectories of GFP+ and GFP- MV-DCs pre-exposed to Y27632 inhibitor treated (30µM) or not (Control) in

the collagen matrix (2 mg/mL). Graphs show mean ± SEM of three independent experiments, each consisting of one donor in three replicates. (77).

Because their migration characteristics are less sensitive to an inhibitor of amoeboid migration (Figure 31), are less polarized and reveal increased filopodial activity (Figures 25, 28 and 29) GFP- DCs obviously prefer a mesenchymal-like mode of migration. Formation of adhesive structures like podosomes is typically observed for cells using a mesenchymal mode of migration (44), and therefore, these were analyzed in both populations in MV-DCs seeded onto FN. As typical for podosomes, f-actin and vinculin were co-detected in rosette-like structures in GFP- DCs, but not in GFP+ DCs indicating that in GFP+ DCs did not form or had dissolved podosomes (Figure 32).

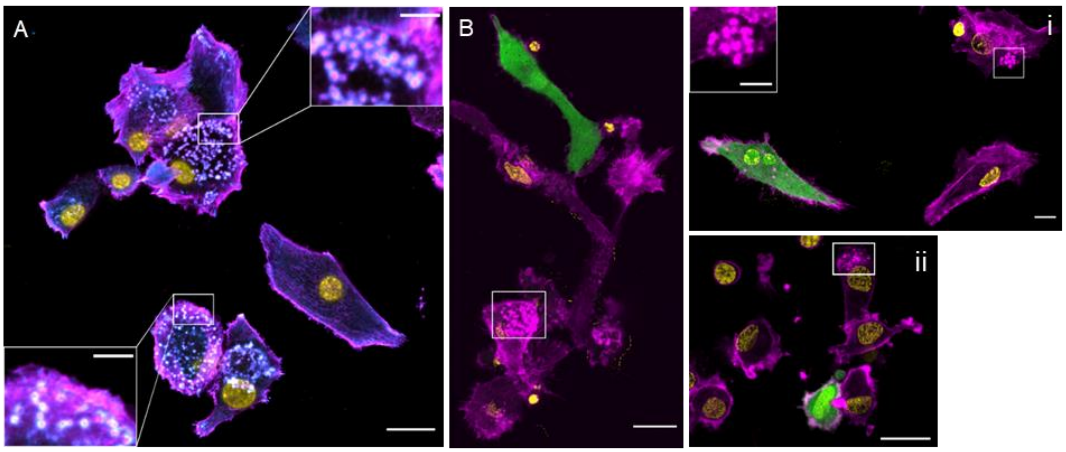

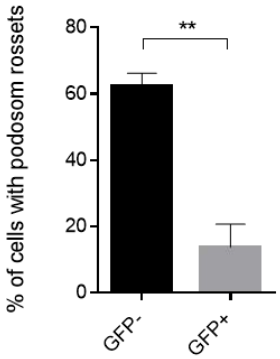

Figure 32 Podosome rosette structures prevail in GFP- DCs.
Vinculin (cyan), f-actin (magenta), MV (GFP) and nuclei (yellow) were co-detected in MV exposed DCs seeded on FN for 2h. Overviews are shown in (A) and (B) (scale bars, 20µm), insets in (A) show magnifications of podosomal structures prominently seen in GFP- cells. In (B) boxed regions highlight the podosomal structures which are not present in GFP+ DCs (scale bars, 5µm). Images are representative for four independent experiments. C) The percentage of DCs with podosome rosettes was measured in each group. The graph shows the mean ± SEM of four independent experiments, each consisting of one donor. At least 60 cells were analyzed per group. (77).

As reported earlier, Filamin A (FLNa), an actin-binding protein, localizes to and stabilizes podosomes in mesenchymal migration (94). To evaluate whether MV infection would affect FLNa, levels of its overall accumulation were comparatively analyzed in immature DCs and MV exposed DC population revealing infection levels of higher than 50% (Figure 33).

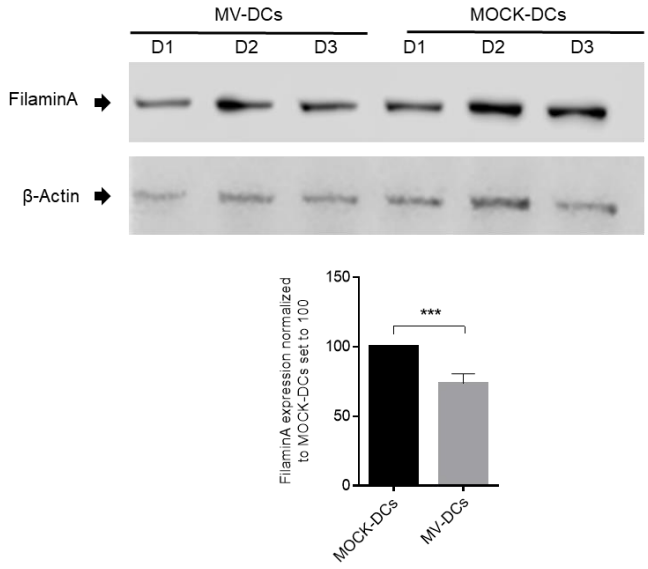

Figure 33 MV infection in DCs reduces the accumulation of Filamin A.
Western blot against FLNa (top) and β-Actin (bottom) as a loading control, in immature iDCs or MV-DCs 24 hrs post-infection in independent DC donor (D1-3). The graph shows the quantification of FLNa expression as mean ± SEM of 3 independent experiments each including

at least two independent donors. Values from each experiment are normalized to the iDC group set to 100.

Consistent with the absence of detectable podosomes in GFP+ MV-DC (Figure 32), accumulation of FLNa was significantly reduced in MV-DCs (Figure 33) indicating that lack of this stabilizing factor might further characterize and even contribute to the usage of differential migration modes of in 3D. Because cell lysates analyzed were obtained from the bulk MV-DC culture, it was not possible to attribute alterations in FLNa to specific populations in MV-DCs. To verify that, as might be expected from the literature (94), high levels of FLNa would be retained in GFP- and not in GFP+ DCs, this protein was co-detected with podosome rosette structures at a single-cell level. Indeed, FLNa was efficiently identified as part of these particular structures in GFP- DCs while it was virtually absent from GFP+ DCs which also failed to reveal podosomes (see below, Figure 34).

In order to show the localization of FLNa and probable colocalization of FLNa with the podosome structures in MV-DCs, IF staining for FLNa, vinculin, and F-actin on MV-DC cultures which were seeded onto fibronectin (FN) coated channel slides was performed (Figures 34 and 35).

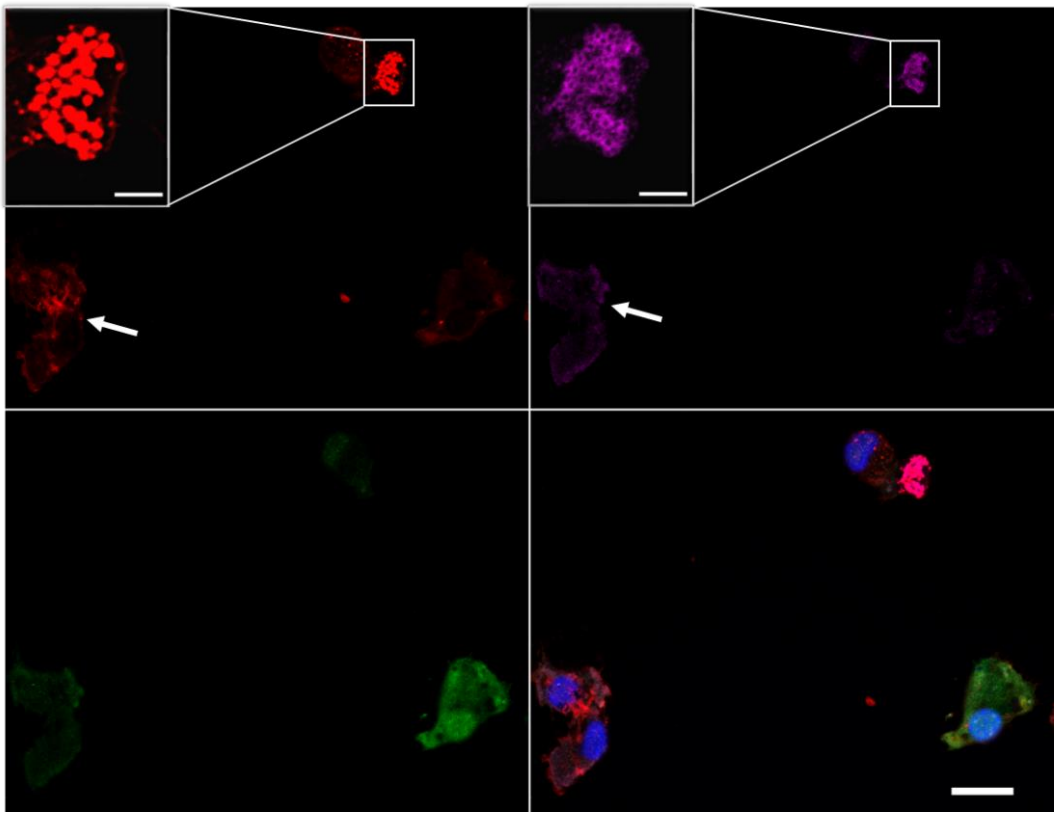

Figure 34 FLNa is localized at the podosome rosettes.
IF staining of FLNa and vinculin on MV-GFP DCs 2h after seeding on a fibronectin-coated channel slide. Vinculin (red), FLNa (magenta) and MV-GFP (green) are shown in single channels, and the overlay is shown with the DAPI (blue) staining (bottom right panel), scale bar: 20µm. Insets show the magnification of selected regions in each channel (podosome rosettes), arrows point to the vinculin and colocalizing FLNa signals in other GFP- cells. Scale bars: 5µm.

In confocal images in Figure 34 vinculin staining imaged with 647 laser is shown in red and a magnification of the selected region as an inset as well as the FLNa staining using 555 laser line and shown in magenta (Figure 34).

Slight cross-talk between the 555 filters (for FLNa detection) and 488 (for MV-GFP detection) caused the visible background for FLNa signal in the 488 channel (Figure 34, bottom left panel).

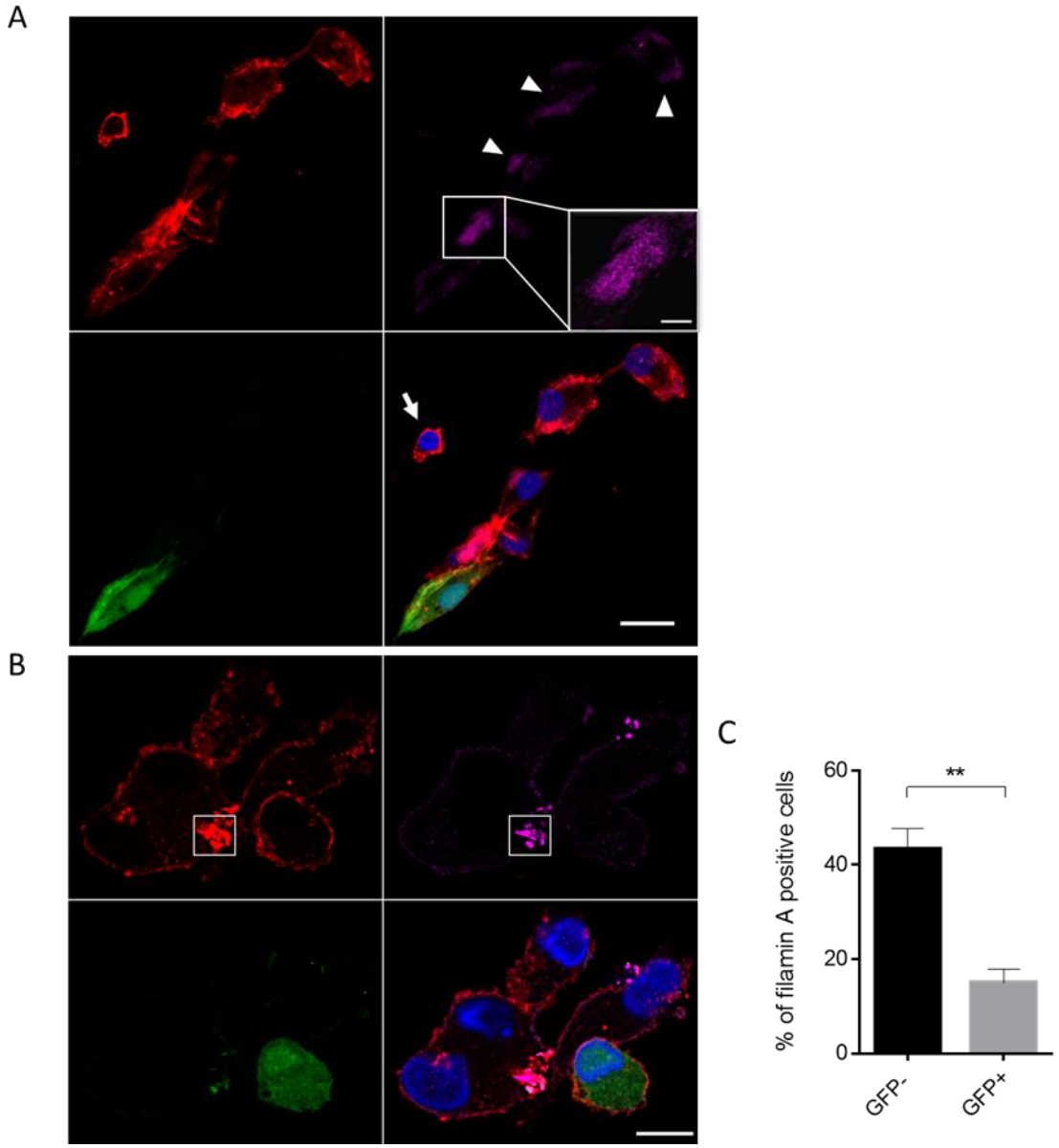

Figure 35 FLNa is more prevalent in GFP- DCs.
IF staining of FLNa and phalloidin on MV-GFP DCs 2h after seeding on a fibronectin-coated channel slide. Phalloidin (red), FLNa (magenta) and MV-GFP (green) are shown in single channels and the overlay is shown with the DAPI (blue) staining (bottom right panel). A) Insets

show the magnification of selected region in FLNa channel (podosome rosette), scale bar: 5µm. Arrowheads point to FLNa signal in podosome rosettes in GFP- DCs. Arrow points to a T-cell with phalloidin and DAPI signal only. B) Colocalization of FLNa with actin cores (red points) shown in selected regions, representing adhesive structures. C) The graph shows the quantification of FLNa positive GFP- and GFP+ MV-DCs as a mean ± SEM of three different experiments. At least 50 cells were analyzed per group. Scale bars: 20µm.

According to the confocal images, FLNa mostly colocalizes with the podosome structures but also was seen in the actin enriched regions (Figure 35 A, B). For a better comparison of FLNa expression in GFP+ and GFP- DCs by confocal microscopy, the number of cells with visible FLNa signal was quantified (Figure 35 C).

FLNa expression was also measured by flow cytometry in immature DCs and MV-DCs, and the MFI levels were accordingly calculated (Figure 36).

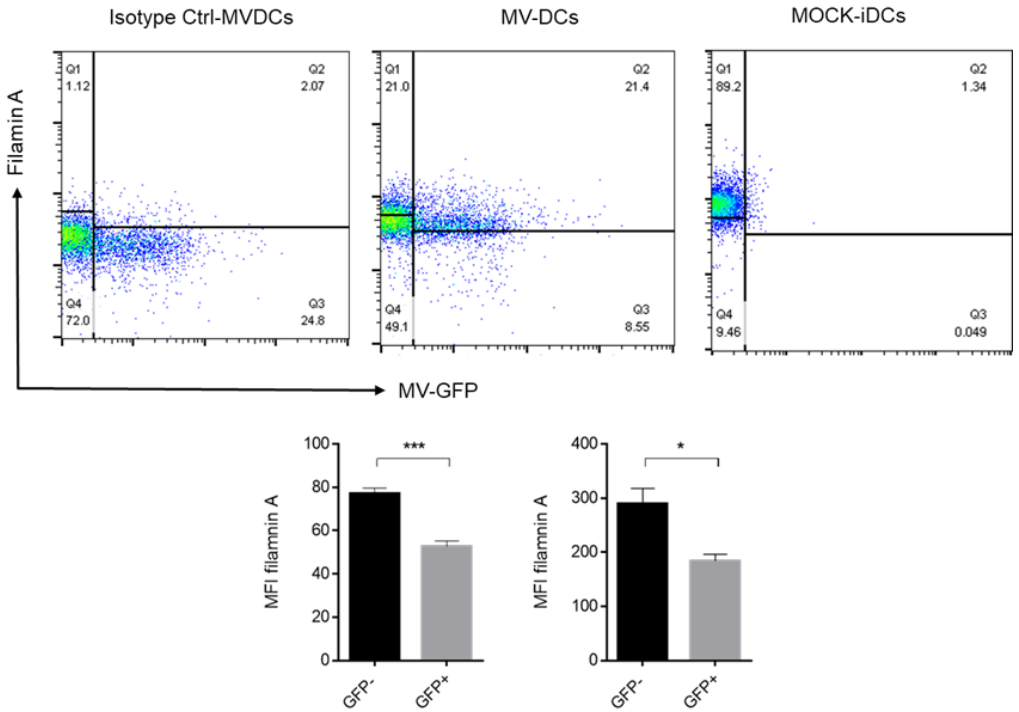

Figure 36 Flow cytometry analysis of FLNa expression in DCs.
Dot blot shows the gating strategy for double detection of MV-GFP and FLNa signal in MV-DCs and iDCs according to the isotype ctrl. Each bar graph shows the mean ± SD of FLNa MFI in one DC donor in 3 replicates. In two independent experiments.

This data consistent with podosome rosettes high frequency in GFP- DCs show that filamin A is also more prevalent in these cells (GFP-) and according to the published reports might contribute to podosome formation and stabilization in these cells.

4.7 The role of the Sphingosine kinase/sphingosine 1-phosphate system in MV transmission

Results obtained so far imply that enhanced migration of MV-infected DCs occurs cell-autonomously, i. e. in the absence of paracrine signals from epithelial or fibroblast cells. Therefore, underlying mechanisms most likely are modulated by infection per se and act to promote cytoskeletal remodeling and mainly ameboid migration of DCs. As shown for other immune cells, sphingosine-1-phosphate (S1P) can act as a potent migrational cue (95, 96). Production and activity of this particular bioactive sphingolipid appeared as highly promising effector promoting migration of MV-infected DCs. This is because MV replication in some cell lines was found to be sensitive to inhibition of sphingosine kinase and enhanced by sphingosine kinase I overexpression suggesting that MV infection triggers activation of this enzyme and production of S1P (15).

4.7.1 MV-infection induces S1P production in DCs

To evaluate the role of SphK/S1P system in contribution to enhanced migration of infected DCs, intracellular S1P levels were determined in DC cultures exposed to MV

or MOCK for 24 h by LC-MS/MS. After normalization to the levels measured in MOCK exposed DCs, S1P levels were found to be significantly increased in MV-DC cultures revealing high infection levels (>50%) (Figure 37).

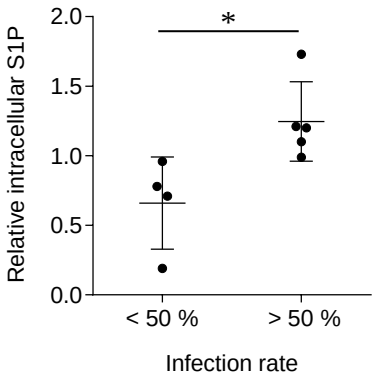

Figure 37 Higher intracellular S1P levels in highly infected DC cultures.
Intracellular levels of S1P were measured in MV-infected DC cultures after 24h (infection levels were determined by viral N protein FACS staining prior to the measurement) and normalized to values obtained from each respective individual culture exposed to a MOCK preparation (set to 1). The graph represents each pairwise analyses for cultures revealing infection levels lower (20-49%, n= 4) and higher (56-78%, n = 5) than 50% with mean values differing significantly (p = 0.0159, two-tailed Mann-Whitney test) between these two groups. (77).

These results indicate that S1P may be specifically produced by infected DCs. This could not be verified to occur in this particular population by LC-MS/MS because sorting of cells required for the distinction of GFP+ and GFP- cells causes cell stress and thereby directly affects sphingolipid levels. An S1P specific antibody potentially allowing for this distinction of this low abundant bioactive metabolite at a single cell level is not commercially available.

1.6.2. The role of sphingosine kinase MV transmission

In order to verify the contribution of sphingosine kinase to the enhanced velocity of GFP+ DCs and thereby, ensuing MV transmission to epithelial cells, the impact of the SphK inhibitor SKI-II on DC migration was tested. Prior to the main experiments, the cytotoxicity of this inhibitor for DCs was analyzed by detection of annexin V binding and/or PI incorporation by flow cytometry. The results showed that the exposure to SKI-II was not toxic at any of the concentrations tested (Figure 38). Because it proved to be effective at inhibiting SK-II in other cell types (97) a concentration of 10 µM was chosen for further experiments.

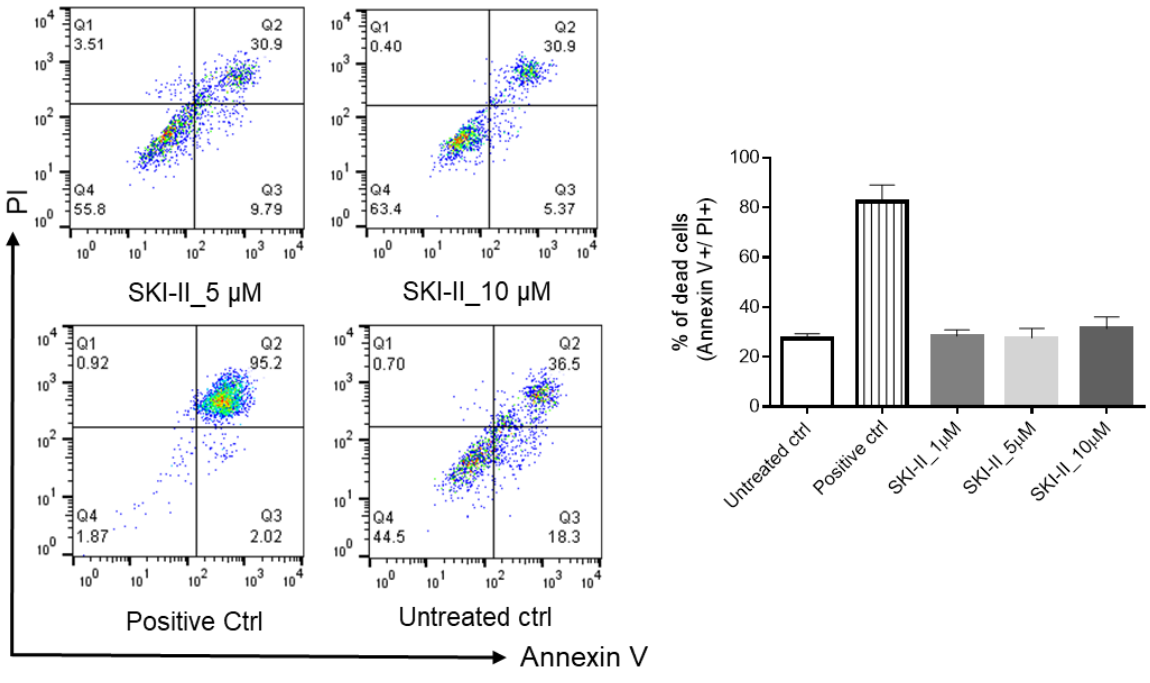

Figure 38 Cytotoxicity of SKII inhibitor in DCs.
SKI-II was applied on DCs at concentrations of 1µM, 5 µM and 10 µM for 24h. Annexin V/ propidium iodide (PI) staining was performed and analyzed by flow cytometry. Graphs show the gating strategy to separate living cells (Q4-bottom left quadrant), early apoptosis (Q3-bottom right) and dead cells (Q2- upper right). The bar graph shows the mean ± SEM percentage of

dead cells in 3 replicates. Positive Ctrl of the staining shows the dead cells (heat-induced cell death).

In contrast to what has been reported for other cell types (97), exposure to SKI-II at this concentration for 2h prior to infection did not affect MV replication in DCs within 48 hrs and only slightly after 72h (Figure 39).

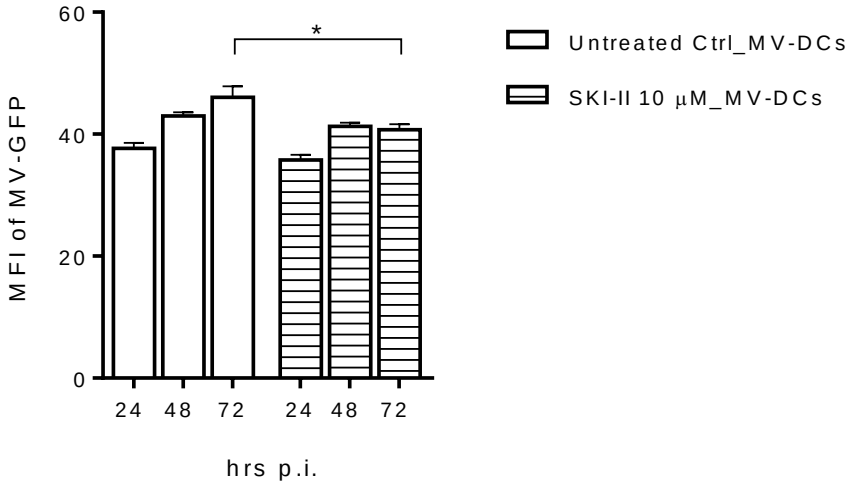

Figure 39 SKI-II does not affect MV replication in DCs
DCs were pre-exposed to SKI-II (10 µM) or the solvent (DMSO) for 2h and infected with MV for the time intervals indicated after which GFP signals were detected and quantified by flow cytometry. The graph shows the mean ± SD of MFI of three replicates.

To evaluate whether sphingosine kinase activity in infected DCs has any role in MV transmission to the DC target cells, the efficiency of GFP acquisition by H358 cells from MV-DCs pre-exposed to SKI-II or not was comparatively analyzed in 3D respiratory models and standard 2D co-cultures. Treatment of MV-DCs with SKI-II reduced transmission of MV to H358 cells in 3D respiratory models, but did not affect that measured under 2D conditions (Figure 40) indicating that sphingosine kinase activity is not important for the transmission process itself also including formation of

transmission interfaces and may rather affect migration and thereby, access to the target cells in 3D.

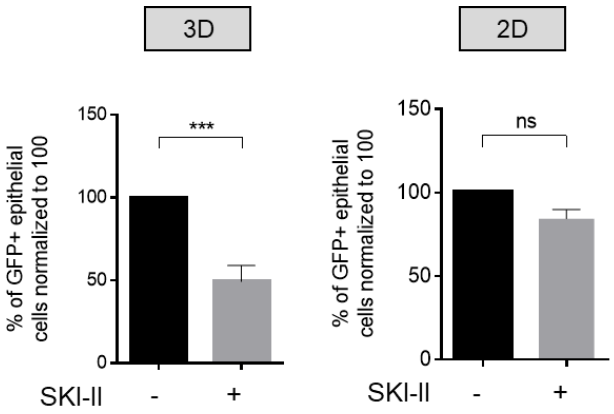

Figure 40 SphK inhibition results in decreased MV transmission to H358 cells only in 3D respiratory models.
Detection of MV transmission to H358 cells (shown as % GFP+ H358 cells) from MV-DC cultures treated with SKI-II (10 µM) or not (Ctrl) in 3D tissue models (left) and 2D co-cultures (right) 4 days after addition of MV-DCs by flow cytometry. Data represent the mean ± SEM of at least three independent experiments, normalized to the untreated control group. (77).

Consequently, the impact of sphingosine kinase activity on the migration of MV-DCs in collagen matrices was directly analyzed. SKI-II pre-treatment substantially reduced the velocity of MV infected (GFP+) cells, but not detectably GFP- cells in this substrate (Figure 41) indicating that sphingosine kinase activity is specifically required for promoting ameboid migration of infected DCs. Surprisingly, the Euclidean distance in GFP- DCs was slightly increased due to the SphK inhibition showing the movement of cells with fewer turns in comparison to the untreated control group.

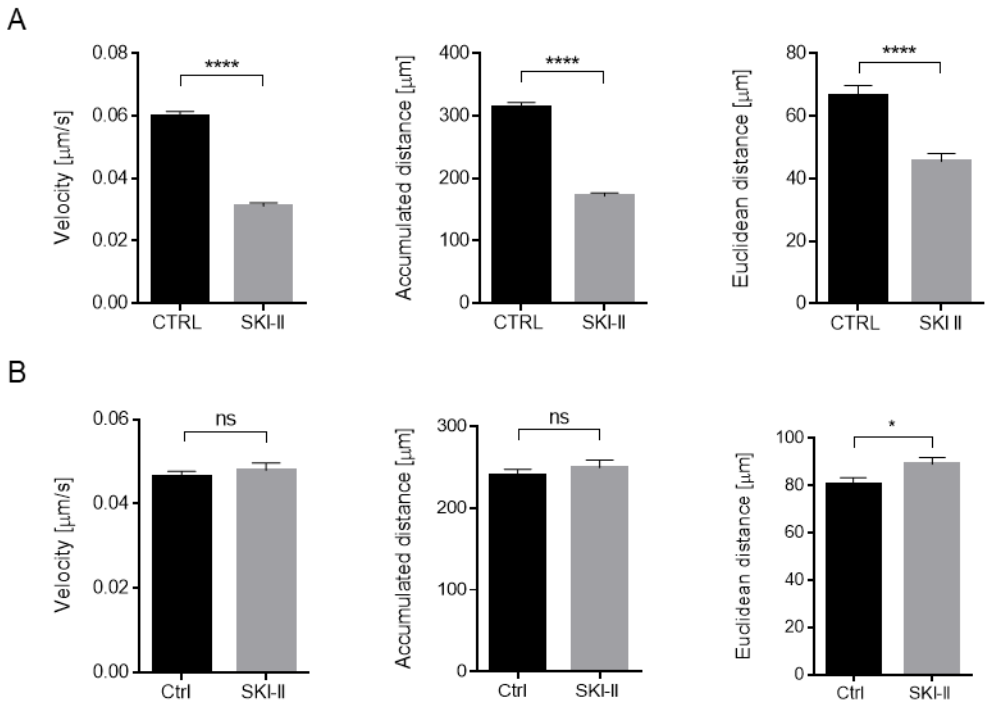

Figure 41 SKI-II direct effect on GFP + and GFP- MV-DCs migration.
Quantification of velocity (left), accumulated (middle) and Euclidean distances (right) measured in single-cell trajectories of GFP+ DCs (A) and GFP- DCs (B) treated with SKI-II (10 µM) or not (CTRL) in 3D collagen (2 mg/mL) for 90 min. (77).

4.7.2 The role of S1P in MV transmission

Having established the importance of sphingosine kinase activity in DC motility and subsequent transmission does not equate to having established the role of S1P in this process because Sphingosine kinase inhibition could result in sphingosine accumulation, too. Therefore, the next set of experiments specifically addressed the importance of S1P in MV-DCs. Although S1P can regulate cellular functions as an intracellular second messenger, its activity after export and interaction with S1P receptors has mainly been investigated (98, 99).

4.7.2.1 Elevation of intracellular S1P levels promote DC migration

To establish whether elevation of intracellular S1P per se acts to foster DC migration, the following experiments included immature DCs supplemented with D-erythro-sphingosine-1-phosphate or caged S1P (described in 3.12).

For this, cells are fed with caged S1P for 2h, and thereafter exposed to UV light irradiation. Thereby, the caging groups are released from the S1P, which leads to the intracellular release of S1P. In the first set of experiments, the cytotoxicity of this molecule used at a concentration reported to be effective before (100) prior to and after UV illumination was tested (Figure 42).

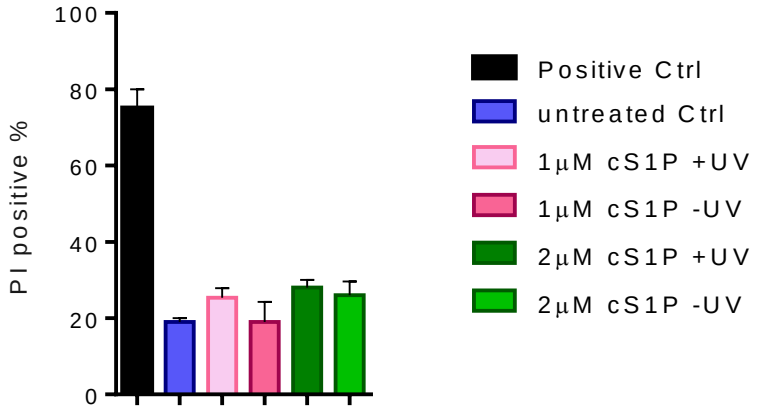

Figure 42 Cytotoxicity of caged S1P with/without UV illumination.
iDCs were loaded with 1 and 2µM of caged S1P for 2hrs and then exposed to UV (uncaged S1P) or not. PI staining was performed 5 hours after S1P addition. Positive ctrl of the staining shows 75% of heat-induced dead cells.

Apparently, the random migration of iDCs was enhanced upon UV activation of caged S1P while the uncaged molecule did not affect all parameter measured (Figure 43). These findings indicate that elevation of S1P levels in DCs substantially impact on their

migratory behavior thereby supporting the hypothesis that virally induced S1P (via sphingosine kinase activity) is of importance in enhanced motility of MV-DCs in 3D.

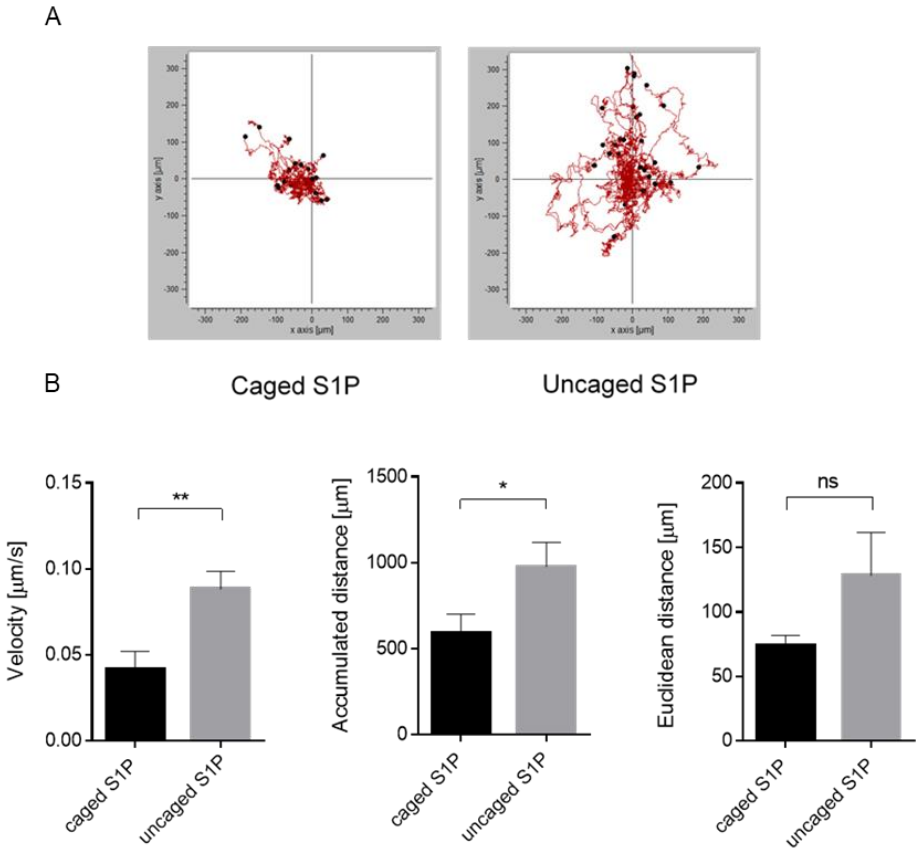

Figure 43 Random migration in collagen matrices of iDCs loaded with caged S1P.
Random migration of DCs in the presence of intracellular S1P caged (-UV) or uncaged (+UV) in 3D collagen (2 mg/mL) for 90 min. A) One representative iDCs single-cell trajectory analysis. B) Quantifications of single-cell trajectories of iDCs in the presence of intracellular caged (without UV illumination- black bars) or uncaged (after UV illumination- gray bars) S1P. Graphs show the mean ± SD of three independent experiments, each involving one donor in three replicates.

4.7.2.2 S1P acts to support DC migration via S1P receptors

To investigate whether S1P (as accumulating in MV-DCs, Figure 41) impacts on MV-DC migration after export and autocrine interaction, MV-DCs were treated with VPC,

an inhibitor blocking signaling via S1P receptor subtypes 1 and 3 ($S1PR_1$ and $S1PR_3$) prior to embedding into collagen matrices. In preparation of these experiments, the cytotoxicity of VPC (used at a 10 µM concentration reported to be effective earlier (101)) for MV-DCs was tested. At this concentration, VPC did not affect DC viability (Figure 44).

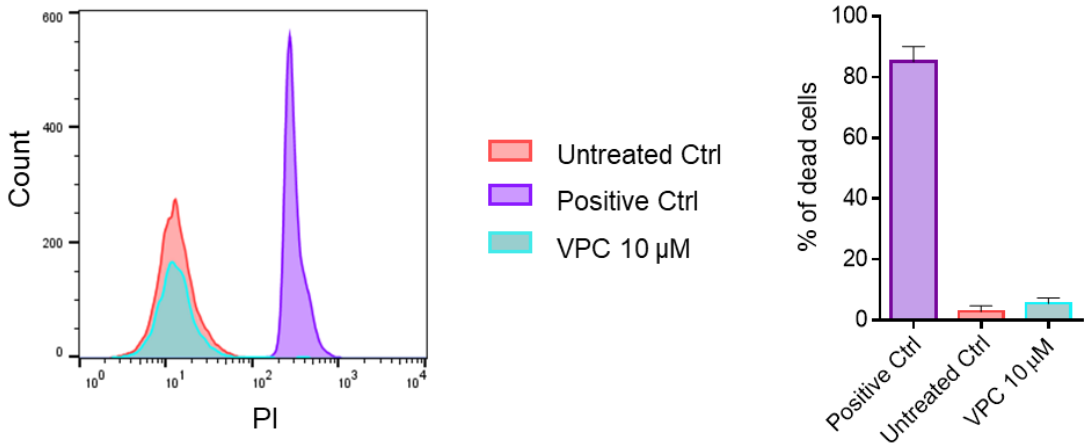

Figure 44 Cytotoxicity of VPC inhibitor in DCs.
VPC was applied on MV-DCs at 10 µM for 24h. Histogram representation of Propidium iodide (PI) staining analyzed by flow cytometry (left panel). PI-positive Ctrl shows the dead DCs (heat-induced death). The bar graph shows the mean ± SD of 3 replicates.

VPC exposure selectively reduced velocity and accumulated distance of GFP+ DCs and did not remarkably affect the migration parameters of GFP- cells in the collagen matrix (Figure 45). Though not excluding an additional role of intracellular S1P, these findings suggest that S1P receptor signaling acts to promote enforced velocity of infected DCs in an autocrine manner through $S1PR_{1,3}$ to support their fast amoeboid trafficking through the respiratory epithelial tissue.

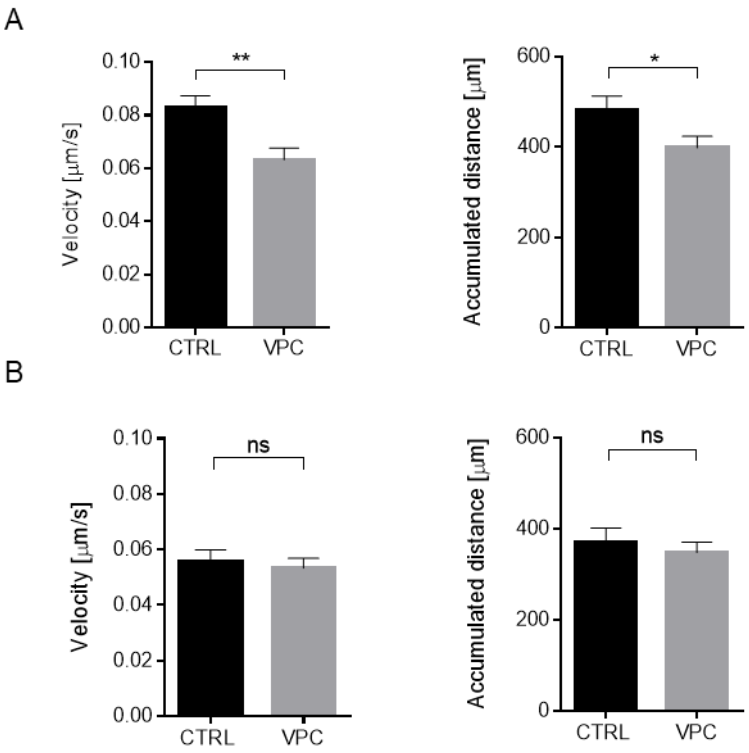

Figure 45 VPC specifically targets velocity and accumulated distance GFP+ DCs in collagen matrices.

Quantifications of single-cell trajectories of GFP+ (A) and GFP- (B) DCs treated with VPC (10 µM) or not (CTRL) in 3D collagen (2 mg/mL) for 90 min. Graphs show the mean ± SEM of three independent experiments, each consisting of one donor in three replicates. (77).

4.7.3 ASM role in MV-infected DCs

S1P is a downstream metabolite of sphingomyelin breakdown and, as described (in the introduction), its accumulation levels are regulated by the activity of various enzymes such as sphingosine kinase, sphingosine lyase, but also S1P phosphatase as well as export efficiencies. An important upstream enzyme involved in S1P production is the acid sphingomyelinase which catalyzes the breakdown of sphingomyelin into ceramide and phosphocholine in response to a variety of stimuli (95). Amongst those, the interaction of MV with DC-SIGN has been described to cause transient ASM activation and membrane ceramide production in DCs (30). Because ASM could also regulate the subsequent accumulation of sphingolipid metabolites in DCs, the next set of experiments focused on determining infection-induced ASM activation and ceramide generation in DCs.

4.7.3.1 ASM activity in DC MV infection

DCs were MOCK treated or MV-infected and harvested after 24 h for detection of ASM activity. As specificity control for the assay, MOCK-DCs were treated with amitriptyline, a known inhibitor of ASM activity (30), which expectedly largely abolished ASM activity in DCs (Figure 46). ASM activity was also found significantly reduced in MV-DCs, with the degree of reduction directly correlating with infection levels indicating that ASM reduction is observed in infected rather than uninfected DCs.

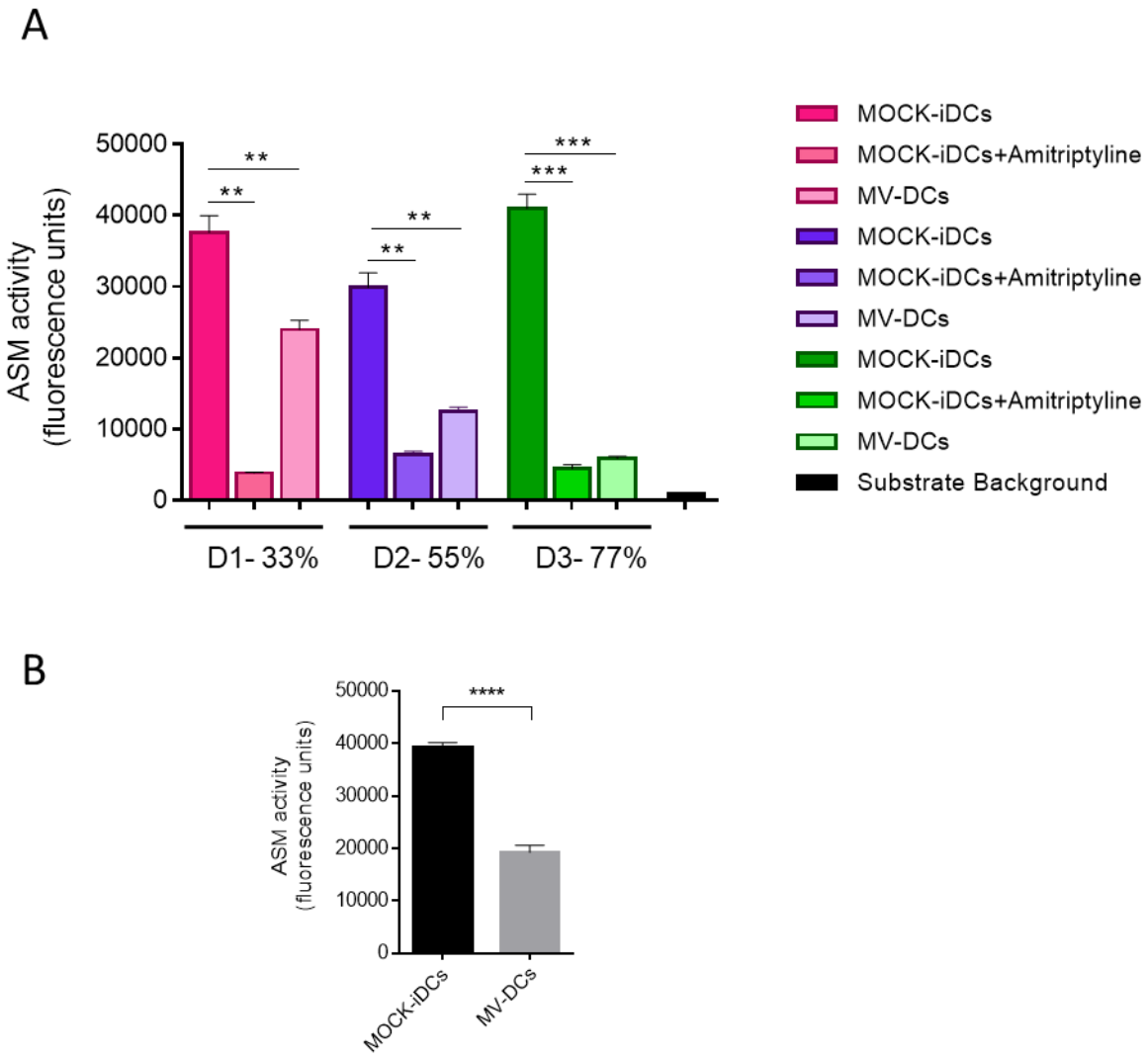

Figure 46 ASM activity in MOCK or MV exposed DCs after 24h.
A) For each donor, shown by color code shades (D1-D3), positive control for ASM inhibition (Amitriptyline (MOCK-iDCs+ Amitriptyline) was included (Middle bar in each donor set). Individual infection rates were determined by GFP detection (in %)(34%, 55% and 77%). Each bar shows mean ± SD of three replicates. The black bar shows the negative ctrl (substrate background) of the assay. B) The same results (without chemical ASM inhibition representation) in (A) are shown and extended to 12 donors and summarized in this graph. The graph shows the mean ± SD of 12 DC donors in at least five independent experiments each in 3 replicates.

Due to the variations between donors and in order to rule out the assay errors this test was performed for 12 independent donors (Figure 46 B).

4.7.4 ASM role in DC migration

The reduced ASM activity in MV-DC bulk culture was suggested to be highly likely due to the GFP+ infected DCs (the negative correlation between ASM activity and infection levels). Considering that in previous parts (see Figure 30), the elevated migration of GFP+ DCs was shown, the probable role of ASM activity in GFP- MV-DCs migration was analyzed. The bulk MV-DC culture was treated with amitriptyline to inhibit the ASM activity in both GFP+ and GFP- DCs as in Figure 46, and subsequently, the cells were embedded in 3D collagen matrices.

The single-cell trajectory analysis revealed that migration factors were all increased in amitriptyline treated GFP- MV-DCs. Velocity is slightly increased; however, this was statistically significant (Figure 47).

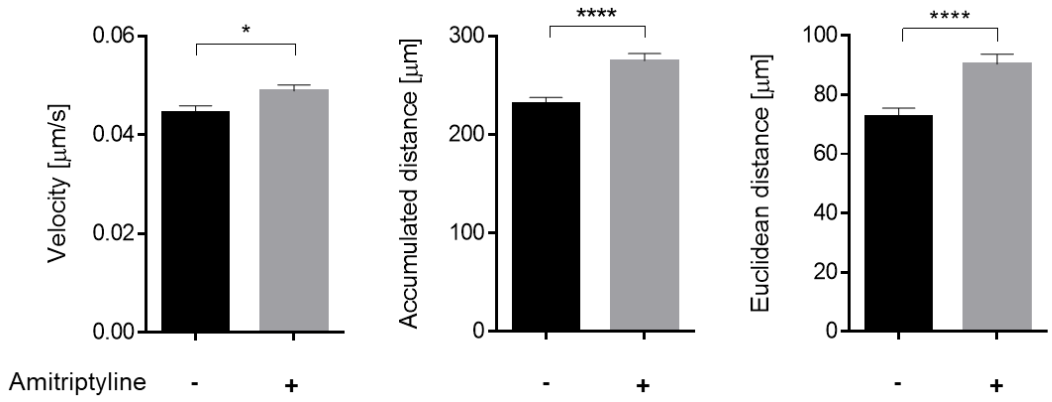

Figure 47 Reduced ASM activity caused elevated migration of GFP- DCs in collagen matrices.

Single-cell trajectories of GFP- DCs were recorded for 90 min when embedded in 3D collagen (2 mg/mL) matrices. Quantification of single-cell tracks analysis of GFP- DCs after 2h

amitriptyline treatment (grey bars) or untreated control (black bars) for mean velocity (left), mean accumulated distance (middle) and mean Euclidean distance (right).

These results, together with the previously shown data on ASM activity in MV-infected DCs (see Figure 46) could show the probable ASM contribution in elevating DCs migration.

4.8 Advancing complexity of the 3D human respiratory tract model: incorporation of the endothelial layer

As so far established, the 3D models proved to be suitable to identify factors important in MV transmission to epithelial cells by migrating DCs which, so far, were directly added basolaterally to the tissue without having to pass an endothelial cell layer on their way from the blood vessels into the connective tissue. It was therefore of high interest to include the endothelial barrier into the model in order to monitor if infected cells would be able to pass this hurdle illustrated in Figure 48 also showing the workflow for these set of experiments).

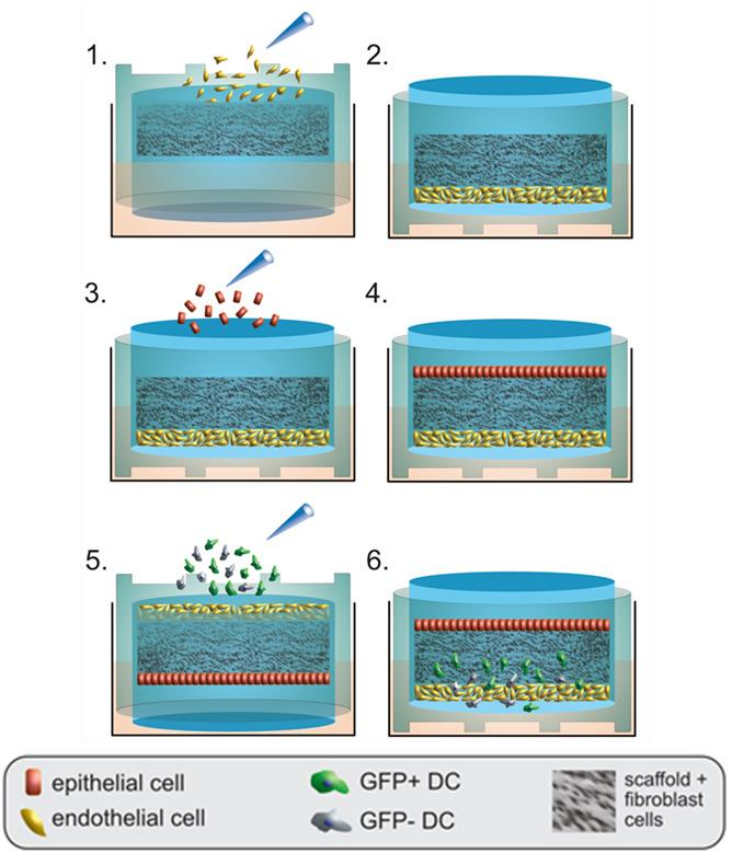

Figure 48 Schematic representation of the advanced 3D respiratory model.
1) Flipping the model up-side-down to add endothelial cells to the basolateral side, 2) reverting the model back to the original orientation after 2h and incubate in 37°C for 2 days, 3) addition of epithelial cells to the apical side, 4) Subsequently, the model was incubated at 37°C for 4-5 days 5) filliping the model to add the MV-DCs to the basolateral side, 6) The whole construct was incubated at 37°C for further experiments.

4.8.1 Supplementation of the 3D respiratory model with endothelial cells

Human umbilical vein endothelial cells (HUVECs) were added to the basolateral side of the 3D models as described in methods and materials and illustrated in Figure 48. HUVECs formed a monolayer on the basolateral side of the collagen scaffold as shown by staining for VE-cadherin (Figure 49). The figure shows a z-stack of the endothelial layer where the first stack (left) and a middle slice with the bright field channel (right) representing the collagen scaffold with the visible collagen fibers can be discerned.

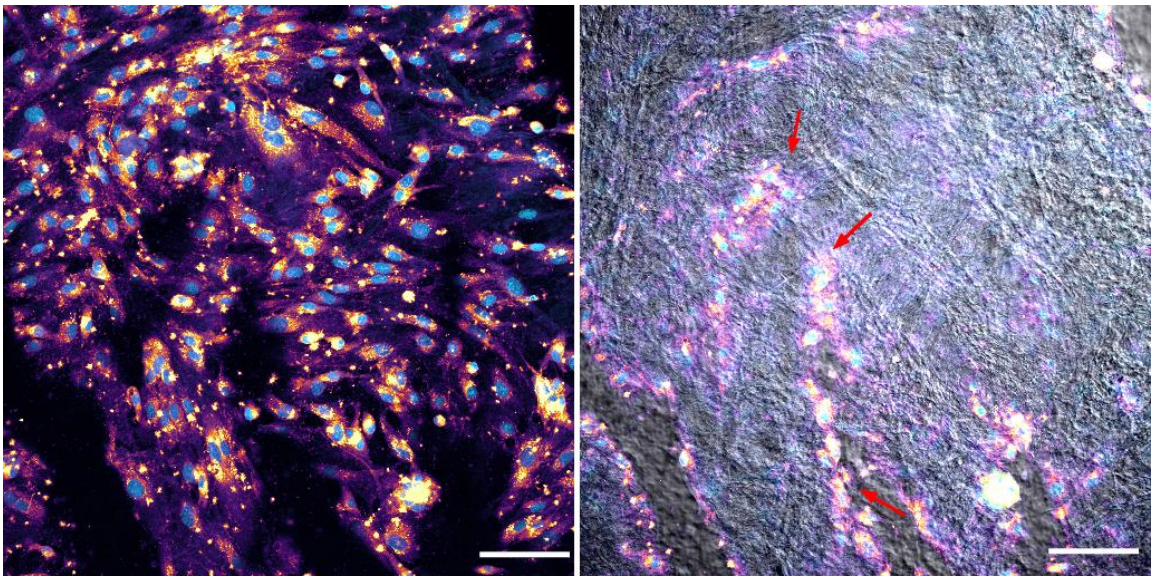

Figure 49 Confocal image of the endothelial layer on the basolateral side of the 3D respiratory model.
First (left) and a middle (right) slice of a z-stack from endothelial layer seeded on the basolateral side of the collagen scaffold as described. HUVECs were stained with the specific VE-cadherin antibody shown with mpl-inferno LUT (look-up-table) from ImageJ. Nuclei were stained with

DAPI shown in cyan. The right image representing the collagen scaffold in grey with, and left image without the bright field channel is shown. Scale bar: 100 µm.

The collagen scaffold appears as a relatively dense, non-homogeneous fibrillar matrix with some notches formed in different areas which are preferred sites for HUVECs to accumulate and grow (Figure 49, right, red arrows).

For a better representation of the endothelial layer formation on the collagen scaffold, a z-stack of the same region chosen in Figure 49, is shown as micrographs (Figure 50).

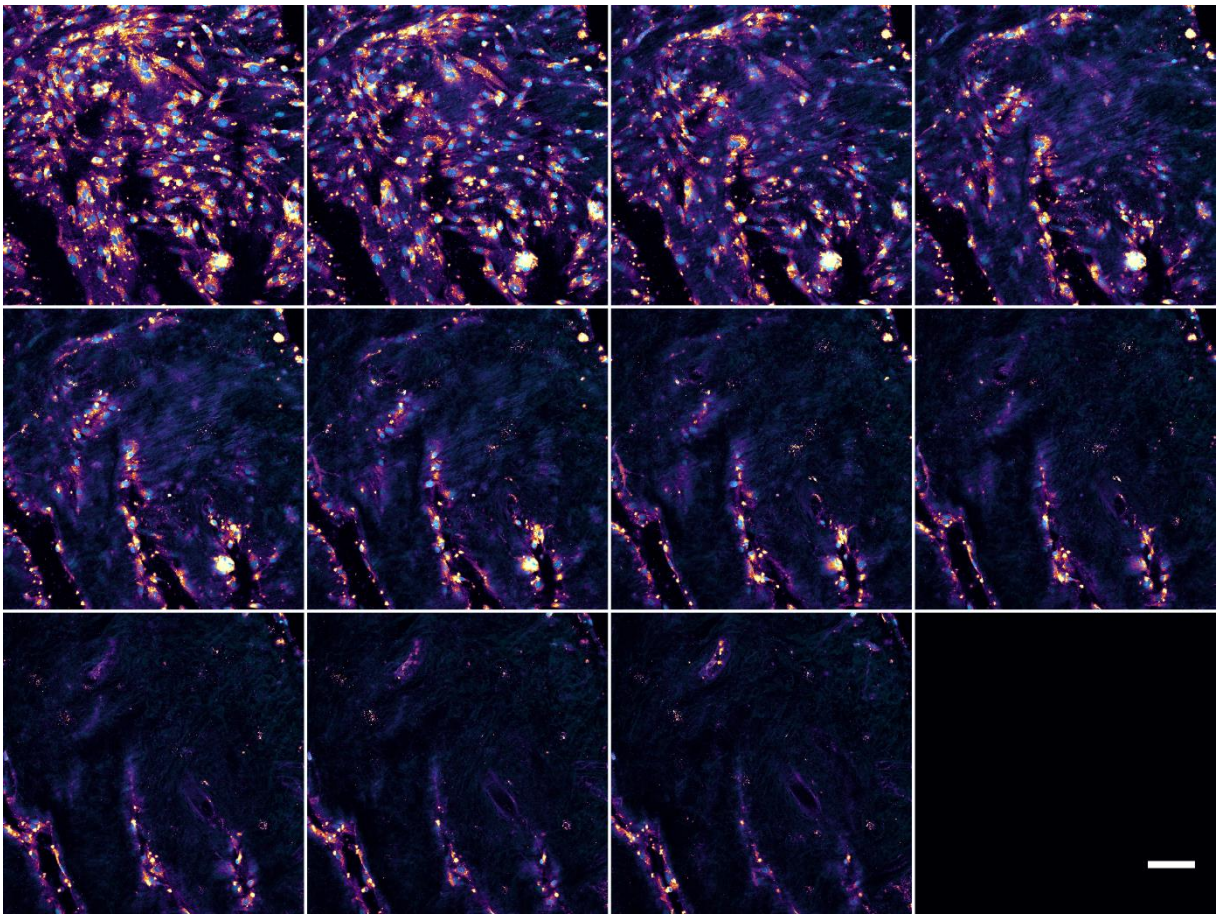

Figure 50 Micrograph representation of a z-stack confocal image of HUVEC layer on collagen scaffold.
HUVECs were stained with the specific VE-cadherin antibody shown in mpl-inferno LUT (look-up-table) from ImageJ. Nuclei were stained with DAPI shown in cyan. Collagen in bright field is not shown. The shown Z dimension here is 11 µm. Scale bar 100 µm.

4.8.2 Epithelial layer features in the presence of the basal endothelial layer

Addition of this endothelial layer to the 3D models did not influence the formation of the apical epithelial layer of the model as confirmed by homogenous E-cadherin staining of H358 epithelial cells after completion of the model (Figure 51) nor did it impact barrier integrity as determined by a FITC dextran assay.

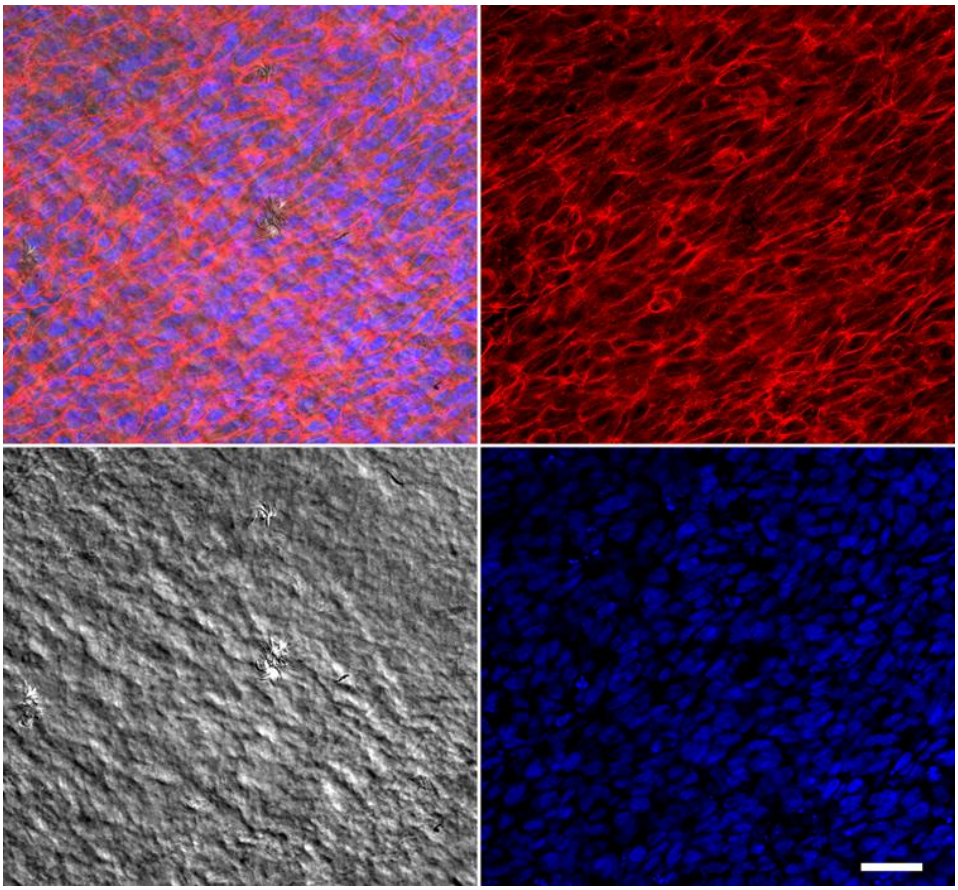

Figure 51 Confocal image of the epithelial layer on the apical side of 3D respiratory model.
The adherent junctions in H358 epithelial cells are shown by E-cadherin staining (top right, red) and Nuclei by DAPI (bottom right, blue). The collagen scaffold is shown in bright field (bottom left, grey) and the channels overlay top left. Scale bar 50 µm.

4.8.3 Addition of MV-DCs to the advanced 3D respiratory model

Following basic characterization of the advanced 3D model, this was supplemented with MV-DCs which were added basolaterally as described in Figure 48. Imaging of the models was performed 24h after addition of MV-DCs (Figure 52).

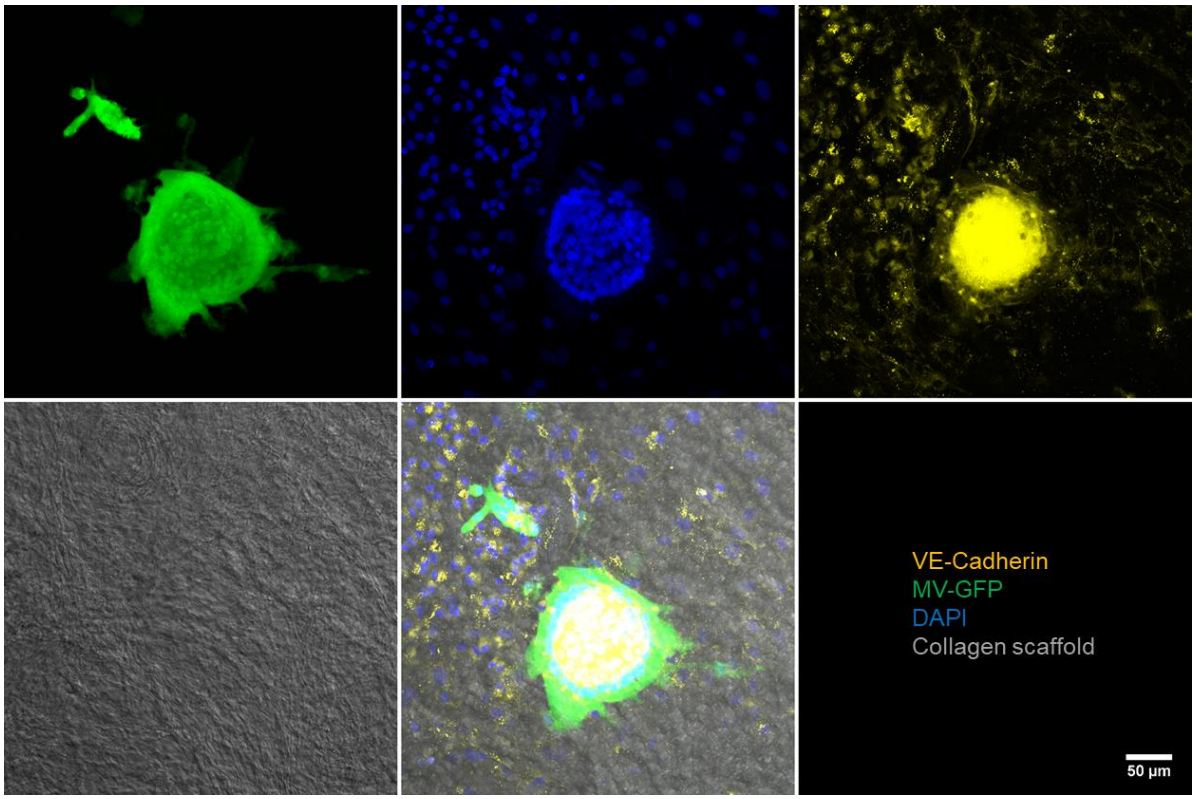

Figure 52 Maximum intensity Z-projection of the endothelial layer after MV-DC reconstitution.
After DC reconstitution the whole model was fixed and accordingly IF staining was performed. HUVECs were stained with the specific VE-cadherin antibody (yellow), Nuclei were stained with DAPI (blue) and MV-GFP in infected cells (green). Z dimension 11 µm. Scale bar: 50 µm.

Addition of MV-DCs onto the endothelial layer caused a massive infection in HUVECs as apparent by the co-detection of MV-GFP and VE-cadherin in this layer. This was more pronounced in the endothelial spheres formed by these cells in notch-areas than in the single cells (Figure 52). Interestingly, MV infection in spheres did not detectably appear to involve cell to cell fusion and syncytia formation, as the adherence junctions shown by VE-cadherin staining were retained and visible in these structures. A better representation of these intact adherence junctions within the MV-infected spheres is shown in Figure 48, in separated slices from the same Z-stack in Figure 53.

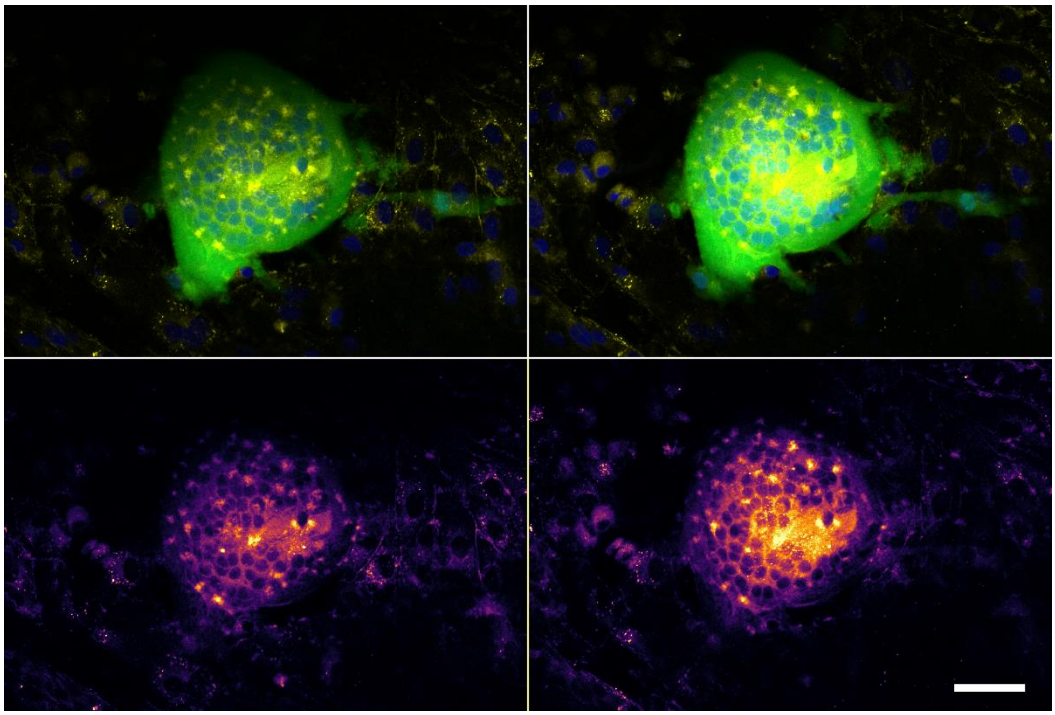

Figure 53 Adherence junctions in MV-infected HUVEC spheres
The adherence junctions are still visible after MV infection caused by MV transmission from MV-DCs. Representative two middle slices of Z-stack in Figure 52, upper row the overlay of VE-cadherin (yellow), MV-GFP (green) and DAPI (blue). The bottom row shows the adherence junctions, single VE-cadherin channel (mpl-inferno). Scale bar: 50 µm.

4.8.4 Formation of vessel-like networks in the endothelial layer

One of the crucial and critical points in tissue engineering and generating ex-vivo infection models is the vascularization. As most of the tissue models for infection studies as well as transplant studies generated in recent years lack the vascular system, they are still named as artificial models and still far from in vivo conditions. It was therefore of particular relevance, that addition of the endothelial layer addition on a biological collagen scaffold indeed created the vessel-like structures and networks inside the collagen matrix (Figure 50). These vessel-like networks are also visible in Figure 54, where the cells cover the edges of some luminal structures of collagen (Figure 54, middle and last rows).

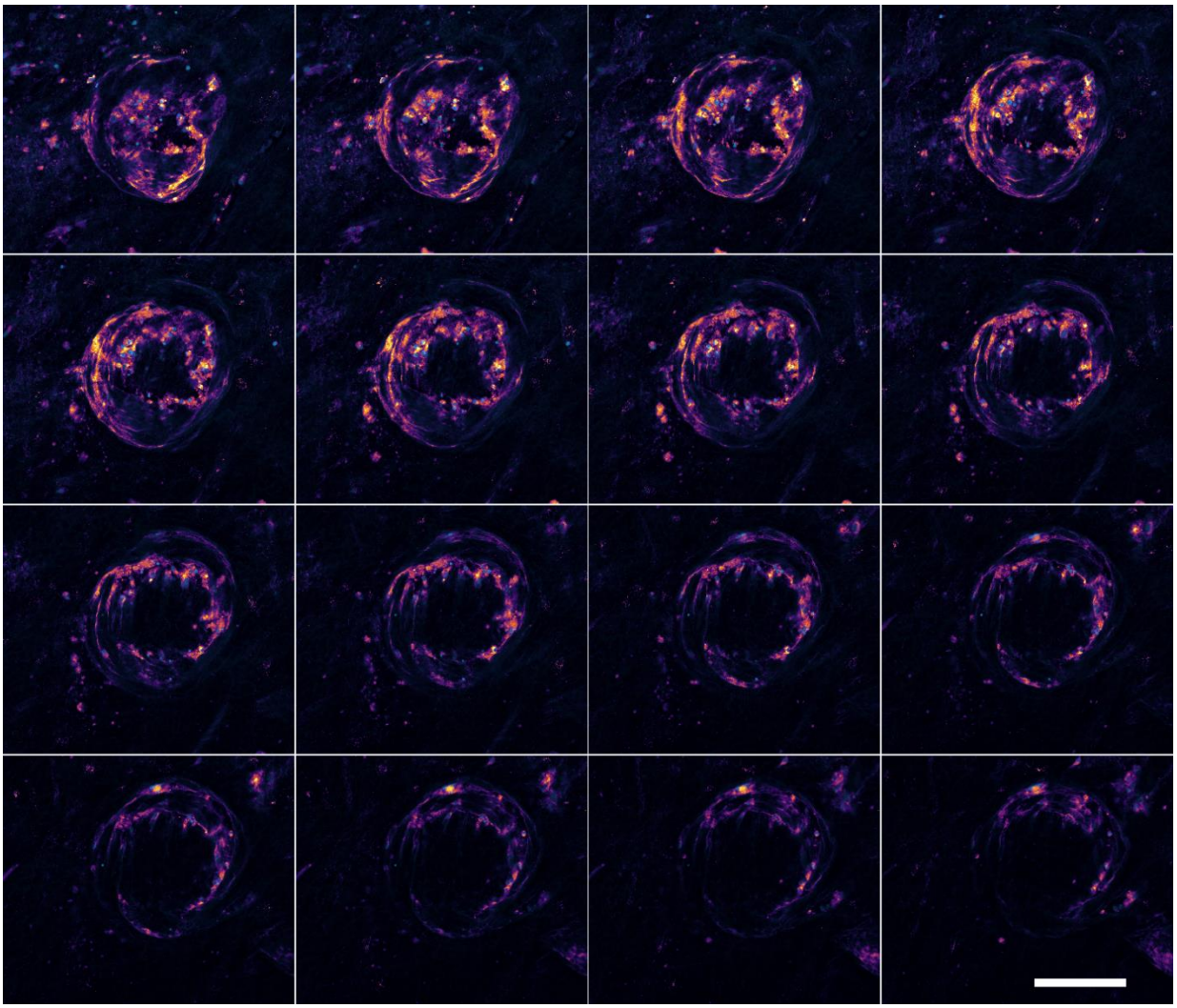

Figure 54 vessel-like structures formation by HUVECs on collagen scaffold.
HUVECs accumulate in luminal structures of collagen scaffold to form vessel like networks. VE-cadherin (mpl-inferno), DAPI (blue). Collagen scaffold in bright field is not shown. Scale bar: 200 µm.

4.8.5 MV transmission to epithelial cells in the advanced 3D respiratory tract model

Upon addition of MV-DCs to the 3D models, they should cross the endothelial barrier so that they can reach the collagen matrix (connective tissue) and finally migrate towards the epithelial target cells for viral transmission. Despite their preferred amoeboid migration mode in dense matrices, which mainly relies on contractile forces (push-and-squeeze) for movement (Figure 31), MV-DCs were able to pass the endothelial layer and transmit the virus to H358 epithelial cells (Figure 55).

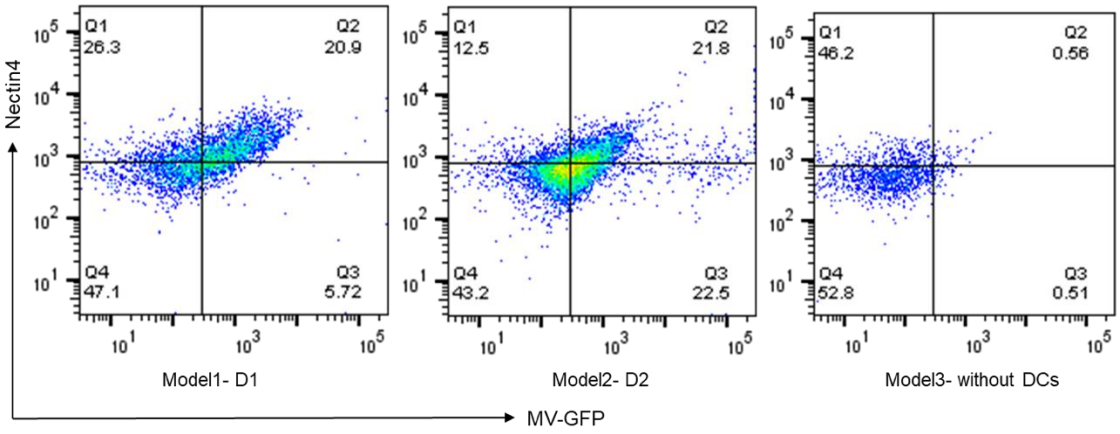

Figure 55 MV transmission from MV-DCs to epithelial cells in 3D models.
Three days after the addition of MV-DCs to the models, MV infection in epithelial cells was detected by the FACS. H358 cells were stained for Nectin-4 which is not expressed on any of the other cell types. The double-positive population for MV-GFP and Nectin-4 is considered as infected epithelial cells. Representative FACS graphs of two independent models with 2 independent DC donors model1-D1 (left graph) and model2-D2 (middle graph) and an infection negative control model without any DCs (right graph) is shown.

These results showing the MV infection in H358 epithelial cells were also confirmed by IF staining and confocal imaging from the whole fixed model (Figure 56) in parallel to

cell recovery from models for flow cytometry analyses. MV infection and cell to cell fusion and formation of syncytia is visible in the epithelial cell layer (Figure 56).

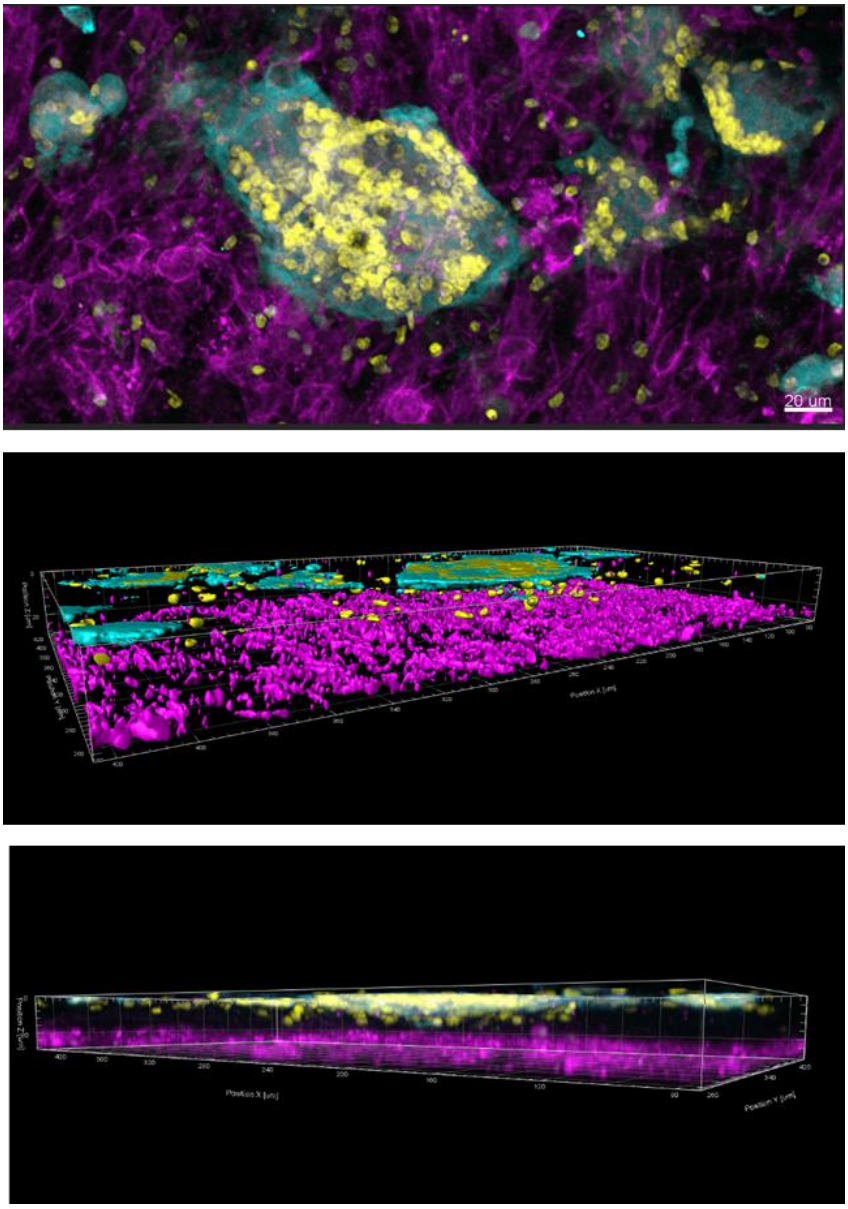

Figure 56 MV infection in epithelial cells in 3D models in the presence of the endothelial layer.

Three days post addition of MV-DCs to the models, MV infection in epithelial cells was detected by IF staining of the complete fixed model. MV-GFP (cyan), VE-Cadherin (magenta) and DAPI (yellow). Syncytia formation in epithelial cells shown as maximum intensity projection of the 3D

volume (top), 3D view of surface modeling (middle) and intensity-based 3D side view. Scale bar (same in all panels): 20µm.

Altogether these results show that the MV-DCs were able to cross the endothelial cell layer and perform the transendothelial migration despite their push-and-squeeze amoeboid migration mode.

5 Discussion

5.1 Establishment of 3D human respiratory tract model to study MV-infected DCs migration and viral transmission

Recent innovative methods in tissue engineering field and developments in generating novel experimental models using primary human cells and tissue have been implemented to study human infectious diseases (102). Considering the importance of these infection models, the establishment of a 3D human respiratory tract model for studying the measles virus infection was described in the first part of the thesis. We took advantage of the previously established 3D respiratory tract model (86) advanced and adapted it for our viral infection studies. This advancement is attributed to the addition of dendritic cells (DCs) and, later on, an additional endothelial layer on the basolateral side of the models.

As particularly important in studying viral transmission to target cells in a 3D environment, motility of the donor cells (DCs) should be maintained in the novel experimental system. This clearly applied to our model system: DCs differentially localized close to epithelial cells and in the middle of scaffold as first shown in the IF stainings of the cross sections of paraffin-embedded fixed tissues (Figure 14) and, later on, by confocal life imaging of the complete model represented in Z-stacks (Figure 21). It is worth mentioning that there are some difficulties in tissue paraffin embedding of these unhandy and extreme thin collagen scaffolds. Especially, this applies to cross sections from the tissue blocks which is to some extent invasive and can cause

mechanical disruption in the scaffold structure which may affect readout of cell positioning. This can also explain the absence of the DAPI signal in some fibroblast cells staining in Figure 11, which might be due to microtome sectioning. Alternatively, cell bodies or nuclei may be only partially visible in a given slice as a section diameter of 5 µm was used.

The fibroblast cells, which migrate to the collagen scaffold upon apical addition to the model and localize within the collagen fibers, play an important role in promoting survival, remodeling and highly resemble human lung mucosa and submucosa (103, 104). It has been shown that fibroblasts interact with the epithelial layer and contribute to the inflammation process and repair of lung tissue (105). Additionally, the cellular interactions between epithelial cells, immune cells (particularly DCs) and fibroblasts in different levels of tissue homeostasis and inflammation have been described (103, 105). Furthermore, as previously described in the other 3D tissue models using the same biological scaffolds, cells seeded on/onto such scaffolds represent more similar physiological characteristics in terms of morphology and functionality, compared to cells cultured on artificial porous PET-membranes (106).

Apparently, neither the scaffold architecture and collagen fibers nor the fibroblasts interfered with the DCs movement as was shown in the static imaging (Figure 21). To confirm this in a more dynamic way, a time-lapse video recording the DC movements in a z-stack covering the whole model height from the basolateral side (where the DCs were added) to the apical layer (where the pre-labeled epithelial cells were visible) was performed and single-cell trajectories of moving DCs were recorded and analyzed by

Imaris software (Figure 22). Surprisingly, quantification of cell tracks revealed higher velocity values and higher track length of MV-infected GFP+ DCs in comparison to GFP- cells in the 3D model. This was also confirmed by the quantification of DCs Z positioning in Z-stack images of the models 2h after DC reconstitution (Figure 23). Errors in this automated cell tracking performed by Imaris software can, however, not be excluded. These can occur due to the high cell density in the tissue and also misplacement or loss of single tracks during the time-lapse in different time frames. In addition to these technical issues, factors released from epithelial cells or fibroblasts which might have specifically confounded recruitment or migration of MV-infected DCs in 3D models. In order to confirm the quantifications in those and also clarify the origin of this migration enhancement, experiments in 3D collagen gel matrices inside channel slides were performed. In this setup, only MV-DCs were embedded in collagen (mimicking the 3D environment) and tracked for 90 mins. Under these conditions, DC migration is random. The manual analysis of single-cell trajectories by image-J revealed the same results as in 3D models showing the higher velocity and accumulated distance of GFP+ MV-DCs (Figure 30). This part of the results proved that the enhanced migration is random and not due to the paracrine signals from the other cells, as there was no other cell type in the channel slides.

This enhanced migration induced by MV infection was characterized in experiments shown in Figures 25 and 26. MV infection was found to promote cytoskeletal activation of DCs, which results in polarization and enhanced velocity as a prerequisite for transmission to epithelial targets. Importantly, the 3D model also recapitulated another

essential late step of MV spread because MV transmission to H358 cells occurred nectin-4 dependently cells as confirmed by imaging and as well as flow cytometric analysis (Figure 19 Figure 20). However, the recovery of cells from the collagen scaffold is not complete, and also virus-induced fusion occurs (fused cells might be lost during recovery or flow cytometry) and therefore, the frequency of infected epithelial cells as determined by flow cytometry may underestimate the efficiency of transmission (Figure 16 and Figure 20). Yet, the infection rates obtained from flow cytometric analysis correlates with that of the intensity-based image analysis from the same models prior to cell recovery (data not shown).

MV infection efficiently promoted actin polarization and enhanced velocity in DCs in both the 3D tissue model and collagen matrices. MV infection caused phenotypic maturation of the entire DC culture in both GFP- and GFP+ populations as characterized by maturation markers (Figure 13), though less efficiently than TLR4 signaling, and this may be carried out by soluble mediators or by TLR2 ligation (40, 88, 107–110).

MV-exposure of DCs was described to affect morphology, migration, and Rac activation earlier (111). In this study, the bulk infected culture was analyzed, and effects were not stratified for infected or uninfected cells. In this thesis, the direct impact of infection at a single cell level was studied. It was shown that MV-induced cytoskeletal activation in infected DCs was of particular importance for efficient transmission to epithelial cells during viral exit (Figure 16). This may rely on fast migration of donor DCs whose viability is known to be limited upon MV infection *in vitro* (107, 108, 112,

113). GFP- DCs also migrated inside the 3D tissue model and towards the epithelial cells (in different angels in x-y-z dimensions, data not shown), though less fast. This was illustrated in the IF experiments on fixed tissues, by detection of DC-SIGN positive DCs 24 h following addition to the models (Figure 14) and also life imaging of 3D Z-stacks (static and time-lapse) detecting DCs localization by life DAPI staining (Figure 21Figure 24). Slow DC migration within a respiratory model (with transwell system and synthetic porous membrane 0.4µm, coated with collagen gel) in the absence of pathogen stimulus from the apical part towards the epithelial layer was previously reported (74). Slow migration in this study was indirectly reflected by the percentage of DC found in the epithelial cell layer in fixed transwells.

If DC stiffness and deformability might be regulated by MV infection and thereby contribute to the fast migration needs to be determined. In transwells with polyester membranes, MV transmission by infected macrophages and DCs to target epithelial cells required large pores with 3 µm size and did not occur with a pore size of 0.4µm (35), while uninfected Mo-DCs efficiently passed through a collagen-coated 0.4 µm polyester membrane to reach epithelial surfaces (74). Higher speed and longer migration paths of MV-infected DCs, especially in Z-dimension in our 3D with dense fibrillar collagen structure model indicates that they are able to efficiently squeeze and can deform both cell body and nucleus. Due to the usage of biological collagen tissue as a scaffold in this study, the density of the collagen fibers can be evaluated using SEM imaging exact while quantification of pore sizes is not possible (114).

5.2 Differential migration modes in MV-infected DCs

In this study, the viral-infection-induced enforced DC velocity was shown firstly in 3D models which contain epithelial cells and fibroblast cells, and later on, this was also shown to be retained in the 3D collagen matrices in the absence of other cell types, indicating that this enforced migration is independent of paracrine signals secreted by other cell types.

Observing this major difference in the migration ability of these cells which did not differ with regard to their phenotypic maturation, prompted us to study the differential migration mode used by the two MV-infected DC populations (GFP+ and GFP-) in detail.

Their high velocity was the first indication that GFP+ DCsd used the fast amoeboid migration mode, which was compatible with the recent reports on human DC migration (44, 115, 116). Secondly, a highly polarized cytoskeleton, f-actin accumulation at the cell rear and sensitivity of their velocity to ROCK inhibition as also typical for an amoeboid mode of migration characterized GFP+ DCs (Figure 25Figure 26Figure 31).

Actin accumulation and myosin II activation at the cell rear defines the uropod structure, which facilitates the cell contractility (92). The latter typically relies on the expression of recombinant fluorophore-tagged myosin II at the uropod which is not achievable in MV-infected Mo-DCs. Uropod markers established for T cells (such as pERM or CD43) are not well characterized in DCs and also did not mark the DC uropod in this study (data not shown) (117). The functional importance of myosin II activation was shown

by the inclusion of the ROCK inhibitor Y27632, which also decreases myosin II activity (118). Migration factors (velocity and accumulated distance) were specifically sensitive to ROCK inhibition in GFP+ MV-DCs, indicating the importance of myosin II activity in the motility of these cells (Figure 31). These results also confirmed the experiments showing particularly pronounced, functional uropods in the majority of GFP+ MV-DCs (Figure 26). Though, GFP- DCs were also to some extent sensitive to ROCK inhibition. This was only partial and did not affect a major proportion of GFP- cells (extracted from the dot plot of represented single-cell trajectory graphs, not shown) (Figure 31). In GFP- DCs, uropod structures were also discernible by their typical morphology in 3D in collagen matrices (Figure 27 by arrows) where, however, the majority of GFP- DCs revealed pronounced filopodial structures with noticeable activity during migration. These structures were visible on GFP+ DCs, but less frequent and active (Figure 28 Figure 29). These observations suggested a mesenchymal-like mode of migration for GFP- DCs which is most likely driven by the leading edge of the cell facilitating cell movement in this dense 3D environment (92, 119, 120). The high filopodial activity was found to be associated with the activity of metalloproteases at the filopodial tips, which thereby supports straight forward migration through extracellular matrices at the expense of cell turns (121). This may explain the directional movement and straight paths of GFP- DCs in the collagen matrix (single-cell trajectory graph in Figure 30). GFP+ DCs (with reduced filopodia number and activity) may be less efficient at digesting the collagen, and therefore rather need more turns for pathfinding, while keeping their higher speed and squeezing through the collagen fibers. This effect is

reflected as the Euclidean distance, which shows the distance between the start and endpoint of each cell track (Figure 30).

In line with the suggested mode for GFP- DCs, podosome rosette structures, which are also a hallmark of mesenchymal migration mode, were detected on the majority of GFP- DCs, while these structures were not seen on GFP+ DCs (Figure 32) (60).Expression of filamin A, an actin-binding protein reported to be required for podosome stabilization, podosome rosette formation, extracellular matrix degradation, and three-dimensional mesenchymal migration (94), was decreased in the bulk MV-DCs lysate compared to immature DCs of the same donor (Figure 33). When studied at a single-cell level, Filamin A expression was barely detected in the majority of GFP+ MV-DCs, while it colocalized with podosomes in GFP- DCs (Figure 34). This data, together with higher filamin A MFI in GFP- DCs (Figure 36), indicate that filamin A is more prevalent in GFP- DCs, which is consistent with their mesenchymal-like migration mode.

In the 3D respiratory model experimental set-up, there was no signal opposing DC peripheral recruitment such as CCL-19 and CCL-20 that would attract and thereby might counterforce DC movement towards the chemokine source. MV-infected DC cultures fail to upregulate CCR7 and rather retain CCR5 within the time interval of infection studied (40); therefore the presence of CCR7 ligand is not likely to influence the migration of MV-DCs towards the epithelial cell layer. Implementation of chemokines mimicking lymph node signaling would be possible in a more sophisticated model design.

This also applies to factors possibly supporting DC motility. In contrast to reports using similar 3D models, where pathogens were added to the apical side of the respiratory epithelium, the epithelial cells in our models did not sense the pathogen from the apical side (74, 78, 122, 123). As verified by the experiments involving collagen matrices (Figure 30), enhanced migration of MV-infected DCs migration added to the basolateral side was independent of paracrine signals from the fibroblast or epithelial cells although their presence as tonic mediators in the 3D models cannot be excluded. Mediators tonically secreted from the airway epithelial cells are not well defined and involve IL-8 or lipophilic factors which have been shown to contribute to the induction of hypo-responsiveness of epithelial and immune cells in the respiratory tract (124).

Though not shown for epithelial cells, IL-8 induced in response to S1P has been described as a chemoattractant (125). For technical reasons, the efficiency of MV-infected DCs to release substantial amounts of S1P has not been directly documented, although the impact of S1PR inhibition on DC motility clearly supports the export of S1P from MV-infected DCs (Figure 45). It can, therefore not be excluded that factors released from these cells (such as S1P) act on epithelial cells in the 3D respiratory tract model. Targeted ablation of potentially involved genes in H358-Cas9 cells would help to find out their role in enhanced migration towards epithelial cells, conjugate formation efficiency in virological synapse or viral transmission in future experiments.

5.3 Mechanisms supporting the enforced migration of infected DCs

Actin cytoskeleton remodeling is shown to be crucial for the life cycle of viruses including MV from early stages in entry to the virus budding and egress (126–128). F-actin has been shown to be involved in the MV assembly and budding process in non-hematopoietic cells, its exact role remains poorly defined. F-actin is important in cell to cell fusion by altering the interaction of MV M and H proteins (129) and in nectin-4 ligation by MV H protein during the entry (130). Out study identified MV-induced activity of SphK/S1P system as important in DC cytoskeletal remodeling (Figure 37Figure 40Figure 41), and it remained unclear whether this requires viral replication. S1P subtypes ($S1PR_{1-4}$) were found to be expressed in immature and LPS mature DCs (131, 132), and the sensitivity of enforced DC velocity to $S1PR_1$ inhibition confirms that this receptor is expressed and functional in MV-infected DCs (Figure 41).

S1P acts via G protein-coupled receptors ($S1PR_{1-5}$), and in most types, $S1PR_1$ and $S1PR_3$ mediate Rac stimulation through G_i which promotes the migration (133) while signaling via S1PR2 is usually inhibitory to this process (134). It, therefore, appears that the expression pattern of S1PRs defines the outcome of S1P signals in cell migration.

To evaluate the role of S1P in DC migration specifically, the impact of exogenously induced S1P accumulation on MOCK-iDCs migration was studied. Uncaging of photolyzable caged S1P resulted in significantly enhanced migration as defined by all parameter measured in 3D collagen matrices (Figure 43). As it is uncaged only after

loading, exogenously added S1P is not supposed to interact with S1PRs and activate G-coupled S1P receptor signaling. Although it can do so after export, it may also promote cellular signaling independently of export. This has been evidenced by a study showing mobilization of intracellular Ca2+ in several cell lines within seconds after S1P uncaging, which occurred independently of S1P-GPCR (135). Uncaging of S1P followed by Ca2+ mobilization was also found to activate Rac1, and to mediate the reorganization of cytoskeletal and focal adhesion proteins (100), which almost all are important and involved in cell migration. In this study, signaling pathways triggered were also found to be independent of S1P receptors but required Rac1 activation, which was subsequently activated via the intracellular S1P function (100). Uncaging of S1P experiments in MOCK-iDCs enhances their migration (Figure 43) and thereby lends support to the hypothesis, that higher levels of S1P produced in MV-DCs take part in enhancing their migration (Figure 37 Figure 41). Whether this is mediated by the intracellular activity of S1P or interaction with S1PR after export cannot be finally answered at this point. It is, however, likely that S1PR signaling is at least involved because exposure to VPC, an inhibitor blocking signaling via $S1PR_1$ and $S1PR_3$ selectively reduced the velocity of GFP+ DCs (and not that of GFP- cells) in collagen matrices (Figure 45). Though not excluding an additional role of intracellular S1P, these findings suggest that S1P receptor signaling acts to promote enforced velocity of infected DCs in an autocrine manner to support their fast amoeboid trafficking through the respiratory epithelial tissue.

What might be the role of the S1P/S1PR system in MV-infected DCs at a cellular level? In bone marrow mesenchymal stromal cells, $S1PR_1$ signaling can induce F-actin assembly and interestingly also reduce vinculin expression. If this applied to DCs as well, S1P could thereby contribute to to the absence of stabilized podosomes from infected DCs (136).

The SphK/S1P axis can also suppress ER-stress mediated pro-apoptotic pathways by regulating IRE1α expression (137). Whether MV infection causes ER stress has not been directly investigated. Yet, MV infection activates NOXA transcription and subsequently induces the apoptotic activity of IRF3 (138), and ER stress is also triggered upon overexpression of the MV glycoproteins in non-hematopoietic cells (139). Thus it is likely that MV infection elicits ER stress, which, the virus might be able to control in DCs by triggering SphK/S1PR1 axis in DCs. The SphK/S1PR1 system has also been found to support MV replication. This was shown in SK1 overexpressing cells and also after SK1 inhibition that suppressed MV one day post infection (97). However, in this thesis, SKI-II inhibition suppressed MV replication significantly only three days post infection in DCs (Figure 39) indicating that S1P production might be less important for MV replication in these cells. In line with the effect of SKI-II inhibition on viral replication in DCs, this inhibitor slightly affected MV transmission to H358 co-cultures in 2D experiments (Figures 39 and 40). In contrast, MV transmission to H358 cells in 3D respiratory models was highly sensitive to this inhibitor (Figure 40), suggesting that migration rather than transmission was its main target. This hypothesis

was directly addressed in DC migration in 3D collagen matrix experiments where treatment with SKI-II substantially reduced DC velocity (Figure 41).

How the SphK/S1P system is regulated by MV is unknown. ASM activation and ceramide release have been shown to occur upon DC-SIGN ligation by MV (but also by specific antibodies or mannan) (30). This was only transient, and therefore is not likely to account for S1P accumulation 24 h after infection which could result from virally induced, interference with expression or function of sphingosine-1-phosphatase or sphingosine-1-phosphate lyase (both of which can act to diminish the intracellular S1P pool) (140). These questions could not be addressed in this current study because infection levels in DCs were highly variable, and these cells are not suitable for gene ablation analysis. Therefore, MV regulation of either of these enzymes will have to rely on established cell systems which, unlike Mo-DCs, allow for standardized high-level infection and are easily accessible to genetic modification.

5.4 ASM in MV-DCs migration

It has been previously shown that sphingomyelinase activity and ceramide release in DCs were increased by MV short interaction (141). In the current study, ASM activity was measured 24h after MV infection or MOCK exposure, and it appeared that infection decreased ASM activity dose-dependently (Figure 46). This suggests that reduction of ASM activity correlated with the percentage of infected cells (Figure 46). This was observed for a high number of donors and technical replicates minimizing donor specific effects being involved. This data may imply that ceramide levels also

decrease along with the activity of the ASM infection-dependently. DC-SIGN ligation with MV in DCs resulted in short term ASM activation and ceramide accumulation in the outer membrane leaflet (30), and it remains unclear as to whether this has an impact on the loss of ASM activity 24h later.

MV-infected DCs revealed lower ASM activity along with enhanced migration (Figure 30 Figure 46). To see whether there is a causal connection between these findings, ASM was pharmacologically inhibited in bulk MV-DC culture and migration of GFP-DCs (with an assumed higher basal ASM activity) was analyzed. The results showed a significant elevation of all migration parameter (velocity, accumulated and migration distances) (Figure 47) suggesting a possible link between the ASM activity and migration in DCs. A direct connection between lower ASM activity and enhanced migration has not been reported, yet some publications showed the dephosphorylation of Ezrin (which could lead to reduction in cell migration) and cytoskeletal paralysis upon ASM activation, using either ASM overexpressing cells or ASM activation in cell lines (80, 81) suggesting that lower levels of ASM activity might have a positive effect on migration. In contrast, the absence of ASM was also found to reduce T cell adhesion and consequently transendothelial migration (142).

5.5 Advanced 3D human respiratory tract model

Establishing a suitable infection model to monitor, analyze and study virus transmission both at the levels of donor cell migration and viral cell to cell transmission at the virological synapse prompted us to enhance the level of complexity in our 3D model. It

is necessary to study the different stages of this procedure when in vivo conditions are mimicked as closely as possible.

Thus, it was of interest to advance the model to allow the inclusion of blood vessels present underneath the connective tissue that the infected donor cells should have to pass. Hence, transendothelial migration of DCs plays an important role, as the infected DCs have to cross the endothelial barrier, enter and move up through the connective tissue towards the epithelial layer, reach the epithelial cells and establish virological synapses to transmit the virus (32). Therefore, transendothelial migration can even be counted as a prerequisite of viral transmission.

Establishment of the endothelial layer was carried out using HUVEC cells which are suitable for this setup. These are human primary endothelial cells and have the potential to form vessel-like structures and luminal shapes within the fibers of biological collagen scaffold (Figures 50 and 54) (143, 144). Establishing this system, we noted that in infected HUVEC spheres, which were reminiscent of syncytia, adherence junctions were retained as shown by VE-cadherin stainings (Figures 52 and 53). Receptors involved in MV-infection of HUVEC are unknown, but may, as suggested by these observations, also locate within the adherence junctions. The MV transfer to the adjacent cells in HUVEC spheres might also be due to the cytoplasm leakage of an infected cell, which flows through intracellular membrane pores into an adjacent cell, as was observed and reported earlier for the spread of MV infection of primary airway epithelial cells (34).

The efficiency and migration mode of MV-DCs in transendothelial migration was not studied in this thesis, yet the ability of MV-DCs to transmigrate endothelia and the entire 3D model was confirmed as MV infection and syncytia formation was detected in epithelial cells using both flow cytometry and confocal imaging of the complete model tissue (Figures 55 and 56). This data show indirect evidence that MV-DCs, despite their amoeboid type of migration, were able to cross the endothelial layer, migrate through the collagen, and reach the epithelial cells to transmit the virus. This transendothelial migration could be facilitated via cell squeeze and deformability of the cell body and the nucleus, which was already shown as a typical characteristic for GFP+ MV-DCs (Figures 55 and 56).

Taken together, this data shows that generating 3D tissue models with the ability to combine and reveal the functionality of these different cell types especially immune cells behavior in such sophisticated tissue-like environments provides a useful tool to study the underlying mechanisms in infectious diseases and might be in some cases a potential replacement for animal models.

6 Bibliography

1. Alcamo IE, Bergdahl J. *Anatomy Coloring Workbook*. Random House (2003).

2. Louten J. “Virus Transmission and Epidemiology,”. In: Louten J, editor. *Essential human virology*. London, UK: Academic Press is an imprint of Elsevier (2016). p. 71–92.

3. Gray H, Mitchell AW, Vogl W, Drake RL. *Gray's Anatomy for Students (3rd ed.)*. Churchill Livingstone. 1 online resource.

4. Condon TV, Sawyer RT, Fenton MJ, Riches DW. Lung dendritic cells at the innate-adaptive immune interface. *J Leukoc Biol* (2011) **90**(5):883–95. doi:10.1189/jlb.0311134

5. Hodde J. Naturally occurring scaffolds for soft tissue repair and regeneration. *Tissue Eng* (2002) **8**(2):295–308. doi:10.1089/107632702753725058

6. Frantz C, Stewart KM, Weaver VM. The extracellular matrix at a glance. *J Cell Sci* (2010) **123**(Pt 24):4195–200. doi:10.1242/jcs.023820

7. White ES. Lung extracellular matrix and fibroblast function. *Ann Am Thorac Soc* (2015) **12 Suppl 1**:S30-3. doi:10.1513/AnnalsATS.201406-240MG

8. Zhou Y, Horowitz JC, Naba A, Ambalavanan N, Atabai K, Balestrini J, et al. Extracellular matrix in lung development, homeostasis and disease. *Matrix Biol* (2018) **73**:77–104. doi:10.1016/j.matbio.2018.03.005

9. Wolfson LJ, Strebel PM, Gacic-Dobo M, Hoekstra EJ, McFarland JW, Hersh BS. Has the 2005 measles mortality reduction goal been achieved? A natural history modelling study. *The Lancet* (2007) **369**(9557):191–200. doi:10.1016/S0140-6736(07)60107-X

10. Portnoy A, Jit M, Ferrari M, Hanson M, Brenzel L, Verguet S. Estimates of case-fatality ratios of measles in low-income and middle-income countries: a systematic

review and modelling analysis. *The Lancet Global Health* (2019) **7**(4):e472-e481. doi:10.1016/S2214-109X(18)30537-0

11. Cutts FT, Lessler J, Metcalf CJ. Measles elimination: progress, challenges and implications for rubella control. *Expert Rev Vaccines* (2013) **12**(8):917–32. doi:10.1586/14760584.2013.814847

12. Guerra FM, Bolotin S, Lim G, Heffernan J, Deeks SL, Li Y, et al. The basic reproduction number (R 0) of measles: a systematic review. *The Lancet Infectious Diseases* (2017) **17**(12):e420-e428. doi:10.1016/S1473-3099(17)30307-9

13. Coughlin MM, Bellini WJ, Rota PA. Contribution of dendritic cells to measles virus induced immunosuppression. *Rev Med Virol* (2013) **23**(2):126–38. doi:10.1002/rmv.1735

14. Schneider-Schaulies S, Klagge IM, ter Meulen V. “Dendritic Cells and Measles Virus Infection,”. In: Steinkasserer A, editor. *Dendritic Cells and Virus Infection*. Berlin, Heidelberg: Springer Berlin Heidelberg (2003). p. 77–101.

15. Rota PA, Moss WJ, Takeda M, Swart RL de, Thompson KM, Goodson JL. Measles. *Nat Rev Dis Primers* (2016) **2**:16049. doi:10.1038/nrdp.2016.49

16. Griffin DE. The Immune Response in Measles: Virus Control, Clearance and Protective Immunity. *Viruses* (2016) **8**(10). doi:10.3390/v8100282

17. Griffin DE. “Immune Responses During Measles Virus Infection,”. In: Meulen V, Billeter MA, editors. *Measles Virus*. Berlin, Heidelberg: Springer Berlin Heidelberg (1995). p. 117–34.

18. Griffin DE, Ward BJ. Differential CD4 T cell activation in measles. *J Infect Dis* (1993) **168**(2):275–81. doi:10.1093/infdis/168.2.275

19. Young VA, Rall GF. Making it to the synapse: Measles virus spread in and among neurons. *Curr Top Microbiol Immunol* (2009) **330**:3–30.

20. Jürgen Schneider-Schaulies, Lee M. Dunster, Sibylle Schneider-Schaulies, Volker ter Meulen. Pathogenetic aspects of measles virus infections. *Veterinary Microbiology* (1995) **44**(2):113–25. doi:10.1016/0378-1135(95)00004-T

21. Griffin DE, Oldstone MB. *Measles: Pathogenesis and control*. Berlin: Springer (2009). 292 p.

22. Griffin DE, Oldstone MB. *Measles: History and basic biology*. Berlin: Springer (2009). 195 p.

23. Kemper C, Atkinson JP. Measles virus and CD46. *Curr Top Microbiol Immunol* (2009) **329**:31–57.

24. Tatsuo H, Ono N, Tanaka K, Yanagi Y. SLAM (CDw150) is a cellular receptor for measles virus. *Nature* (2000) **406**(6798):893–7. doi:10.1038/35022579

25. Schwartzberg PL, Mueller KL, Qi H, Cannons JL. SLAM receptors and SAP influence lymphocyte interactions, development and function. *Nat Rev Immunol* (2009) **9**(1):39–46. doi:10.1038/nri2456

26. Noyce RS, Bondre DG, Ha MN, Lin L-T, Sisson G, Tsao M-S, et al. Tumor cell marker PVRL4 (nectin 4) is an epithelial cell receptor for measles virus. *PLoS Pathog* (2011) **7**(8):e1002240. doi:10.1371/journal.ppat.1002240

27. Mühlebach MD, Mateo M, Sinn PL, Prüfer S, Uhlig KM, Leonard VH, et al. Adherens junction protein nectin-4 is the epithelial receptor for measles virus. *Nature* (2011) **480**:530 EP -. doi:10.1038/nature10639

28. Swart RL de, Ludlow M, Witte L de, Yanagi Y, van Amerongen G, McQuaid S, et al. Predominant infection of CD150+ lymphocytes and dendritic cells during measles virus infection of macaques. *PLoS Pathog* (2007) **3**(11):e178. doi:10.1371/journal.ppat.0030178

29. Vries RD de, Swart RL de. Measles immune suppression: functional impairment or numbers game? *PLoS Pathog* (2014) **10**(12):e1004482. doi:10.1371/journal.ppat.1004482

30. Avota E, Gulbins E, Schneider-Schaulies S. DC-SIGN mediated sphingomyelinase-activation and ceramide generation is essential for enhancement of viral uptake in dendritic cells. *PLoS Pathog* (2011) **7**(2):e1001290. doi:10.1371/journal.ppat.1001290

31. Ludlow M, Rennick LJ, Sarlang S, Skibinski G, McQuaid S, Moore T, et al. Wild-type measles virus infection of primary epithelial cells occurs via the basolateral surface without syncytium formation or release of infectious virus. *J Gen Virol* (2010) **91**(Pt 4):971–9. doi:10.1099/vir.0.016428-0

32. Noyce RS, Richardson CD. Nectin 4 is the epithelial cell receptor for measles virus. *Trends Microbiol* (2012) **20**(9):429–39. doi:10.1016/j.tim.2012.05.006

33. Frenzke M, Sawatsky B, Wong XX, Delpeut S, Mateo M, Cattaneo R, et al. Nectin-4-dependent measles virus spread to the cynomolgus monkey tracheal epithelium: role of infected immune cells infiltrating the lamina propria. *J Virol* (2013) **87**(5):2526–34. doi:10.1128/JVI.03037-12

34. Singh BK, Hornick AL, Krishnamurthy S, Locke AC, Mendoza CA, Mateo M, et al. The Nectin-4/Afadin Protein Complex and Intercellular Membrane Pores Contribute to Rapid Spread of Measles Virus in Primary Human Airway Epithelia. *J Virol* (2015) **89**(14):7089–96. doi:10.1128/JVI.00821-15

35. Singh BK, Li N, Mark AC, Mateo M, Cattaneo R, Sinn PL. Cell-to-Cell Contact and Nectin-4 Govern Spread of Measles Virus from Primary Human Myeloid Cells to Primary Human Airway Epithelial Cells. *J Virol* (2016) **90**(15):6808–17. doi:10.1128/JVI.00266-16

36. Leonard VH, Sinn PL, Hodge G, Miest T, Devaux P, Oezguen N, et al. Measles virus blind to its epithelial cell receptor remains virulent in rhesus monkeys but

cannot cross the airway epithelium and is not shed. *J Clin Invest* (2008) **118**(7):2448–58. doi:10.1172/JCI35454

37. Worbs T, Hammerschmidt SI, Förster R. Dendritic cell migration in health and disease. *Nat Rev Immunol* (2017) **17**(1):30–48. doi:10.1038/nri.2016.116

38. Sallusto F, Schaerli P, Loetscher P, Schaniel C, Lenig D, Mackay CR, et al. Rapid and coordinated switch in chemokine receptor expression during dendritic cell maturation. *Eur. J. Immunol.* (1998) **28**(9):2760–9. doi:10.1002/(SICI)1521-4141(199809)28:09<2760:AID-IMMU2760>3.0.CO;2-N

39. Randolph GJ, Angeli V, Swartz MA. Dendritic-cell trafficking to lymph nodes through lymphatic vessels. *Nat Rev Immunol* (2005) **5**(8):617–28. doi:10.1038/nri1670

40. Abt M, Gassert E, Schneider-Schaulies S. Measles virus modulates chemokine release and chemotactic responses of dendritic cells. *J Gen Virol* (2009) **90**(Pt 4):909–14. doi:10.1099/vir.0.008581-0

41. Friedl P, Wolf K. Plasticity of cell migration: a multiscale tuning model. *J Cell Biol* (2010) **188**(1):11–9. doi:10.1083/jcb.200909003

42. Charras G, Sahai E. Physical influences of the extracellular environment on cell migration. *Nature Reviews Molecular Cell Biology* (2014) **15**(12):813.

43. Friedl P. Prespecification and plasticity: shifting mechanisms of cell migration. *Curr Opin Cell Biol* (2004) **16**(1):14–23. doi:10.1016/j.ceb.2003.11.001

44. Bear JE, Haugh JM. Directed migration of mesenchymal cells: where signaling and the cytoskeleton meet. *Curr Opin Cell Biol* (2014) **30**:74–82. doi:10.1016/j.ceb.2014.06.005

45. Lämmermann T, Sixt M. Mechanical modes of 'amoeboid' cell migration. *Curr Opin Cell Biol* (2009) **21**(5):636–44. doi:10.1016/j.ceb.2009.05.003

46. Petrie RJ, Doyle AD, Yamada KM. Random versus directionally persistent cell migration. *Nature Reviews Molecular Cell Biology* (2009) **10**:538 EP -. doi:10.1038/nrm2729

47. Mitchison TJ, Cramer LP. Actin-Based Cell Motility and Cell Locomotion. *Cell* (1996) **84**(3):371–9. doi:10.1016/S0092-8674(00)81281-7

48. Skau CT, Waterman CM. Specification of Architecture and Function of Actin Structures by Actin Nucleation Factors. *Annu Rev Biophys* (2015) **44**:285–310. doi:10.1146/annurev-biophys-060414-034308

49. Sahai E, Marshall CJ. Differing modes of tumour cell invasion have distinct requirements for Rho/ROCK signalling and extracellular proteolysis. *Nat Cell Biol* (2003) **5**(8):711–9. doi:10.1038/ncb1019

50. Vargas P, Maiuri P, Bretou M, Sáez PJ, Pierobon P, Maurin M, et al. Innate control of actin nucleation determines two distinct migration behaviours in dendritic cells. *Nat Cell Biol* (2016) **18**(1):43–53. doi:10.1038/ncb3284

51. Lämmermann T, Bader BL, Monkley SJ, Worbs T, Wedlich-Söldner R, Hirsch K, et al. Rapid leukocyte migration by integrin-independent flowing and squeezing. *Nature* (2008) **453**(7191):51–5. doi:10.1038/nature06887

52. Even-Ram S, Yamada KM. Cell migration in 3D matrix. *Curr Opin Cell Biol* (2005) **17**(5):524–32. doi:10.1016/j.ceb.2005.08.015

53. Wolf K, Müller R, Borgmann S, Bröcker E-B, Friedl P. Amoeboid shape change and contact guidance: T-lymphocyte crawling through fibrillar collagen is independent of matrix remodeling by MMPs and other proteases. *Blood* (2003) **102**(9):3262–9. doi:10.1182/blood-2002-12-3791

54. Linder S, Wiesner C. Tools of the trade: podosomes as multipurpose organelles of monocytic cells. *Cell Mol Life Sci* (2015) **72**(1):121–35. doi:10.1007/s00018-014-1731-z

55. Gawden-Bone C, Zhou Z, King E, Prescott A, Watts C, Lucocq J. Dendritic cell podosomes are protrusive and invade the extracellular matrix using metalloproteinase MMP-14. *J Cell Sci* (2010) **123**(Pt 9):1427–37. doi:10.1242/jcs.056515

56. Murphy DA, Courtneidge SA. The 'ins' and 'outs' of podosomes and invadopodia: characteristics, formation and function. *Nat Rev Mol Cell Biol* (2011) **12**(7):413–26. doi:10.1038/nrm3141

57. Schachtner H, Calaminus SD, Thomas SG, Machesky LM. Podosomes in adhesion, migration, mechanosensing and matrix remodeling. *Cytoskeleton (Hoboken)* (2013) **70**(10):572–89. doi:10.1002/cm.21119

58. Kanatani S, Uhlén P, Barragan A. Infection by Toxoplasma gondii Induces Amoeboid-Like Migration of Dendritic Cells in a Three-Dimensional Collagen Matrix. *PLoS ONE* (2015) **10**(9):e0139104. doi:10.1371/journal.pone.0139104

59. Yamaguchi H, Lorenz M, Kempiak S, Sarmiento C, Coniglio S, Symons M, et al. Molecular mechanisms of invadopodium formation: the role of the N-WASP-Arp2/3 complex pathway and cofilin. *J Cell Biol* (2005) **168**(3):441–52. doi:10.1083/jcb.200407076

60. Cougoule C, Lastrucci C, Guiet R, Mascarau R, Meunier E, Lugo-Villarino G, et al. Podosomes, But Not the Maturation Status, Determine the Protease-Dependent 3D Migration in Human Dendritic Cells. *Front Immunol* (2018) **9**:846. doi:10.3389/fimmu.2018.00846

61. Airola MV, Hannun YA. Sphingolipid metabolism and neutral sphingomyelinases. *Handb Exp Pharmacol* (2013) (215):57–76. doi:10.1007/978-3-7091-1368-4_3

62. Hannun YA, Obeid LM. Principles of bioactive lipid signalling: lessons from sphingolipids. *Nature Reviews Molecular Cell Biology* (2008) **9**:139 EP -. doi:10.1038/nrm2329

63. Kitatani K, Idkowiak-Baldys J, Hannun YA. The sphingolipid salvage pathway in ceramide metabolism and signaling. *Cell Signal* (2008) **20**(6):1010–8. doi:10.1016/j.cellsig.2007.12.006

64. Bartke N, Hannun YA. Bioactive sphingolipids: metabolism and function. *J Lipid Res* (2009) **50 Suppl**:S91-6. doi:10.1194/jlr.R800080-JLR200

65. El Alwani M, Wu BX, Obeid LM, Hannun YA. Bioactive sphingolipids in the modulation of the inflammatory response. *Pharmacol Ther* (2006) **112**(1):171–83. doi:10.1016/j.pharmthera.2006.04.004

66. Ma Y, Pitson S, Hercus T, Murphy J, Lopez A, Woodcock J. Sphingosine activates protein kinase A type II by a novel cAMP-independent mechanism. *J Biol Chem* (2005) **280**(28):26011–7. doi:10.1074/jbc.M409081200

67. Czeloth N, Bernhardt G, Hofmann F, Genth H, Förster R. Sphingosine-1-phosphate mediates migration of mature dendritic cells. *J Immunol* (2005) **175**(5):2960–7. doi:10.4049/jimmunol.175.5.2960

68. Olivera A, Rosenfeldt HM, Bektas M, Wang F, Ishii I, Chun J, et al. Sphingosine kinase type 1 induces G12/13-mediated stress fiber formation, yet promotes growth and survival independent of G protein-coupled receptors. *J Biol Chem* (2003) **278**(47):46452–60. doi:10.1074/jbc.M308749200

69. Jingsong Xu, Fei Wang, Alexandra Van Keymeulen, Paul Herzmark, Aaron Straight, Kathleen Kelly, et al. Divergent Signals and Cytoskeletal Assemblies Regulate Self-Organizing Polarity in Neutrophils. *Cell* (2003) **114**(2):201–14. doi:10.1016/S0092-8674(03)00555-5

70. Arikawa K, Takuwa N, Yamaguchi H, Sugimoto N, Kitayama J, Nagawa H, et al. Ligand-dependent inhibition of B16 melanoma cell migration and invasion via endogenous S1P2 G protein-coupled receptor. Requirement of inhibition of cellular RAC activity. *J Biol Chem* (2003) **278**(35):32841–51. doi:10.1074/jbc.M305024200

71. Charest PG, Firtel RA. Big roles for small GTPases in the control of directed cell movement. *Biochem J* (2007) **401**(2):377–90. doi:10.1042/BJ20061432

72. Kimura K, Ito M, Amano M, Chihara K, Fukata Y, Nakafuku M, et al. Regulation of myosin phosphatase by Rho and Rho-associated kinase (Rho-kinase). *Science* (1996) **273**(5272):245–8. doi:10.1126/science.273.5272.245

73. Hutmacher DW, Cool S. Concepts of scaffold-based tissue engineering--the rationale to use solid free-form fabrication techniques. *J Cell Mol Med* (2007) **11**(4):654–69. doi:10.1111/j.1582-4934.2007.00078.x

74. Chandorkar P, Posch W, Zaderer V, Blatzer M, Steger M, Ammann CG, et al. Fast-track development of an in vitro 3D lung/immune cell model to study Aspergillus infections. *Sci Rep* (2017) **7**(1):11644. doi:10.1038/s41598-017-11271-4

75. Tam RY, Yockell-Lelièvre J, Smith LJ, Julian LM, Baker AE, Choey C, et al. Rationally Designed 3D Hydrogels Model Invasive Lung Diseases Enabling High-Content Drug Screening. *Adv Mater Weinheim* (2019) **31**(7):e1806214. doi:10.1002/adma.201806214

76. Benam KH, Dauth S, Hassell B, Herland A, Jain A, Jang K-J, et al. Engineered in vitro disease models. *Annu Rev Pathol* (2015) **10**:195–262. doi:10.1146/annurev-pathol-012414-040418

77. Derakhshani S, Kurz A, Japtok L, Schumacher F, Pilgram L, Steinke M, et al. Measles Virus Infection Fosters Dendritic Cell Motility in a 3D Environment to Enhance Transmission to Target Cells in the Respiratory Epithelium. *Front Immunol* (2019) **10**:1294. doi:10.3389/fimmu.2019.01294

78. Ding P, Wu H, Fang L, Wu M, Liu R. Transmigration and phagocytosis of macrophages in an airway infection model using four-dimensional techniques. *Am J Respir Cell Mol Biol* (2014) **51**(1):1–10. doi:10.1165/rcmb.2013-0390TE

79. Shahin K, Doran PM. Shear and Compression Bioreactor for Cartilage Synthesis. *Methods Mol Biol* (2015) **1340**:221–33. doi:10.1007/978-1-4939-2938-2_16

80. O'Connor MD. The 3R principle: advancing clinical application of human pluripotent stem cells. *Stem Cell Res Ther* (2013) **4**(2):21. doi:10.1186/scrt169

81. Khademhosseini A, Langer R. A decade of progress in tissue engineering. *Nature Protocols* (2016) **11**:1775 EP -. doi:10.1038/nprot.2016.123

82. Moll C, Reboredo J, Schwarz T, Appelt A, Schürlein S, Walles H, et al. Tissue Engineering of a Human 3D in vitro Tumor Test System. *J Vis Exp* (2013) (78). doi:10.3791/50460

83. Qiao L, Kozikowski AP, Olivera A, Spiegel S. Synthesis and evaluation of a photolyzable derivative of sphingosine 1-phosphate--caged SPP. *Bioorg Med Chem Lett* (1998) **8**(7):711–4.

84. Fayyaz S, Henkel J, Japtok L, Krämer S, Damm G, Seehofer D, et al. Involvement of sphingosine 1-phosphate in palmitate-induced insulin resistance of hepatocytes via the S1P2 receptor subtype. *Diabetologia* (2014) **57**(2):373–82. doi:10.1007/s00125-013-3123-6

85. Griffith LG, Swartz MA. Capturing complex 3D tissue physiology in vitro. *Nature Reviews Molecular Cell Biology* (2006) **7**(3):211–24. doi:10.1038/nrm1858

86. Steinke M, Gross R, Walles H, Gangnus R, Schütze K, Walles T. An engineered 3D human airway mucosa model based on an SIS scaffold. *Biomaterials* (2014) **35**(26):7355–62. doi:10.1016/j.biomaterials.2014.05.031

87. Fugier-Vivier I, Servet-Delprat C, Rivailler P, Rissoan M-C, Liu Y-J, Rabourdin-Combe C. Measles Virus Suppresses Cell-mediated Immunity by Interfering with the Survival and Functions of Dendritic and T Cells. J Exp Med (1997) 186(6):813–23.

88. Servet-Delprat C, Vidalain PO, Bausinger H, Manié S, Le Deist F, Azocar O, et al. Measles virus induces abnormal differentiation of CD40 ligand-activated human dendritic cells. *J Immunol* (2000) **164**(4):1753–60. doi:10.4049/jimmunol.164.4.1753

89. Avota E, Koethe S, Schneider-Schaulies S. Membrane dynamics and interactions in measles virus dendritic cell infections. *Cell Microbiol* (2013) **15**(2):161–9. doi:10.1111/cmi.12025

90. Griffin DE. Measles virus-induced suppression of immune responses. Immunol Rev (2010) 236:176–89. doi:10.1111/j.1600-065X.2010.00925.x

91. Barry DJ, Durkin CH, Abella JV, Way M. Open source software for quantification of cell migration, protrusions, and fluorescence intensities. *J Cell Biol* (2015) **209**(1):163–80. doi:10.1083/jcb.201501081

92. Sánchez-Madrid F, Serrador JM. Bringing up the rear: defining the roles of the uropod. *Nature Reviews Molecular Cell Biology* (2009) **10**:353 EP -. doi:10.1038/nrm2680

93. Lämmermann T, Renkawitz J, Wu X, Hirsch K, Brakebusch C, Sixt M. Cdc42-dependent leading edge coordination is essential for interstitial dendritic cell migration. *Blood* (2009) **113**(23):5703–10. doi:10.1182/blood-2008-11-191882

94. Guiet R, Vérollet C, Lamsoul I, Cougoule C, Poincloux R, Labrousse A, et al. Macrophage mesenchymal migration requires podosome stabilization by filamin A. *J Biol Chem* (2012) **287**(16):13051–62. doi:10.1074/jbc.M111.307124

95. Takuwa Y, Okamoto Y, Yoshioka K, Takuwa N. Sphingosine-1-phosphate signaling in physiology and diseases. *Biofactors* (2012) **38**(5):329–37.

96. Pyne NJ, Pyne S. Sphingosine 1-phosphate and cancer. *Nat Rev Cancer* (2010) **10**(7):489–503. doi:10.1038/nrc2875

97. Vijayan M, Seo Y-J, Pritzl CJ, Squires SA, Alexander S, Hahm B. Sphingosinekinase1regulates measles virus replication. *Virology* (2014) **450-451**:55–63. doi:10.1016/j.virol.2013.11.039

98. Kumar A, Saba J. Regulation of Immune Cell Migration by Sphingosine-1-Phosphate. *Cell Mol Biol (OMICS)* (2015) **61**(2).

99. Mitra P, Oskeritzian CA, Payne SG, Beaven MA, Milstien S, Spiegel S. Role of ABCC1 in export of sphingosine-1-phosphate from mast cells. *Proceedings of the National Academy of Sciences* (2006) **103**(44):16394–9. doi:10.1073/pnas.0603734103

100. Usatyuk PV, He D, Bindokas V, Gorshkova IA, Berdyshev EV, Garcia JG, et al. Photolysis of caged sphingosine-1-phosphate induces barrier enhancement and intracellular activation of lung endothelial cell signaling pathways. *Am J Physiol Lung Cell Mol Physiol* (2011) **300**(6):L840-50. doi:10.1152/ajplung.00404.2010

101. Park KS, Kim M-K, Lee HY, Kim SD, Lee SY, Kim JM, et al. S1P stimulates chemotactic migration and invasion in OVCAR3 ovarian cancer cells. *Biochem Biophys Res Commun* (2007) **356**(1):239–44. doi:10.1016/j.bbrc.2007.02.112

102. Zscheppang K, Berg J, Hedtrich S, Verheyen L, Wagner DE, Suttorp N, et al. Human Pulmonary 3D Models For Translational Research. *Biotechnol J* (2018) **13**(1). doi:10.1002/biot.201700341

103. Nguyen Hoang AT, Chen P, Juarez J, Sachamitr P, Billing B, Bosnjak L, et al. Dendritic cell functional properties in a three-dimensional tissue model of human lung mucosa. *Am J Physiol Lung Cell Mol Physiol* (2012) **302**(2):L226-37. doi:10.1152/ajplung.00059.2011

104. Choe MM, Sporn PH, Swartz MA. Extracellular matrix remodeling by dynamic strain in a three-dimensional tissue-engineered human airway wall model. *Am J Respir Cell Mol Biol* (2006) **35**(3):306–13. doi:10.1165/rcmb.2005-0443OC

105. Tomasek JJ, Gabbiani G, Hinz B, Chaponnier C, Brown RA. Myofibroblasts and mechano-regulation of connective tissue remodelling. *Nature Reviews Molecular Cell Biology* (2002) **3**(5):349–63. doi:10.1038/nrm809

106. Pusch J, Votteler M, Göhler S, Engl J, Hampel M, Walles H, et al. The physiological performance of a three-dimensional model that mimics the microenvironment of the small intestine. *Biomaterials* (2011) **32**(30):7469–78. doi:10.1016/j.biomaterials.2011.06.035

107. Fugier-Vivier I, Servet-Delprat C, Rivailler P, Rissoan M-C, Liu Y-J, Rabourdin-Combe C. Measles Virus Suppresses Cell-mediated Immunity by Interfering with the Survival and Functions of Dendritic and T Cells. *J Exp Med* (1997) **186**(6):813–23.

108. Schnorr JJ, Xanthakos S, Keikavoussi P, Kämpgen E, ter Meulen V, Schneider-Schaulies S. Induction of maturation of human blood dendritic cell precursors by measles virus is associated with immunosuppression. *Proc Natl Acad Sci U S A* (1997) **94**(10):5326–31. doi:10.1073/pnas.94.10.5326

109. Klagge IM, Meulen Vt, Schneider-Schaulies S. Measles virus-induced promotion of dendritic cell maturation by soluble mediators does not overcome the immunosuppressive activity of viral glycoproteins on the cell surface. *Eur. J. Immunol.* (2000) **30**(10):2741–50. doi:10.1002/1521-4141(200010)30:10<2741:AID-IMMU2741>3.0.CO;2-N

110. Bieback K, Lien E, Klagge IM, Avota E, Schneider-Schaulies J, Duprex WP, et al. Hemagglutinin protein of wild-type measles virus activates toll-like receptor 2 signaling. *J Virol* (2002) **76**(17):8729–36. doi:10.1128/jvi.76.17.8729-8736.2002

111. Shishkova Y, Harms H, Krohne G, Avota E, Schneider-Schaulies S. Immune synapses formed with measles virus-infected dendritic cells are unstable and fail to sustain T cell activation. *Cell Microbiol* (2007) **9**(8):1974–86. doi:10.1111/j.1462-5822.2007.00928.x

112. Servet-Delprat C, Vidalain P-O, Azocar O, Le Deist F, Fischer A, Rabourdin-Combe C. Consequences of Fas-Mediated Human Dendritic Cell Apoptosis Induced by Measles Virus. *J Virol* (2000) **74**(9):4387–93.

113. Vidalain PO, Azocar O, Lamouille B, Astier A, Rabourdin-Combe C, Servet-Delprat C. Measles virus induces functional TRAIL production by human dendritic cells. *J Virol* (2000) **74**(1):556–9. doi:10.1128/jvi.74.1.556-559.2000

114. Schweinlin M, Wilhelm S, Schwedhelm I, Hansmann J, Rietscher R, Jurowich C, et al. Development of an Advanced Primary Human In Vitro Model of the Small Intestine. *Tissue Eng Part C Methods* (2016) **22**(9):873–83. doi:10.1089/ten.TEC.2016.0101

115. Quast T, Tappertzhofen B, Schild C, Grell J, Czeloth N, Förster R, et al. Cytohesin-1 controls the activation of RhoA and modulates integrin-dependent adhesion and migration of dendritic cells. *Blood* (2009) **113**(23):5801–10. doi:10.1182/blood-2008-08-176123

116. Ólafsson EB, Varas-Godoy M, Barragan A. Toxoplasma gondii infection shifts dendritic cells into an amoeboid rapid migration mode encompassing podosome dissolution, secretion of TIMP-1, and reduced proteolysis of extracellular matrix. *Cell Microbiol* (2018) **20**(3). doi:10.1111/cmi.12808

117. Wilson CA, Tsuchida MA, Allen GM, Barnhart EL, Applegate KT, Yam PT, et al. Myosin II contributes to cell-scale actin network treadmilling through network disassembly. *Nature* (2010) **465**:373 EP -. doi:10.1038/nature08994

118. Barbier L, Sáez PJ, Attia R, Lennon-Duménil A-M, Lavi I, Piel M, et al. Myosin II Activity Is Selectively Needed for Migration in Highly Confined Microenvironments in Mature Dendritic Cells. *Front Immunol* (2019) **10**:747. doi:10.3389/fimmu.2019.00747

119. Thiam H-R, Vargas P, Carpi N, Crespo CL, Raab M, Terriac E, et al. Perinuclear Arp2/3-driven actin polymerization enables nuclear deformation to facilitate cell

migration through complex environments. *Nat Commun* (2016) **7**:10997. doi:10.1038/ncomms10997

120. Leithner A, Eichner A, Müller J, Reversat A, Brown M, Schwarz J, et al. Diversified actin protrusions promote environmental exploration but are dispensable for locomotion of leukocytes. *Nat Cell Biol* (2016) **18**(11):1253–9. doi:10.1038/ncb3426

121. Ridley AJ. Life at the leading edge. *Cell* (2011) **145**(7):1012–22. doi:10.1016/j.cell.2011.06.010

122. Bhowmick R, Derakhshan T, Liang Y, Ritchey J, Liu L, Gappa-Fahlenkamp H. A Three-Dimensional Human Tissue-Engineered Lung Model to Study Influenza A Infection. *Tissue Eng Part A* (2018) **24**(19-20):1468–80. doi:10.1089/ten.TEA.2017.0449

123. Braian C, Svensson M, Brighenti S, Lerm M, Parasa VR. A 3D Human Lung Tissue Model for Functional Studies on Mycobacterium tuberculosis Infection. *J Vis Exp* (2015) (104). doi:10.3791/53084

124. Weitnauer M, Mijošek V, Dalpke AH. Control of local immunity by airway epithelial cells. *Mucosal Immunol* (2016) **9**(2):287–98. doi:10.1038/mi.2015.126

125. Daniela Brünnert, Svea Piccenini, Jens Ehrhardt, Marek Zygmunt, Pankaj Goyal. Sphingosine 1-phosphate regulates IL-8 expression and secretion via S1PR1 and S1PR2 receptors-mediated signaling in extravillous trophoblast derived HTR-8/SVneo cells. *Placenta* (2015) **36**(10):1115–21. doi:10.1016/j.placenta.2015.08.010

126. Taylor MP, Koyuncu OO, Enquist LW. Subversion of the actin cytoskeleton during viral infection. *Nat Rev Microbiol* (2011) **9**(6):427–39. doi:10.1038/nrmicro2574

127. Bohn W, Rutter G, Hohenberg H, Mannweiler K, Nobis P. Involvement of actin filaments in budding of measles virus: Studies on cytoskeletons of infected cells. Virology (1986) 149(1):91–106. doi:10.1016/0042-6822(86)90090-5

128. Dietzel E, Kolesnikova L, Maisner A. Actin filaments disruption and stabilization affect measles virus maturation by different mechanisms. *Virol J* (2013) **10**:249. doi:10.1186/1743-422X-10-249

129. Wakimoto H, Shimodo M, Satoh Y, Kitagawa Y, Takeuchi K, Gotoh B, et al. F-actin modulates measles virus cell-cell fusion and assembly by altering the interaction between the matrix protein and the cytoplasmic tail of hemagglutinin. *J Virol* (2013) **87**(4):1974–84. doi:10.1128/JVI.02371-12

130. Liu Y-P, Russell SP, Ayala-Breton C, Russell SJ, Peng K-W. Ablation of nectin4 binding compromises CD46 usage by a hybrid vesicular stomatitis virus/measles virus. *J Virol* (2014) **88**(4):2195–204. doi:10.1128/JVI.02628-13

131. *Müller H, Hofer S, Kaneider N, Neuwirt H, Mosheimer B, Mayer G, et al. The immunomodulator FTY720 interferes with effector functions of human monocyte-derived dendritic cells. Eur. J. Immunol. (2005) 35(2):533–45. doi:10.1002/eji.200425556*

132. Bryan AM, Del Poeta M. Sphingosine-1-phosphate receptors and innate immunity. *Cell Microbiol* (2018) **20**(5):e12836. doi:10.1111/cmi.12836

133. Takuwa Y. Subtype-specific differential regulation of Rho family G proteins and cell migration by the Edg family sphingosine-1-phosphate receptors. *Biochimica et Biophysica Acta (BBA) - Molecular and Cell Biology of Lipids* (2002) **1582**(1-3):112–20. doi:10.1016/S1388-1981(02)00145-2

134. Sanchez T, Hla T. Structural and functional characteristics of S1P receptors. *J Cell Biochem* (2004) **92**(5):913–22. doi:10.1002/jcb.20127

135. Meyer zu Heringdorf D, Liliom K, Schaefer M, Danneberg K, Jaggar JH, Tigyi G, et al. Photolysis of intracellular caged sphingosine-1-phosphate causes Ca 2+ mobilization independently of G-protein-coupled receptors. *FEBS Letters* (2003) **554**(3):443–9. doi:10.1016/S0014-5793(03)01219-5

136. Sassoli C, Pierucci F, Tani A, Frati A, Chellini F, Matteini F, et al. Sphingosine 1-Phosphate Receptor 1 Is Required for MMP-2 Function in Bone Marrow Mesenchymal Stromal Cells: Implications for Cytoskeleton Assembly and Proliferation. *Stem Cells Int* (2018) **2018**:5034679. doi:10.1155/2018/5034679

137. Qi Y, Wang W, Chen J, Dai L, Kaczorowski D, Gao X, et al. Sphingosine Kinase 1 Protects Hepatocytes from Lipotoxicity via Down-regulation of IRE1α Protein Expression. *J Biol Chem* (2015) **290**(38):23282–90. doi:10.1074/jbc.M115.677542

138. Lallemand C, Blanchard B, Palmieri M, Lebon P, May E, Tovey MG. Single-stranded RNA viruses inactivate the transcriptional activity of p53 but induce NOXA-dependent apoptosis via post-translational modifications of IRF-1, IRF-3 and CREB. Oncogene (2007) 26(3):328–38. doi:10.1038/sj.onc.1209795

139. Ciplys E, Samuel D, Juozapaitis M, Sasnauskas K, Slibinskas R. Overexpression of human virus surface glycoprotein precursors induces cytosolic unfolded protein response in Saccharomyces cerevisiae. *Microb Cell Fact* (2011) **10**:37. doi:10.1186/1475-2859-10-37

140. Gault CR, Obeid LM, Hannun YA. An overview of sphingolipid metabolism: from synthesis to breakdown. Adv Exp Med Biol (2010) 688:1–23.

141. Gassert E, Avota E, Harms H, Krohne G, Gulbins E, Schneider-Schaulies S. Induction of membrane ceramides: a novel strategy to interfere with T lymphocyte cytoskeletal reorganisation in viral immunosuppression. *PLoS Pathog* (2009) **5**(10):e1000623. doi:10.1371/journal.ppat.1000623

142. Lopes Pinheiro MA, Kroon J, Hoogenboezem M, Geerts D, van Het Hof B, van der Pol SM, et al. Acid Sphingomyelinase-Derived Ceramide Regulates ICAM-1

Function during T Cell Transmigration across Brain Endothelial Cells. *J Immunol* (2016) **196**(1):72–9. doi:10.4049/jimmunol.1500702

143. Park H-J, Zhang Y, Georgescu SP, Johnson KL, Kong D, Galper JB. Human umbilical vein endothelial cells and human dermal microvascular endothelial cells offer new insights into the relationship between lipid metabolism and angiogenesis. *Stem Cell Rev* (2006) **2**(2):93–102. doi:10.1007/s12015-006-0015-x

144. Alberts B, Johnson A, Lewis J, Raff M, Roberts K, Walter P. *Molecular biology of the cell*. New York, NY: Garland Science Taylor & Francis Group (2002). 1 p.